Université du Québec
Institut national de la recherche scientifique
Centre Énergie Matériaux Télécommunications

Towards an Automated Portable Electroencephalography-based System for Alzheimer's Disease Diagnosis

By

Raymundo Cassani González

A thesis submitted in fulfillment of the requirements for the degree of
Doctorate of Sciences, Ph.D
in Telecommunications

Evaluation Committee

Internal evaluator and committee president:	Prof. Douglas O'Shaughnessy
External evaluator 1:	Prof. Justin Dauwels Nanyang Technological University
External evaluator 2:	Prof. Alexandre Lehmann McGill University
Research advisor:	Prof. Tiago H. Falk

“Not all those who wander are lost”

Gandalf

Acknowledgements

My deepest gratitude for my supervisor Dr. Tiago H. Falk for the support, opportunities and challenges provided throughout the PhD program, his role as supervisor surpasses all expectations, as such, his mentorship and attitude have been vital for the completion of this thesis, and for my personal development, it is great pleasure to work with him.

I would like also to thank all the members and ex-members of the MuSAE lab for their incredible help, advice, company, and for the fun we have had while discussing ideas, running experiments, rushing for deadlines, debating and so on. In particular, I would like to thank Hubert J. Banville, Rishabh Gupta, João F. Santos and Anderson Avila for their support and camaraderie. Moreover, special thanks to Dr. Franciso J. Fraga and Lucas Trambaiolli whose collaboration and advice were pivotal at different stages of this work.

Without my family, I would not be the person that I am today, I would like to largely thank my family, my parents Raymundo and Martha, and my sister Marlene; who despite the distance are always in my mind, thanks for gaving your love, support, advice and care. Finally, I would like to greatly thank to my partner in life (and crime) Ana, for her love, friendship, support, patience, help, feedback, humor during all these years.

There are not words to describe how grateful I am with every single person who helped to make this work possible. This thesis dedicated to all of you.

Abstract

Alzheimer's disease (AD) is a neurodegenerative terminal disorder that accounts for nearly 70% of dementia cases worldwide. Global dementia incidence is projected to 75 million cases by 2030, with the majority of the affected individuals coming from low- and medium- income countries. Although there is no cure for AD, early diagnosis can improve the quality of life of AD patients and their caregivers. Currently, AD diagnosis is carried out using mental status examinations, expensive neuroimaging scans, and invasive laboratory tests, all of which render the diagnosis time-consuming and costly. Notwithstanding, over the last decade electroencephalography (EEG), specifically resting-state EEG (rsEEG), has emerged as an alternative technique for AD diagnosis with accuracies inline with those obtained with more expensive neuroimaging tools, such as magnetic resonance imaging (MRI), computed tomography (CT) and positron emission tomography (PET). However the use of rsEEG for AD diagnosis presents two major disadvantages: (*i*) the reliance on"artifact-free'' segments, which are manually and meticulously selected by expert clinicians, and (*ii*) the need for research- and medical-grade EEG devices often with 16+ electrodes, thus making them hard to transport and expensive to fund, specially for low- and middle-income countries. In this doctoral thesis, we present the steps towards the development of an automated portable and low-cost rsEEG-based system for AD diagnosis. To achieve this goal, three main innovations have been developed.

First, we explored the effects of several fully automated artifact handling (AAH) methods on rsEEG signals and reported their advantages and disadvantages for automated AD diagnosis. The outcome of this exploration showed the AD diagnosis based on AAH-enhanced rsEEG signals is inline with the performance obtained with "artifact-free" EEG data, suggesting that expert human intervention and the discard of EEG data (due to artifacts) can be avoided. Secondly, we evaluated and compared the use of lower-density (7-channel) EEG devices for rsEEG eyes-open and eyes-closed experimental protocols for AD diagnosis. By comparing the diagnosis performance obtained with the low-density EEG devices to the one obtained with a typical medium-density (20-channel) system, we found that the reduction of channels diminishes the classification performance. Lastly, we showed that conventional features proposed in the literature are not only sensitive to artifacts, but rely on information extracted from EEG frequency subbands that are suboptimal for AD diagnosis. As such, we proposed a new set of features based on the modulation spectrogram approach. Experiments showed the proposed features being robust to artifacts, thus bypassing the need for AAH algorithms, as well as providing more discriminatory information not only for AD diagnosis, but also for disease progression monitoring. These new benefits are invaluable for the development of low-cost portable devices and it is hoped that the insights presented herein can be used to improve the quality-of-life of individuals living with AD, their families, and caregivers.

Keywords: Alzheimer's disease, electroencephalography, resting-state, amplitude modulation, automated artifact handing, portable EEG

Résumé

La maladie d'Alzheimer (MA) est une maladie neurodégénérative terminale qui représente près de 70% des cas de démence. L'incidence mondiale de la démence devrait atteindre 75 millions d'individus d'ici 2030, dont la majorité des personnes atteintes viendraient de pays à revenus faibles ou moyens. Bien qu'il n'y ait pas de traitement curatif pour la MA, un diagnostic précoce peut améliorer la qualité de vie des patients atteints de la MA et de leurs soignants. Actuellement, le diagnostic de la MA est effectué à l'aide de tests d'évaluation de l'état mental, d'examens de neuroimagerie coûteux et de tests de laboratoire invasifs, ce qui rend le diagnostic long et onéreux. Toutefois, l'électroencéphalographie (EEG), en particulier l'EEG à l'état de repos (rsEEG), est apparue au cours de la dernière décennie comme une technique alternative pour le diagnostic de la MA offrant des précisions comparables à celles d'outils de neuroimagerie plus coûteux, tels la tomodensitométrie et la tomographie par émission de positrons. Cependant, l'utilisation de la rsEEG pour le diagnostic de la MA présente deux inconvénients majeurs: (*i*) la dépendance à des segments «sans artefacts», sélectionnés manuellement et méticuleusement par des cliniciens experts, et (*ii*) le besoin d'appareils EEG de qualité médicale et convenant à la recherche comportant souvent plus de 16 électrodes, ce qui les rend difficiles à transporter et coûteux, en particulier pour les pays à revenus faibles ou intermédiaires. Dans cette thèse de doctorat, nous présentons les étapes vers le développement d'un système automatisé basé sur la rsEEG portable et peu coûteux pour le diagnostic de la maladie d'Alzheimer. Pour atteindre cet objectif, trois innovations principales ont été développées.

Premièrement, nous avons exploré les effets de plusieurs méthodes de manipulation automatisée des artefacts (MAA) sur les signaux rsEEG et nous avons étudié leurs avantages et désavantages pour le diagnostic automatisé de la MA. Les résultats de cette exploration ont montré que le diagnostic de la MA basé sur les signaux rsEEG améliorés par les méthodes de MAA est comparable à la performance obtenue avec les données EEG «sans artefact», suggérant que l'intervention humaine experte et l'élimination des segments d'EEG (dûes aux artefacts) peuvent être évités. Deuxièmement, nous avons évalué et comparé l'utilisation de dispositifs EEG à densité basse (7 canaux) pour les protocoles expérimentaux à yeux ouverts et à yeux fermés en rsEEG pour le diagnostic de la MA. Leur performance a été comparée à celle d'un système à densité moyenne (20 canaux), qui était en général considérablement plus élevée que les configurations à densité basse. Enfin, nous avons montré que les traits caractéristiques conventionnels proposés dans la littérature ne sont pas seulement sensibles aux artefacts, mais reposent sur des informations extraites de bandes de fréquences EEG qui ne sont pas optimales pour le diagnostic de la MA. De ce fait, nous avons proposé un nouvel ensemble de traits caractéristiques basé sur l'approche par spectrogramme de modulation. Les expériences ont montré que les traits caractéristiques proposés étaient robustes aux artefacts, évitant ainsi le recours aux algorithmes de MAA, tout en fournissant des informations plus précises pour le diagnostic de la MA, et potentiellement pour la surveillance de la progression de la maladie. Ces nouveaux avantages sont inestimables pour le développement d'appareils portables à bas coût et il est à espérer que les idées présentées ici pourront être utilisées pour améliorer la qualité de vie des personnes atteintes de la MA, de leurs familles et de leurs soignants.

Mots-clés: Maladie d'Alzheimer, électroencéphalographie, état de repos, modulation d'amplitude, manipulation automatisée des artefacts, EEG portable

Resumen

La enfermedad de Alzheimer (EA) es una enfermedad terminal neurodegenerativo que representa casi el 70% de los casos de demencia en todo el mundo. La incidencia de demencia global se calcula en 75 millones de casos para el año 2030, con la mayoría de las personas afectadas provenientes de países de bajo y medio ingreso. Aunque no existe una cura para la EA, un diagnóstico temprano puede mejorar la calidad de vida de los pacientes con Alzheimer y las personas que los cuidan. Actualmente, el diagnóstico de la EA se lleva a cabo mediante exámenes de estado mental, estudios costosos de neuroimagen y pruebas de laboratorio que son invasivas, todo lo anterior hace que el diagnóstico lleve mucho tiempo y sea costoso. No obstante, en la última década la electroencefalografía (EEG), específicamente el EEG en reposo (rsEEG), ha sido considerada como una técnica alternativa para el diagnóstico de la EA con la cual se pueden obtener una exactitud similar a las obtenidas con técnicas de neuroimagen más costosas, como la resonancia magnética (MRI), tomografía computarizada (TC) y tomografía por emisión de positrones (PET). Sin embargo, el uso de rsEEG para el diagnóstico de la EA presenta dos desventajas principales: (*i*) la dependencia en segmentos "sin artefactos", que son seleccionados manual y meticulosamente por médicos expertos y (*ii*) la necesidad de dispositivos EEG de grado médico y de investigación, a menudo con más de 16 electrodos, aspecto que los hace difíciles de transportar y costosos de financiar, especialmente para los países de bajo y mediano ingreso. En esta tesis doctoral, presentamos los pasos hacia el desarrollo de un sistema automatizado portátil y de bajo costo basado en rsEEG para el diagnóstico de la EA. Para alcanzar este objetivo, se han desarrollado tres principales innovaciones.

Primero, exploramos los efectos de varios métodos de manipulación (totalmente) automatizada de artefactos (MAA) en las señales de rsEEG y reportamos sus ventajas y desventajas de su uso en el diagnóstico automático de la EA. El resultado de esta exploración mostró que el diagnóstico de EA basado en señales de rsEEG mejoradas con MMA está en línea con el rendimiento obtenido con datos de EEG "sin artefactos", lo cual sugiere que se pueden evitar la intervención de humanos expertos y el desecho de señales de EEG (con artefactos). En segundo lugar, evaluamos y comparamos el uso de dispositivos de EEG de baja densidad (7 canales) para los protocolos experimentales de ojos abiertos y ojos cerrados en rsEEG para el diagnóstico de la EA. Su desempeño se comparó con el de un sistema típico de densidad media (20 canales). Por último, demostramos que las características convencionales de EEG propuestas en la literatura no solo son sensibles a artefactos, sino que, se basan en información extraída de subbandas de frecuencia de EEG que son subóptimas para el diagnóstico de la EA. Como tal, propusimos un nuevo conjunto de características de EEG basadas en la técnica del espectrograma de modulación. Los experimentos mostraron que las características propuestas son robustas a artefactos, evitando así la necesidad de algoritmos de MAA, también proporcionan información más discriminatoria no solo para el diagnóstico de la EA, sino también para el monitoreo de la progresión de la enfermedad. Estos nuevos beneficios son invaluables para el desarrollo de dispositivos EEG portátiles de bajo costo y se espera que las ideas presentadas en esta tesis puedan ser utilizadas para mejorar la calidad de vida de las personas afectadas por la EA, sus familias y cuidadores.

Palabras claves: Enfermedad de Alzheimer, electroencefalografía, estado de reposo, modulación de amplitud, manipulación automática de artefactos, EEG portátil

Contents

List of Figures

List of Tables

Liste des Figures

Liste des Tableaux

List of Abbreviations

AA	Alzheimer's Association
AAH	Automated artifact handling
AAR	Automated artifact removal
aBSS	Automated BSS
AD	Alzheimer's disease
ADNI	Alzheimer's disease neuroimaging initiative
ADRDA	Alzheimer's Disease and Related Disorder Association
AM	Amplitude modulation
AUC	Area under the (ROC) curve
BA	Brodmann area
BCI	Brain-computer interface
BSS	Blind source separation
BSS	Blind source separation
CCA	Canonical correlation analysis
CDR	Clinical Dementia Rating
CSD	Current source density
CSF	Cerebrospinal fluid
CT	Computed tomography
CV	Cross-validation
CWT	Continuous wavelet transform
ECG	Electrocardiography
EEG	Electroencephalography
EGT	Eye-gaze tracking
eLORETA	Exact low-resolution electromagnetic tomography
EMG	Electromyography
EOG	Electrooculography
ERD	Event-related desynchronization
ERO	Event-related oscillations
ERP	Event-related potential
ERS	Event-related synchronization
FIR	Finite impulse response

fNIRS	functional near-infrared spectroscopy
FT	Fourier transform
GUI	Graphical user interface
HT	Hilbert transform
IC	Independent component
ICA	Independent component analysis
ICA	Independent component analysis
IFT	Inverse Fourier transform
IIR	Infinite impulse response
IMU	Inertial meassurement unit
LDA	Linear discriminant analysis
LORETA	Low-resolution brain electromagnetic tomography
LOSO	Leave-one-subject-out
MCI	Mild cognitive impairment
MMSE	Mini-mental state examination
MNI	Montreal Neurological Institute
MRI	Magnetic resonance imaging
MuLES	MuSAE Lab EEG server
MuSAE Lab	Multimedia/multimodal signal analysis and enhancement Lab
NIA	National Institute on Aging
NINCDS	National Institute of Neurological and Communication Disorder and Stroke
NIRS	Near-infrared spectroscopy
Nold	Healthy normal elderly controls
PCA	Principal component analysis
PET	Positron emission tomography
PPG	Photoplethysmogram
PSD	Power spectrum density
ROC	Receiver operating characteristic
rsEEG	Resting-state EEG
RVM	Relevance vector machine
SAR	Statistical artifact rejection
sLORETA	Standardized low-resolution electromagnetic tomography
SnPM	Statistical non-parametric mapping
SNR	Signal-to-noise ratio
SOBI	Second order blind identification
STFT	Short-time Fourier transform
SVM	Support vector machine
VR	Virtual reality
wICA	Wavelet-enhanced ICA

Synopsis

0.1 Introduction

Le terme de démence est utilisé pour englober un certain nombre de maladies neurodégénératives qui ont pour origine des lésions cérébrales et la mort de neurones. La progression de la démence entraîne un déclin et, par conséquent, une perte des fonctions cognitives (par exemple, de la mémoire, du raisonnement et de la communication) et comportementales qui entravent la vie quotidienne d'un individu. Parmi les troubles classés comme démence, la maladie d'Alzheimer (MA) est la forme la plus courante, représentant près de 70% des cas de démence dans le monde. La MA est fatale et, à ce jour, il n'existe pas de traitement, mais uniquement des traitements palliatifs qui ralentissent temporairement la progression des symptômes, visant ainsi à améliorer la qualité de vie des patients, de leur famille et des soignants [2, 3, 4]. En 2015, 46,8 millions de personnes vivaient avec un type de démence dans le monde et ce nombre devrait atteindre 74,7 millions d'ici 2030 et 131,5 millions d'ici 2050 [3], avec des projections similaires pour le Canada [5].

La plupart de ces cas de démence (environ 65%) auront lieu dans des pays à revenus faibles ou intermédiaires, comme le montre la Figure 1.1. De nos jours, le diagnostic définitif de la maladie d'Alzheimer n'est possible que post-mortem lorsque l'analyse révèle les lésions cérébrales structurelles caractéristiques de la maladie. Les critères de diagnostic clinique actuels de la MA ont été mis au point par l'Institut national sur le vieillissement (National Institute on Aging) et l'Association Alzheimer (NIA-AA) [6, 7, 8, 9]. Outre l'utilisation de dossiers médicaux et d'examens neurologiques tels que le *mini-mental state examination* (MMSE) [10] et le test clinique de démence (CDR) [11], les directives actualisées incluent l'utilisation de biomarqueurs dérivés du liquide cérébro-spinal (LCR) et de neuroimagerie pour soutenir le diagnostic de la MA chez les individus symptomatiques [6]. L'obtention d'un échantillon de LCR nécessite une ponction lombaire, faisant de la mesure de ces biomarqueurs une approche invasive et peu pratique, tandis que les outils de neuroimagerie sont coûteux, prennent du temps et nécessitent l'intervention d'experts. Ces limitations entravent l'utilisation de ces techniques dans la pratique clinique quotidienne pour le diagnostic de la MA, en particulier dans les pays à revenus faibles et moyens. Les biomarqueurs basés sur l'électroencéphalographie (EEG) sont apparus comme des outils prometteurs dans l'étude de la maladie d'Alzheimer, entraînés par les inconvénients et les limites des biomarqueurs dérivés du LCR et de la neuroimagerie.

Électroencéphalographie

L'EEG consiste à enregistrer les changements du potentiel électrique mesurés au niveau du cuir chevelu de l'individu avec des électrodes. Ces changements ont pour origine l'activité électrique provoquée par l'activation synchrone de milliers de neurones d'orientation spatiale similaire, appelés *dipôles*, dans le cortex cérébral, comme le montre la Figure 1.2, [12, 1]. Les potentiels électriques sont mesurés entre des électrodes placés sur différents points du cuir chevelu et une électrode de référence située électriquement «loin» des sources d'intérêt corticales. Les emplacements communs de l'électrode de référence comprennent la moyenne des mastoïdes, la moyenne des lobes d'oreille et le cou [1, 13]. Pour éviter les variations entre les sujets avec différentes tailles et formes de têtes, des emplacements standard ou des positionnements d'électrodes ont été proposés, parmi lesquels le système international 10-20 est le positionnement le plus utilisé (voir Figure 1.3a). Les potentiels électriques mesurés sur le cuir chevelu, comme le montre la Figure 1.3b, présentent des amplitudes $< 100\ \mu$V et sont généralement numérisés à des fréquences d'échantillonnage supérieures à 200 Hz. De ce fait, l'EEG présente une meilleure résolution temporelle que les autres techniques de neuroimagerie [14]. Les signaux EEG sont traditionnellement divisés en cinq bandes de fréquences principales, soit delta (δ) 0,1-4 Hz, thêta (θ) 4-8 Hz, alpha (α) 8-12 Hz, bêta (β) 12-30 Hz et gamma (γ) $>$ 30 Hz. Cette décomposition est illustrée dans le domaine temporel à la Figure 1.3c, et son équivalent en fréquence à la Figure 1.3d. Contrairement aux autres biopotentiels, tels que le signal d'électrocardiographie (ECG), les signaux EEG sont rarement analysés visuellement, ce qui nécessite un traitement du signal supplémentaire pour identifier des motifs et extraire des informations précieuses des enregistrements EEG [15, 13].

L'EEG dans l'étude de la MA

Puisque les signaux EEG ont leur origine dans l'activité sous-jacente du cortex cérébral, des biomarqueurs basés sur l'EEG peuvent être utilisés pour déduire la dégénérescence neuronale et le déclin du nombre de synapses causés par la progression de la MA [16, 17]. Ainsi, l'EEG a suscité l'intérêt des chercheurs pour l'étude et le diagnostic de la MA. En outre, les signaux EEG ont été étudiés chez des personnes âgées en bonne santé, montrant qu'il n'y a pas de modifications substantielles de l'EEG associées au vieillissement en santé, faisant de l'EEG une technique appropriée pour évaluer les déficiences fonctionnelles causées par la MA [16]. En effet, les biomarqueurs basés sur l'EEG ont le potentiel de servir de support et/ou d'alternative aux biomarqueurs existants (par exemple, LCR et neuroimagerie), avec l'avantage d'être non invasifs, moins coûteux et potentiellement portables. Au cours des dernières décennies, de nombreuses études ont exploré les effets de la MA et de sa progression sur les signaux EEG. Ces études ont utilisé des signaux EEG collectés dans un certain nombre de conditions différentes, relevant généralement de deux classes: les enregistrements au repos et les enregistrements liés à des événements. L'EEG au repos (rsEEG) consiste en l'activité enregistrée en l'absence de tout type de stimulus, mesurant ainsi l'activité cérébrale endogène [18, 15]. Avec l'enregistrement rsEEG, le participant n'exécute aucune tâche, par conséquent, l'acquisition d'EEG devient plus simple, plus confortable et moins stressante pour le participant que l'enregistrement lié à des événements. Les enregistrements rsEEG ont donc été largement utilisés dans l'étude de la MA basée sur l'EEG.

Défis pour le diagnostic de la MA à base d'EEG

Un inconvénient majeur de l'utilisation de l'EEG est que les signaux sont soumis à des interférences provenant d'autres signaux. Collectivement, ces signaux interférents sont appelés artefacts. Certaines sources d'artefacts communes comprennent les mouvements oculaires, les clignements de yeux, l'activité cardiaque, l'activité des muscles crâniens, le mouvement des électrodes et les interférences du réseau électrique [1, 15, 19, 20]. Ces artefacts ont des effets néfastes sur la qualité du signal EEG et par conséquent sur la précision du diagnostic de la MA. Ainsi, la majorité des études publiées se sont appuyées sur des segments ou des époques d'EEG «sans artefact», sélectionnés manuellement grâce à une inspection visuelle minutieuse effectuée par des cliniciens experts. Cependant, la sélection manuelle des époques sans artefacts est un processus fastidieux, long et coûteux qui introduit des biais humains et élimine une grande quantité de données EEG enregistrées [20]. Pour surmonter ce problème, des méthodes de manipulation des artefacts peuvent être utilisées pour améliorer la qualité du signal ou réduire la dépendance à l'inspection visuelle humaine. Alternativement, de nouveaux traits caractéristiques robustes aux artefacts peuvent être développés pour une analyse améliorée de la MA. De plus, les dispositifs EEG de qualité médicale et de recherche généralement utilisés pour les études de la MA ont 16 électrodes ou plus (souvent 64+), ce qui les rend difficiles à transporter et coûteux, en particulier pour les pays à revenus faibles ou intermédiaires. Les progrès technologiques, cependant, au cours des dernières années, ont abouti à des dispositifs EEG commerciaux portables, abordables et sans fil capables d'enregistrer et d'analyser des signaux EEG avec des ordinateurs portables, tablettes ou téléphones intelligents [21, 22]. De tels progrès ouvrent la voie à des systèmes de diagnostic de la MA portables basés sur l'EEG, peu coûteux, qui peuvent avoir un impact aussi bien dans les pays en développement que dans les régions éloignées. À ce titre, la faisabilité de tels systèmes devrait être explorée.

0.1.1 Contributions de la thèse

L'objectif principal de cette thèse de doctorat est de développer un système d'analyse EEG portable, peu coûteux et automatisé pouvant être utilisé par les cliniciens du monde entier pour améliorer le diagnostic de la MA via un protocole expérimental simple au repos. Pour atteindre cet objectif, plusieurs innovations ont dû être développées, constituant ainsi les principales contributions de cette thèse. Plus précisément, trois innovations principales ont été proposées, développées et évaluées.

1. Afin d'éliminer le besoin d'intervention humaine experte pour la collecte d'EEG sans artefacts, cette thèse est la première à explorer les effets de plusieurs algorithmes de manipulation d'artefacts entièrement automatisés sur les signaux rsEEG et à évaluer leurs avantages et inconvénients pour le diagnostic automatisé.
2. Afin d'explorer le potentiel des dispositifs portables à densité basse et des protocoles d'enregistrement au repos, cette thèse est la première à comparer les changements dans les protocoles expérimentaux à yeux ouverts et à yeux fermés sur la précision diagnostique, ainsi que d'évaluer les différences de performance entre un système automatisé à 20 canaux et un système portable à 7 canaux.
3. S'appuyer sur des traits caractéristiques conventionnels d'EEG pour le diagnostic peut être problématique, car les informations discriminatoires peuvent être supprimées par les algorithmes de traitement des artefacts ou par le nombre réduit de canaux disponibles. Ici, une nouvelle classe de traits caractéristiques dérivée d'une représentation spectrotemporelle des signaux est présentée et (*i*) offre une robustesse améliorée contre les artefacts, (*ii*) évite potentiellement le besoin d'une étape de suppression d'artefact séparée, et (*iii*) fournit de meilleures informations discriminatoires non seulement à des fins de diagnostic de la MA, mais également pour la surveillance de la progression de la maladie.

Ces trois innovations ont été décrites dans plusieurs manuscrits; une liste détaillée de ces manuscrits se trouve à la Section 1.6.

0.1.2 Organisation de la thèse

Ce chapitre d'introduction, le Chapitre 1, a décrit le diagnostic actuel de la MA et le rôle de l'EEG en tant que méthode alternative, a défini les défis liés au diagnostic de la MA basé sur l'EEG et, enfin, a défini l'objectif général de cette thèse de doctorat. Dans le Chapitre 2, une évaluation des techniques rsEEG de pointe pour la MA est présentée, en mettant l'accent sur le pipeline généralement utilisé pour le diagnostic de la MA, y compris le prétraitement, l'extraction d'époques, l'extraction de traits caractéristiques EEG, la sélection de traits caractéristiques et la classification. Le Chapitre 3 élargit le concept d'analyse par modulation d'amplitude des signaux biologiques, son cadre théorique et son application potentielle sur les signaux rsEEG; ce chapitre sert de base aux nouveaux traits caractéristiques proposés plus loin dans le document. Dans le Chapitre 4, les effets néfastes des artefacts EEG sur le diagnostic de la MA sont étudiés et les avantages et les inconvénients des algorithmes automatisés de gestion des artefacts sur les performances de diagnostic AD sont explorés. Ensuite, le Chapitre 5 présente les résultats obtenus lorsque des dispositifs EEG portables à faible densité sont utilisés. Les protocoles expérimentaux à yeux ouverts et à yeux fermés sont également comparés et leurs effets sur la précision du diagnostic de la MA sont quantifiés. Dans le Chapitre 6, nous décrivons le développement de nouveaux traits caractéristiques robustes aux artefacts basés sur l'analyse de la modulation d'amplitude des signaux rsEEG. Nous validons l'utilité des traits caractéristiques proposés par la classification de quatre sous-tâches diagnostiques (saine ou «Nold» contre MA, saine contre MA légère, MA légère contre MA modérée, et saine contre MA légère contre MA modérée). Enfin, le Chapitre 7 présente les conclusions générales de cette thèse, ainsi que les futurs domaines de la recherche.

0.2 Chapitre 2: Diagnostic de la MA à base d'EEG de pointe

Au début de 2018, nous avons effectué une étude complète sur l'utilisation de la rsEEG pour l'étude de la MA. Au total, 112 articles de revues publiés entre janvier 2010 et février 2018 ont été rassemblés et examinés méticuleusement dans le but de comparer les éléments cruciaux d'un système de diagnostic de la MA basé sur la rsEEG. Plus précisément, des éléments tels que l'acquisition du signal, le protocole expérimental, le prétraitement, la manipulation des artefacts, l'extraction des traits caractéristiques et la classification ont été étudiés. De plus, la revue systématique a mis en évidence des pratiques communes, des différences et des consensus dans l'utilisation de la rsEEG, des limitations rapportées et des recommandations pour des études futures [23]. Ce chapitre donne un aperçu des effets généralement rapportés de la MA sur le signal rsEEG, suivi de la description de la structure générale d'un système basé sur la rsEEG pour le diagnostic de la MA et de ses éléments constitutifs; chacun de ces éléments est ensuite abordé en fonction des résultats de la revue de littérature mentionnée.

0.2.1 Effets de la MA sur les signaux rsEEG

Avec l'adoption de l'analyse quantitative des données EEG, au cours des deux dernières décennies, plusieurs travaux ont exploré les anomalies de la rsEEG liées à la MA. Une analyse approfondie de ces anomalies peut être trouvée dans [17, 24]. Quatre effets majeurs de la MA et de sa progression sur les signaux rsEEG ont été rapportés à plusieurs reprises.

1. *Ralentissement.* Le spectre de puissance des signaux rsEEG passe des composantes haute fréquence (alpha, bêta et gamma) aux composantes basse fréquence (delta et thêta). Le degré de changement de puissance s'est révélé proportionnel à la progression de la MA [25, 26]. Le ralentissement de l'EEG serait la conséquence de la perte d'innervation cholinergique chez les patients atteints de la MA [27].
2. *Diminution de la synchronisation.* Perçue comme une réduction de la connectivité entre les régions corticales, une diminution de la synchronisation a été rapportée chez les patients atteints de la MA. L'origine de ce phénomène n'est pas encore bien comprise, bien que l'on

pense qu'elle est liée à l'atrophie dans la communication des réseaux neuronaux [28, 29, 30, 31].

3. *Complexité réduite.* Une diminution de la complexité globale de l'activité électrique du cerveau a été observée chez les patients atteints de MA par rapport aux témoins sains [32, 17, 33]. Cette diminution est probablement causée par la mort neuronale massive et la réduction des connexions non linéaires entre les régions corticales, conduisant à une dynamique d'EEG plus simple (moins complexe).
4. *Déficit neuromodulateur.* Des preuves expérimentales récentes [34, 35] ont suggéré un déficit neuromodulateur dans la MA, qui pourrait avoir pour origine la réduction des neurotransmetteurs dûe à des dommages dans les voies cérébrales au cours de la MA. De ce fait, une analyse de modulation a récemment été proposée pour quantifier le comportement non stationnaire dans rsEEG [36].

Bien que ces effets soient souvent considérés indépendamment, il est important de noter qu'ils ont pour origine le même phénomène, c.-à-d. la perte de neurones dans la MA qui perturbe la connectivité cérébrale anatomique au niveau des réseaux fonctionnels [37, 33, 17]. Diverses méthodologies ont été proposées pour étudier et quantifier les effets dans le but final de pouvoir diagnostiquer la MA à partir des signaux rsEEG. Bien que les méthodologies proposées soient différentes à de nombreux égards, toutes peuvent être considérées comme ayant une structure similaire.

0.2.2 Système pour le diagnostic de la MA à base de la rsEEG

En général, un système de diagnostic de la MA basé sur les signaux rsEEG peut être imaginé suivant la structure décrite à la Figure 2.1. Tout d'abord, les signaux EEG sont acquis sous un protocole expérimental spécifique qui décrit le statut du participant, le périphérique EEG et la durée de l'enregistrement. Deuxièmement, au stade du prétraitement, les signaux EEG enregistrés sont filtrés avec un filtre passe-bande afin de supprimer les artefacts. De plus, dans cette étape, d'autres méthodes pour rejeter et/ou supprimer des artefacts sont implémentées. Après l'extraction des traits caractéristiques, les signaux EEG prétraités sont divisés en époques. Pour chaque époque, les traits caractéristiques sont calculés pour quantifier un ou plusieurs des effets de la MA dans les signaux EEG. Enfin, au stade de la traduction des traits caractéristiques, les traits caractéristiques calculés sont utilisés pour déduire la présence ou la progression de la MA.

Protocole expérimental

Le protocole expérimental se réfère à l'ensemble des éléments décrivant l'acquisition des signaux EEG, c.-à-d., les conditions d'enregistrement, la durée de l'enregistrement et le nombre de canaux. La condition d'enregistrement la plus courante est celle des yeux fermés, dans laquelle le participant est confortablement assis avec les yeux fermés. Cette condition a été explicitement rapportée dans

109 des articles examinés; elle est en effet considérée comme une procédure standardisée pour la rsEEG [38]. Étant donné la population cible dans les études de la MA, la durée d'enregistrement devient un facteur critique pour le confort du participant et, par conséquent, pour la conformité de l'enregistrement. Les valeurs rapportées allaient de 2 à 33 minutes, avec une durée moyenne 10 minutes. Notez que ces temps n'incluent pas le temps de configuration qui est proportionnel au nombre d'électrodes utilisées pour l'enregistrement rsEEG. La décision concernant le nombre d'électrodes dépend du compromis entre la résolution spatiale et le confort des participants. Les systèmes EEG avec 32 canaux ou plus sont encombrants et leur mise en place et leur réglage peuvent durer une heure, voire plus, pour le personnel expert en EEG [39, 40]. En outre, un long temps de préparation peut provoquer des états cognitifs indésirables tels que la somnolence, la fatigue, la frustration ou le stress chez les participants plus âgés; ces états cognitifs induits peuvent altérer le signal rsEEG et présenter ainsi des effets néfastes pour le diagnostic de la MA. Une autre raison de prendre en compte le nombre d'électrodes est l'utilisation d'outils de localisation de source EEG pour estimer l'emplacement approximatif de l'activité électrique dans le cerveau. Le nombre d'électrodes utilisées pour l'acquisition du signal EEG dans les études examinées variait considérablement, allant de 1 à 256 électrodes, 19 électrodes étant le nombre le plus commun (utilisé par 53 articles). L'impact du nombre d'électrodes sur les performances de diagnostic est exploré plus en détail au Chapitre 5.

Prétraitement du signal EEG

Au sens large, le prétraitement du signal EEG représente les manipulations effectuées sur les données brutes acquises afin de le préparer à l'extraction de traits caractéristiques [41, 13, 15]. L'objectif principal du prétraitement est d'améliorer la qualité du signal EEG en éliminant les artefacts, car ils ont des effets néfastes sur les analyses ultérieures [42].

Bande passante. Le filtrage (numérique) passe-bande linéaire, invariant dans le temps, est de loin la technique de prétraitement EEG la plus utilisée. Son utilisation repose sur l'hypothèse que les artefacts et l'EEG ne partagent pas de composantes spectrales, ainsi il est possible de concevoir un filtre égal à la bande passante EEG de telle sorte que seules les données EEG soient conservées [15, 1, 43]. Alors que les limites inférieure et supérieure de la bande passante dépendent des composantes spectrales d'intérêt pour une étude donnée, généralement pour les signaux EEG la limite inférieure se situe entre 0,1 et 4 Hz et vise à éliminer la dérive de base des signaux EEG. La limite supérieure varie quant à elle de 20 à 200 Hz et est choisie en fonction du compromis entre la fréquence supérieure d'intérêt et la réduction des artefacts électromyographiques à haute fréquence (EMG). Un aspect crucial de l'utilisation des filtres numériques pour l'EEG est leur implémentation, soit la réponse impulsionnelle infinie (RII) ou la réponse impulsionnelle finie (RIF). L'une des principales différences est que les filtres RIF peuvent être conçus pour avoir une réponse en phase linéaire, c.-à-d. que la forme temporelle du signal avec des composantes spectrales dans la bande passante n'est pas déformée par le filtrage. Une analyse détaillée de l'utilisation du filtrage numérique des signaux électrophysiologiques peut être trouvée dans [43]. Malheureusement, les artefacts et l'EEG partagent généralement des composantes spectrales; ils ne peuvent donc pas être séparés par un filtrage passe-bande du signal EEG. De ce fait, différentes stratégies de manipulation des artefacts doivent être utilisées pour réduire l'impact des artefacts sur le signal EEG [44, 15].

Manipulation des artefacts. Après le filtrage de la bande passante, plusieurs artefacts sont présents dans les signaux EEG, donc un traitement supplémentaire est nécessaire. Trois approches principales sont généralement suivies pour la manipulation des artefacts: ignorer, rejeter ou supprimer les artefacts. Ignorer les artefacts n'est normalement considéré que dans les applications en temps réel, comme dans le cas des interfaces cerveau-ordinateur (ICOs); dans l'approche de rejet, des segments EEG artéfactuels sont identifiés et éliminés des étapes de traitement ultérieures; enfin, la suppression des artefacts vise à réduire ou à éliminer l'influence des artefacts afin de préserver autant de données EEG que possible, même dans le cas d'un chevauchement spectral. En règle générale, les études EEG se sont appuyées sur le rejet manuel des artefacts, c'est-à-dire qu'une inspection visuelle minutieuse des signaux EEG est effectuée par des experts afin d'identifier et d'éliminer les segments EEG artificiels. En fait, la majorité des articles examinés, soit 65, reposaient sur cette sélection manuelle d'EEG «sans artefact». De plus, une telle dépendance vis-à-vis des experts humains entrave les avantages en termes de coûts liés à l'utilisation des signaux EEG dans l'étude de la MA. En guise d'alternative, d'autres méthodes ont été proposées pour réduire l'intervention humaine dans le processus de manipulation des artefacts. Si l'intervention humaine est requise, ces méthodes sont classées comme «semi-automatisées»; autrement, on parle de méthodes «automatisées». Les méthodes de séparation aveugle de source (BSS) sont les plus utilisées pour la suppression semi-automatisée et automatisée des artefacts. La documentation sur la gestion des artefacts EEG est vaste, [45, 42, 20, 46, 47], néanmoins, il n'y a pas de consensus sur les meilleures approches pour réduire l'influence des artefacts tout en conservant autant de données EEG que possible. Toutefois, il est généralement admis que la qualité et la quantité des données EEG conservées sont essentielles pour éviter les sessions d'enregistrement longues et fatiguantes. Dans le Chapitre 4, une évaluation des différentes approches de manipulation automatisée des artefacts (MAA) est fournie dans le contexte du diagnostic de la MA basé sur la rsEEG. En outre, une discussion sur les avantages, les inconvénients et les défis de ces différentes approches est fournie.

Localisation de sources cérébrales. Étant donné que les enregistrements EEG ont pour origine l'activité neuronale électrique à l'intérieur du cerveau, l'analyse des signaux EEG observés au niveau du cuir chevelu permet d'estimer l'activité cérébrale électrique générant l'EEG observé. L'estimation de l'activité cérébrale à partir des signaux EEG est appelée localisation de sources (cérébrales) ou problème inverse EEG. Parmi les diverses méthodes utilisées pour résoudre le problème inverse de l'EEG, la tomographie électromagnétique cérébrale à basse résolution (LORETA) et ses variantes sont les plus populaires [48]. L'utilisation de méthodes de localisation des sources est fréquente dans l'étude de la MA, car ces méthodes fournissent des informations sur les sources actives dans le cerveau, en aidant à identifier les anomalies liées à la présence cérébrale ou à la progression de la maladie. Parmi les articles examinés, dix-sept ont utilisé la localisation de sources; parmi ceux-ci, douze utilisaient un positionnement avec 19 électrodes, le reste utilisant des positionnements avec 32 électrodes ou plus. Il est important de noter qu'un plus grand nombre de canaux améliore généralement la localisation des sources [49, 39], mais a des effets négatifs sur l'aspect pratique de la configuration de l'expérience.

Extraction de traits caractéristiques EEG

L'extraction de traits caractéristiques consiste en l'ensemble des techniques traitant les signaux EEG pour obtenir des caractéristiques quantitatives (traits caractéristiques) qui sont des indicateurs prouvés ou potentiels de la présence ou de l'absence d'un phénomène donné dans l'activité cérébrale [50, 41]. En règle générale, les traits caractéristiques de rsEEG proposés pour l'étude de la MA visaient à quantifier l'un des effets signalés de la MA sur les signaux rsEEG. En tant que tels, les traits caractéristiques sont divisés en quatre catégories en fonction des effets de la MA qu'ils visent à évaluer, c.-à-d.: le ralentissement, la complexité réduite, la diminution de la synchronisation ou le déficit neuromodulateur. Dans les articles examinés, il était courant d'observer l'utilisation de caractéristiques visant à évaluer les différents effets de la MA sur le signal EEG dans le même article.

Traduction de traits caractéristiques EEG

La traduction de traits caractéristiques représente l'ensemble des actions effectuées sur les traits caractéristiques EEG extraites dans le but de créer des modèles pour: (*i*) évaluer les corrélations entre les traits caractéristiques et la progression de la MA et/ou (*ii*) effectuer la classification entre les participants Nold et souffrant de la MA, c.-à-d. le diagnostic. Dans le cas de la tâche de classification, la traduction des traits caractéristiques est normalement divisée suivant les étapes suivantes: sélection des traits caractéristiques, validation croisée et classification.

Sélection de traits caractéristiques. L'objectif de la sélection de traits caractéristiques est de sélectionner un sous-ensemble de traits caractéristiques pour résoudre les problèmes liés aux données de haute dimension lors de l'étape de classification, car elle supprime les traits caractéristiques redondants ou non pertinents, réduisant ainsi la complexité de l'algorithme de classification ce qui, en général, aide à éviter le surapprentissage dans le classifieur [51]. Dans la littérature sur la MA, les traits caractéristiques sont généralement classés en fonction de leur valeur prédictive individuelle, telle que leur valeur-p. Une évaluation de différentes méthodes de sélection des traits caractéristiques dans le contexte du diagnostic de la MA basé sur la rsEEG peut être trouvée dans [52].

Validation croisée. Avec une quantité limitée de données pour entraîner et tester les algorithmes de classification, le surapprentissage peut se produire lorsque les mêmes données sont utilisées pour l'entraînement et les tests. Un moyen d'éviter cela consiste à diviser les données disponibles en deux ensembles, soit un pour chaque tâche. Cependant, les données sélectionnées pour l'entraînement (ou les tests) peuvent ne pas être représentatives, conduisant à des résultats biaisés. Un moyen de réduire le biais introduit par la partition de données consiste à répéter plusieurs fois la partition de différentes manières. Ce processus est appelé validation croisée (CV). L'une des méthodes de CV les plus utilisées est le 10-fold CV, où les données disponibles sont divisées de manière aléatoire en 10 partitions, 9 partitions étant utilisées pour entraîner le classifieur et une autre pour les tests. Ce processus est répété 10 fois et le résultat est obtenu en combinant les résultats obtenus pour chacune des partitions de test. Bien que l'utilisation du 10-fold CV permet d'estimer la performance généralisée du système de classification proposé, il est sujet à des biais optimistes en raison de la sélection aléatoire des partitions de données, car des échantillons de données provenant du même sujet peuvent être trouvés dans les partitions d'entraînement et de tests pour le même pli. En conséquence, le classifieur est formé et testé sur des données non indépendantes mais fortement corrélées. Un moyen de réduire ces biais est d'utiliser la CV avec exclusion d'un sujet (LOSO), dans lequel, dans un ensemble de données constitué de données provenant de N participants, les données de N-1 sujets sont utilisées pour l'entraînement des classifieurs alors que les données du sujet restant sont utilisées pour les tests, ce processus étant répété pour chaque participant de l'ensemble de données.

Algorithme de classification. Le rôle d'un algorithme de classification ou d'un classifieur est d'apprendre à partir de données le modèle ou la fonction de transfert entre les vecteurs de traits caractéristiques et les étiquettes. Comme l'intérêt porte sur le diagnostic par sujet, une fois que les étiquettes ont été obtenues pour chaque vecteur de caractéristiques, les étiquettes associées à un sujet donné doivent être combinées pour fournir une étiquette par sujet. Selon le type de sortie fourni, les classifieurs peuvent être divisés deux groupes : informatif ou discriminatif. Les classifieurs informatifs apprennent les modèles de classe : donc, pour classifier un vecteur de traits caractéristiques, la probabilité de chaque classe est calculée et la plus probable est choisie.

0.2.3 Discussion

L'utilisation de la rsEEG pour l'étude de la MA repose principalement sur sa simplicité et sur le faible impact qu'elle représente pour le confort des participants âgés, qui souffrent souvent de démence. Cependant, ce confort est inversement proportionnel à la durée totale de la session qui est composée des temps de configuration et d'enregistrement. Un moyen simple de minimiser la durée d'enregistrement consiste à améliorer les techniques de manipulation des artefacts afin d'éviter de devoir compter sur de longues sessions pour compenser la quantité de données EEG supprimées en raison des artefacts. L'utilisation de méthodes semi-automatisées pour l'élimination des artefacts a donné des résultats prometteurs, mais elle compromet les avantages de l'EEG concernant son faible coût, car l'intervention d'experts humains est toujours nécessaire. Par conséquent, une attention particulière doit être accordée à l'évaluation des techniques MAA. De plus, une grande diversité de traits caractéristiques rsEEG a été proposée pour l'étude de la MA, mais leur robustesse en présence d'artefacts ou de méthodes d'élimination d'artefacts n'a pas été explorée. Un plus grand nombre d'électrodes permet une meilleure résolution spatiale pour l'étude de l'activité sous-jacente et est souhaitable pour l'extraction de traits caractéristiques basées sur la localisation de sources. Cependant, les montages à plus haute densité sont lourds, peu pratiques et impliquent une longue préparation; le temps d'installation peut être raccourci en réduisant le nombre d'électrodes. L'utilisation de ces dispositifs à densité basse n'est pas courante dans l'étude de la MA basée sur l'EEG, par exemple, parmi les articles examinés, seulement cinq utilisaient une configuration EEG avec 8 électrodes ou moins. Ainsi, les performances des systèmes à densité basse doivent être explorées plus en détails.

0.3 Chapitre 3: Analyse spectrotemporelle des signaux EEG

Ce chapitre présente les fondements théoriques et les applications existantes du domaine de l'analyse spectrotemporelle des signaux appliqués aux signaux biomédicaux et plus spécifiquement à l'EEG. Généralement, les techniques et les méthodes de traitement du signal supposent (et nécessitent fréquemment) que les signaux EEG soient stationnaires. La stationnarité est une hypothèse stricte rarement rencontrée par des signaux naturels, en tant que tels, pour des raisons pratiques, les signaux sont supposés stationnaires s'ils remplissent une définition de stationnarité plus souple appelée «stationnarité au sens large» [53]. En pratique, pour analyser des signaux non stationnaires avec des outils de traitement de signal conventionnels, on considère des segments de temps plus courts dans lesquels le signal peut être considéré comme stationnaire. Par exemple, les signaux rsEEG peuvent être fréquemment considérés quasi-stationnaires à des époques d'une durée d'environ 10 s, permettant ainsi l'utilisation d'outils de traitement de signal conventionnels [1, 15, 54, 13]. Par conséquent, pour analyser les signaux non stationnaires, il est nécessaire d'avoir une représentation capable d'enregistrer les changements de contenu de fréquence dans le temps, c'est-à-dire une représentation spectrotemporelle.

0.3.1 Représentation spectrotemporelle

La dynamique temporelle du signal EEG est hautement non stationnaire et présente des changements continus sur toutes les échelles de temps [55, 1], c.-à-d., son contenu spectral évolue dans le temps, ainsi, la transformée de Fourier (FT) ne décrit pas suffisamment la dynamique de ces signaux. En ce sens, une représentation spectrale dépendante du temps est nécessaire. L'idée fondamentale d'obtenir la représentation spectrotemporelle d'un signal non stationnaire est de diviser le signal en segments plus courts et d'effectuer une transformation temps-fréquence pour chaque segment. L'utilisation de la représentation spectrotemporelle des signaux EEG a été d'une grande utilité car elle permet d'explorer les caractéristiques non stationnaires du signal EEG, par exemple, les estimations de l'amplitude et de la phase instantanées obtenues avec ces représentations sont la base pour l'analyse comme la connectivité pour différentes fréquences, et les couplages croisé de fréquences puissance-puissance et puissance-phase. L'analyse de la représentation spectrotemporelle EEG a été utilisée pour étudier les potentiels évoqués (PE) [55, 13, 56], les désynchronisations liées à un événement (DRÉ) utilisées pour les ICO d'imagerie motrice [57], les études EEG du sommeil [58], et dans le cas de rEEEG éveillé pour la détection d'événements perturbant le comportement «stationnaire», tels que les crises d'épilepsie [59]. Dans le contexte de la MA, les traits caractéristiques dérivés de la transformée en ondelettes (continue ou discrète) sont couramment utilisés [60, 61, 62, 63]. D'autres approches incluent l'utilisation de modèles basés sur des «bosses» de fréquence-temps pour décrire la représentation spectrotemporelle des signaux EEG [64, 65], ou des composants obtenus avec BSS [66], avec l'objectif final de développement de traits caractéristiques ou d'évaluation de la synchronisation [65] pour faire la distinction entre les contrôles sains et les participants avec la MA. Bien que la représentation spectrotemporelle $|X(f,t)|$ soit utile pour identifier les changements spectraux temporels dans le signal EEG, elle ne fournit pas d'informations sur la nature périodique de ces changements. Le spectrogramme de modulation défini ci-après surmonte cette limitation.

0.3.2 Spectrogramme de modulation

Une extension naturelle de la représentation spectrotemporelle d'un signal est le spectrogramme de modulation, qui caractérise les changements d'amplitude dans le cadre d'une analyse de modulation d'amplitude, fournissant une représentation des périodicités de second ordre, c.-à- d. fréquences de modulation. Ces composantes de fréquence de modulation sont parfois appelées «périodicités cachées» car elles ne sont pas présentes en tant que composantes spectrales dans la représentation fréquentielle «classique». En fait, l'un des aspects qui n'a pas été largement exploré est le phénomène de modulation d'amplitude de l'EEG [67]. Une caractéristique remarquable de la rsEEG est que sa dynamique temporelle est non stationnaire et qu'elle présente des changements continus à différentes échelles de temps [68]. Ces changements sont entraînés ou affectés par divers mécanismes, y compris les effets des voies cérébrales (ou systèmes) de neurotransmetteurs tels que la dopamine, l'acétylcholine, la sérotonine, la norépinéphrine, etc. Les projections de ces voies sont largement répandues dans les zones corticales et sont très susceptibles d'être une source importante de la variabilité temporelle observée dans la dynamique de l'activité cérébrale et donc dans les enregistrements rsEEG [55, 69, 70]. L'analyse de la modulation de la rsEEG a été suggérée comme une approche prometteuse pour la caractérisation et l'évaluation de différents troubles neurologiques. Dans l'étude de la MA, par exemple, une anomalie en termes de neuromodulation a été signalée avec une origine potentielle dans les voies cérébrales altérées causées par une perte neuronale [36, 71].

0.3.3 Conclusions

Ces dernières années, l'approche dite de modulation d'amplitude s'est révélée pertinente dans l'analyse et la synthèse de signaux quasi-stationnaires et non stationnaires où l'analyse spectrale conventionnelle présente des limites. Dans ce chapitre, nous avons présenté la théorie et les applications liées à l'analyse spectrotemporelle et à la modulation d'amplitude des signaux EEG. De plus, le concept de spectrogramme de modulation a été décrit puis présenté comme un outil utile pour l'analyse de rsEEG, car il permet de découvrir de nouvelles perspectives pour les diagnostics de la MA et de filtrer les sources de bruit qui doivent être exclues des analyses. L'analyse de modulation d'amplitude de rsEEG pour la MA est utilisée au Chapitre 6

0.4 Chapitre 4: Vers l'automatisation de l'analyse de l'EEG : effets des artefacts sur le diagnostic de la MA

La qualité et la quantité des données EEG sont compromises par la présence d'artefacts. De ce fait, les systèmes de diagnostic de la MA basés sur l'EEG reposent généralement sur la sélection manuelle par des experts de segments EEG «sans artefacts». Afin de progresser vers un diagnostic automatisé de la MA basé sur l'EEG, nous avons étudié les effets de trois algorithmes automatisés de manipulation des artefacts (seuls et en combinaison les uns avec les autres) sur des systèmes de diagnostic de la MA basés sur différentes classes de traits caractéristiques EEG : caractéristiques spectrales, taux de variation de modulation d'amplitude et cohérence.

0.4.1 Méthodologie

Cinquante-neuf participants ont été recrutés dans l'unité de neurologie comportementale et cognitive du département de neurologie et dans le centre de référence pour les troubles cognitifs à l'Hôpital das Clinicas de São Paulo, au Brésil. Le diagnostic de la MA a été réalisé par des neurologues expérimentés selon les critères NINCDS-ADRDA [72] et classé selon la version brésilienne du MMSE [73]. Les participants ont été divisés en trois groupes : le premier groupe (Nold) consistait en 24 participants normaux âgés sains sur le plan cognitif; le deuxième groupe (AD1) comprenait 20 patients atteints d'une forme légère de la MA; le troisième groupe (AD2) était composé de 15 patients présentant des symptômes de la MA modérés à graves. Les caractéristiques démographiques de cet ensemble de données peuvent être trouvées dans le Tableau 4.1. Vingt canaux EEG ont été acquis avec les participants éveillés, détendus et les yeux fermés pendant au moins huit minutes. Les électrodes ont été placées conformément au système international 10-20 dans les emplacements décrits à la Figure 4.1. En prétraitement, les enregistrements EEG ont été filtrés avec un filtre passe-bande RIF à phase zéro avec une largeur de bande de 0,5 à 45 Hz.

Trois approches automatisées de manipulation des artefacts ont été explorées dans le cadre de ce travail: le rejet statistique des artefacts (SAR), la suppression automatisée des artefacts basée sur le BSS (aBSS) et l'analyse des composantes indépendantes améliorée par ondelettes (wICA). Les résultats expérimentaux ont été obtenus pour les algorithmes de MAA et leurs combinaisons (SAR, aBSS, wICA, SAR+aBSS, SAR+wICA) sont comparées aux performances obtenues avec les données EEG «brutes», qui représentent la performance de «référence», et la performance obtenue avec un système basé sur des données EEG sélectionnées manuellement (ce système est appelé «l'étalon-or»). Quatre catégories de traits caractéristiques EEG communs ont été explorées, c.-à-d. la puissance spectrale (PSD), la cohérence de magnitude carrée (MSC), la cohérence de phase (PHA) et le taux de variation AM (MOD) récemment proposé. Une liste des traits caractéristiques calculés est présentée dans le Tableau 4.2. De plus, pour explorer la complémentarité des traits caractéristiques extraits, des ensembles de traits caractéristiques combinés ont également été étudiés. De ce fait, l'ensemble de traits caractéristiques «ALL» contenait tous les traits caractéristiques extraits et l'ensemble «PSD+MOD» était une combinaison d'ensembles de traits caractéristiques PSD et MOD, ce dernier étant motivé par les résultats récents suggérant la complémentarité des deux domaines pour la caractérisation de la MA. Comme l'objectif était de comprendre les effets des artefacts et des algorithmes de MAA sur différents ensembles de traits caractéristiques EEG et par conséquent sur les performances de diagnostic plutôt que les effets des différents algorithmes de traduction, nous avons utilisé l'algorithme de machines à vecteurs de support (SVM). L'algorithme SVM est largement utilisé dans la littérature sur le diagnostic de la MA basée en EEG [74, 75, 36, 76]. Le logiciel source libre Weka [1] a été utilisé afin de classer les traits caractéristiques en ordre d'importance suivant l'évaluation d'attributs avec une SVM, puis le classifieur SVM avec noyau polynomial, coefficient de régularisation C = 1 et coefficient de mise en forme de l'hyperplan $\gamma = 0{,}01$. Un total contigu de 25% des données disponibles pour chaque participant a été séléctionné au hasard pour la sélection des traits caractéristiques et les 75% restants ont été utilisés pour former et tester le classifieur en utilisant une validation croisée à 10 plis. La sélection des traits caractéristiques a été utilisée pour identifier les 24 traits caractéristiques les plus pertinents. Nous évaluons les performances du diagnostic de la MA pour chacune des combinaisons des sept méthodes de traitement des artefacts et des six ensembles de traits caractéristiques proposés. Les effets de la MAA sur les performances de diagnostic de la MA ont été testés sous trois tâches de classification, c.-à-d., Tâche 1: Nold vs AD1 vs. AD2, Tâche 2: Nold vs. AD1, et Tâche 3: AD1 vs. AD2. La première tâche a exploré le problème plus complexe à trois classes, c.-à-d. la distinction entre le vieillissement en bonne santé et deux étapes de la MA. La seconde, à son tour, a exploré la performance de la discrimination dans le scénario de la détection précoce. Enfin, la troisième tâche a évalué le scénario de surveillance de la progression de la maladie basé sur l'EEG. À des fins de comparaison, le système appelé «l'étalon-or» a été utilisé pour évaluer les résultats et a été obtenu en utilisant l'ensemble de traits caractéristiques «ALL» dérivé de l'ensemble de données EEG sélectionné manuellement.

0.4.2 Résultats

Les Tableaux 4.3, 4.4 et 4.5 rapportent l'exactitude obtenue avec le système de référence dans la rangée supérieure, suivies de celles obtenues avec les différents algorithmes de MAA pour les quatre traits caractéristiques ensembles et deux ensembles de traits caractéristiques combinés (c.-à-d. ALL et PSD+MOD) pour les Tâches 1, 2 et 3 respectivement. Une analyse minutieuse des

---

[1] `https://www.cs.waikato.ac.nz/ml/weka/`

tableaux présentés suggère que, pour les trois tâches, l'algorithme wICA associé aux 24 meilleurs traits caractéristiques sélectionnées dans l'ensemble ALL a donné les meilleures performances de classification. Les Tableaux 4.6 et 4.7 montrent les 24 fonctions principales pour chacune des trois tâches, respectivement pour le système standard et le système wICA-All. Les noms des traits caractéristiques sont signalés en tant que «électrode_trait-caractéristique» où «électrode» représente soit les 10 à 20 positions d'électrode (par exemple, Pz), soit le signal bipolaire virtuel (par exemple, P3-P4), et le «trait-caractéristique» est indiqué selon le Tableau 4.2.

0.4.3 Discussion

À partir des Tableaux 4.3, 4.4 et 4.5, on peut voir que l'algorithme wICA associé aux classifieurs entraînés sur les 24 principaux traits caractéristiques trouvés dans l'ensemble ALL résulte en la meilleure performance de classification. Pour la tâche à trois classes, un tel système automatisé entraînait une exactitude de classification de 78,9%, ce qui était significativement plus élevé que le hasard et conforme à ce qui avait été obtenu avec le «l'étalon-or» (83,8%). Pour la Tâche 2, l'exactitude obtenue était de 90,8%, ce qui se comparait également favorablement à la performance standard de 93,2%. Il est intéressant de noter que pour la Tâche 3, le système basé sur la wICA a surpassé «l'étalon-or», atteignant une exactitude de 96,3%. «L'étalon-or» a quant à lui atteint une précision de 92,8%. Ces résultats montrent la pertinence d'un système automatisé pour assister les cliniciens dans le diagnostic. De plus, à partir des Tableaux 4.3, 4.4 et 4.5, on peut voir que l'algorithme aBSS et sa combinaison avec la méthode SAR ont entraîné une diminution des performances sur les données brutes pour tous les ensembles de traits caractéristiques et tâches testés. Cela suggère que si aBSS peut être utilisé pour supprimer de manière fiable les artefacts oculaires [77], son traitement supprime également des informations importantes pour la discrimination basée sur les données EEG brutes.

Une fois la performance du diagnostic analysée pour toutes les combinaisons d'algorithmes de MAA et d'ensembles de traits caractéristiques, nous avons constaté que l'algorithme wICA surpassait toutes les autres méthodes. Étant donné que la méthode de validation croisée à 10 plis utilisée est sujette à des biais optimistes, il est probable que les données utilisées pour l'entraînement et le test ne sont pas disjointes. Pour éviter cette situation, nous avons évalué la tâche de classification Nold vs. MA sous validation croisée LOSO. De plus, nous avons exploré les avantages potentiels de l'utilisation d'une approche de classification informative, en utilisant l'algorithme de machine à vecteur de pertinence (RVM) comme classifieur. La RVM utilise un cadre d'apprentissage bayésien probabiliste pour trouver des classifieurs qui ont (*i*) moins de fonctions de base qu'une SVM comparable et (*ii*) l'avantage de prédire explicitement la probabilité d'appartenance à une classe, offrant ainsi aux cliniciens une source d'informations plus riche [78]. L'utilisation du classifieur RVM a montré que l'utilisation de la classification informative peut encore améliorer les performances du système de diagnostic de la MA, comme illustré dans le Tableau 4.8, en effectuant une classification mieux informée. En outre, il peut fournir un éventail plus riche d'informations aux cliniciens, permettant une évaluation plus précise et plus précoce de la MA, ainsi qu'un suivi de la progression de la maladie.

0.5 Chapitre 5: Vers l'EEG portable : effets de l'EEG de densité basse sur le diagnostic de la MA

La miniaturisation et le caractère abordable des capteurs et des circuits ont conduit au développement de dispositifs portables pour la surveillance de la santé. Plus spécifiquement, dans le domaine de l'EEG, cela a ouvert la voie à la possibilité d'acquérir et de traiter des données EEG dans des lieux autres que l'environnement clinique typique [79]. Ces dispositifs portables présentent des avantages intéressants par rapport à leurs homologues traditionnellement utilisés en recherche, tels que : (*i*) réduction de l'inconfort lors des enregistrements, permettant des enregistrements plus longs, (*ii*) puisque le câblage est éliminé, le transport de ces dispositifs facilité et, compte tenu de leur compatibilité avec des technologies de transmission de données répandues, l'enregistrement et le traitement des signaux EEG sur des dispositifs portables, (*iii*) les exigences de consommation d'énergie plus faibles ont permis des enregistrements à long terme pendant que les sujets effectuent leurs activités quotidiennes, ce qui rend pratique l'EEG ambulatoire. Les enquêtes sur les dispositifs EEG portables sont présentées dans [21, 22, 79]. Dans la recherche sur la MA basée sur l'EEG, la plupart des travaux publiés ont utilisé des montages comportant 16 électrodes ou plus. Dans ce chapitre, nous présentons l'exploration réalisée sur la combinaison de dispositifs EEG portables et la MAA sur l'analyse de rsEEG pour le diagnostic de la MA, afin d'évaluer la viabilité d'un diagnostic de la MA portable et abordable basé sur EEG.

0.5.1 Méthodologie

Récemment, l'entreprise américaine Neuronetrix a recruté des participants au cours d'une étude clinique de deux ans dans sept grands centres de traitement de la MA aux États-Unis. L'étude a été approuvée par les comités d'examen institutionnels pour chaque site et un consentement éclairé écrit a été obtenu de chaque participant à l'étude [80]. Cent quatre-vingt-quatre participants ont été répartis entre ceux qui souffrent de MA et les sujets en bonne santé. Le groupe MA était composé de 99 participants diagnostiqués selon les critères NINCSD-ADRDA et DSM-IV et présentant un score MMSE compris entre 21 et 26. Le Tableau 5.1 présente les données démographiques des participants utilisés dans cette étude. Les données EEG ont été collectées pendant une période de 3 minutes au repos avec les yeux ouverts. Le dispositif COGNISION™ à 7 canaux de Neuronetrix (Figure 5.1a) a été utilisé pour la collecte des données. Le positionnement des électrodes est présenté à la Figure 5.1b. Afin de comparer les résultats avec l'ensemble de données Neuronetrix, le montage de l'ensemble de données «Brazil» (décrit en détail à la Section 4.3.1) a été réduit afin d'avoir le même positionnement d'électrodes que l'ensemble de données Neuronetrix. Cet ensemble de données est désormais appelé «Brazil-ld». Le prétraitement du signal utilisé pour les deux ensembles de données à 7 électrodes était identique à celui décrit au Chapitre 4; de plus, motivés par les résultats présentés dans ce chapitre, nous avons utilisé l'algorithme wICA pour supprimer automatiquement les artefacts. Les traits caractéristiques extraits pour ces expériences sont listés dans le Tableau 5.2.

Dans les expériences présentées au Chapitre 4, 25% des données disponibles ont été mises de côté pour la sélection de traits caractéristiques. Pour pouvoir utiliser 100% des données disponibles pour la classification, un classifieur SVM a été utilisé avec la norme l^1 comme pénalisation, car cela présente des avantages par rapport à la norme l^2 traditionnelle. Plus précisément, l'utilisation de la norme l^1 conduit à des vecteurs de poids parcimonieux, ainsi la sélection de traits caractéristiques et la classification s'effectuent dans une seule et même étape [81]. Dans nos expériences, l'implémentation SVM du logiciel à code source ouvert scikit-learn (apprentissage automatique pour Python) [82] a été utilisée avec les paramètres suivants: kernel linéaire, pénalisation l^1 et valeur du coefficient de régularisation par défaut de C = 1. Afin d'évaluer la performance du classifieur, nous avons calculé l'exactitude avec deux approches différentes: en utilisant une validation croisée à 10 plis ou LOSO. À des fins de comparaison, nous utilisons comme «référence» les performances de classification rapportées dans le Tableau 4.8 obtenues avec l'ensemble des données Brazil, soit les données des 20 électrodes, l'approche wICA, classifieur SVM et CV LOSO. Enfin, pour tester si les traits caractéristiques présentaient une différence statistiquement significative entre les groupes AD et Nold, un test de Kruskal-Wallis avec correction post hoc Dunn-Sidak a été utilisé [83]. La signification statistique a été établie à un niveau de 1%.

0.5.2 Résultats

Le Tableau 5.2 résume les performances de classification (exactitude, sensibilité et spécificité) de la «référence» et des différentes combinaisons pour les données EEG à 7 canaux: Neuronetrix (yeux ouverts au repos) et Brazil-ld (yeux fermés au repos), en utilisant CV 10-fold et CV LOSO. En tenant compte uniquement des 35 traits caractéristiques principaux de chaque ensemble de données, le Tableau 5.2 montre ces traits caractéristiques et signale ainsi les points communs aux deux ensembles de données. Les traits caractéristiques présentant une différence significative ($p < 0{,}01$) entre le groupe témoin et le groupe MA sont suivis d'un astérisque dans le tableau. Les traits caractéristiques communs aux deux ensembles de données sont indiqués par les symboles ↑ et ↓, qui indiquent si la médiane du trait caractéristique respectif est supérieure ou inférieure dans la cohorte MA, respectivement.

0.5.3 Discussion

Comme prévu, la réduction du nombre d'électrodes, de 20 dans le système de référence à 7 dans le système proposé (Brazil-ld plus LOSO), a conduit à une diminution des performances de diagnostic de la MA. En général, les performances du système de référence (20 électrodes) sont considérablement plus élevées que celles des configurations à densité basse, ceci pouvant être attribué au fait qu'une configuration de densité plus élevée présente une distribution spatiale plus large sur le cuir chevelu, il peut ainsi enregistrer l'activité corticale d'autres régions telles que les lobes temporaux et occipitaux. Une analyse approfondie des traits caractéristiques les mieux sélectionnés au Tableau 5.2 montre que près de 50% (17 sur 35) de ces traits caractéristiques sont communs aux ensembles de données Neuronetrix et Brazil. Dans les deux ensembles de données, on peut noter que la cohorte MA présente des médianes réduites pour les traits caractéristiques de puissance spectrale correspondant aux bandes alpha et bêta, et une augmentation des médianes des traits caractéristiques de puissance spectrale dans les bandes delta et thêta par rapport à la cohorte Nold. Ce décalage dans le spectre de puissance des hautes fréquences aux basses fréquences pendant la MA est en accord avec les effets de ralentissement de la MA dans les signaux EEG précédemment rapportés dans la littérature. Néanmoins, dans [84], on rapporte une augmentation de la puissance de la bande gamma pour la cohorte AD, tandis que dans [85] et [86] l'effet inverse est observé. De tels résultats contradictoires peuvent avoir pour origine les conditions d'enregistrement de l'EEG, qui consistent à laisser les yeux ouverts dans [84] et à laisser les yeux fermés dans [85] et [86].

0.6 Chapitre 6: Nouveaux traits caractéristiques dans le domaine de la modulation pour le diagnostic de la MA

Les expériences présentées dans les Chapitres 4 et 5 se sont appuyées sur des traits caractéristiques définis par les bandes de fréquences traditionnelles de EEG, ce qui peut ne pas être optimal pour l'étude de la MA. En fait, la plupart des études publiées sur les diagnostics de la MA basés sur l'EEG ont utilisé et proposé des traits caractéristiques d'EEG définis selon les bandes d'EEG traditionnelles. Bien que l'utilisation de ces bandes de fréquences traditionnelles permette de comparer les résultats obtenus avec ceux rapportés dans la littérature [87], il se peut que dans l'étude de la MA, cette partition de fréquence ne soit pas appropriée pour les signaux EEG. Des travaux récents ont étudié l'utilisation de bandes de fréquences «optimales» dérivées de l'étude de la MA en EEG [88, 89]. En effet, les bandes de fréquences optimisées diffèrent des bandes traditionnelles, et l'utilisation des traits caractéristiques EEG dérivés de ces bandes optimisées a amélioré les performances de classification pour les deux études. Motivés par les résultats prometteurs obtenus avec l'utilisation des traits caractéristiques de taux de variation AM (définis en termes de bandes d'EEG traditionnelles) pour caractériser le déficit neuromodulateur en la MA présenté dans [36, 90], et les résultats obtenus avec le utilisation des bandes de fréquences optimisées présentées dans [88, 89], nous avons proposé l'utilisation de l'approche par spectrogramme de modulation pour analyser le signal rsEEG sans la contrainte des bandes traditionnelles.

0.6.1 Méthodologie

Les analyses exploratoires présentées dans ce chapitre ont été réalisées sur l'ensemble de données décrit dans la Section 4.3.1, qui comprend les enregistrements rsEEG à 20 canaux, plus 8 canaux bipolaires virtuels, provenant de 59 sujets appartenant à trois populations différentes, Nold, AD1 et AD2. Le prétraitement des enregistrements rsEEG était le même que celui décrit dans la Section 4.3.2 et trois versions différentes des enregistrements ont été étudiées: données EEG sélectionnées manuellement, brutes et wICA. Dans ces expériences, nous avons utilisé la représentation du domaine de modulation pour caractériser la périodicité dans les séries temporelles de puissance pour différentes fréquences des signaux EEG. Pour ce faire, la formulation du spectrogramme de modulation présentée dans la Section 3.4 est modifiée pour analyser les séries temporelles de puissance plutôt que les séries temporelles d'amplitude. Désormais, les spectrogrammes de modulation présentés dans ce chapitre sont calculés selon (6.1). La séparabilité entre deux distributions a été quantifiée en calculant l'aire sous la courbe de la fonction d'efficacité du récepteur (ROC), c.-à-d., AUC [91].

0.6.2 Spectrogramme de modulation du rsEEG pour l'évaluation de la MA

Nous avons exploré les différences en rsEEG dans le domaine de la modulation pour les enregistrements des participants Nold et AD. Pour un canal rsEEG, la représentation spectrotemporelle $X(t, f)$ a été calculée en utilisant la transformée en ondelettes continue avec l'ondelette Morlet complexe comme ondelette mère pour des fréquences de 1 à 45 Hz avec un pas de 1 Hz et $n_c = 6$. Ensuite, le spectrogramme de puissance ($|X(t, f)|^2$) a été divisé en périodes de 8 secondes et, pour chaque époque, le spectrogramme de modulation a été calculé selon (6.1). Le spectrogramme de modulation de puissance ($|X(f, f_{mod})|^2$) a été calculé pour toutes les époques de l'enregistrement. Pour permettre la comparaison des spectrogrammes de modulation de puissance obtenus entre les époques et entre les sujets, chaque spectrogramme de modulation de puissance a été normalisé par sa puissance totale, processus représenté dans 6.2. Ainsi, pour chaque sujet, une collection de spectrogrammes de modulation de puissance normalisés est obtenue pour chaque canal, comme le montre la Figure 6.3. Enfin, les spectrogrammes de modulation de puissance sont rassemblés sur tous les sujets de chaque groupe, résultant en deux collections (une par groupe) de spectrogrammes de modulation de puissance normalisés. Ensuite, pour chaque paire (f, f_{mod}) dans les spectrogrammes de modulation de puissance normalisés, l'AUC a été calculée, ce processus conduisant ainsi à une représentation des valeurs AUC dans le domaine de modulation. La Figure 6.4 décrit ce processus pour un canal. Comme le calcul des valeurs AUC a été effectué pour tous les canaux dans les enregistrements, le résultat est une carte topographique qui présente les valeurs AUC de la comparaison de groupe dans le domaine de modulation pour chaque canal dans sa position respective. La Figure 6.5 représente la carte topographique obtenue à partir de la comparaison des spectrogrammes de modulation de puissance normalisés entre les groupes Nold et MA en analysant les enregistrements rsEEG sélectionnés manuellement. En comparant les groupes Nold et MA en utilisant les données EEG brutes et améliorées par wICA, des cartes topographiques AUC similaires ont été obtenues, comme le montrent respectivement les Figures 6.6 et 6.7. Dans les cartes topographiques AUC obtenues à partir de la comparaison entre les groupes Nold et MA (Figures 6.5, 6.6 et 6.7), il est possible d'identifier des régions dans le domaine de la modulation où les valeurs AUC sont loin de 0,5. Plus précisément, il existe trois régions (R1, R2 et R3) qui regroupent les meilleures valeurs d'AUC; ces régions sont représentées à la Figure 6.8, qui correspond à la moyenne des 20 électrodes de la carte topographique AUC présentée à la Figure 6.5.

Nous explorons en outre les différences dans le domaine de la modulation entre Nold et chacun des sous-groupes MA (AD1 et AD2), et entre eux. La Figure 6.10 illustre les moyennes des électrodes obtenues à partir des comparaisons Nold vs AD1, Nold vs AD2 et AD1 vs AD2. Il est intéressant de noter que différents patrons dans le domaine de la modulation ont été observés, suggérant que cette représentation pourrait fournir des informations précieuses pour effectuer une évaluation supplémentaire de la progression de la MA. Pour évaluer le pouvoir discriminant des régions dans le domaine de la modulation, des traits caractéristiques basés sur ces régions ont été proposées et leur performance de classification a été comparée aux traits caractéristiques EEG traditionnels utilisés dans les Chapitres 4 et 5.

0.6.3 Diagnostic de la MA en utilisant les traits caractéristiques d'EEG du domaine de la modulation

Pour obtenir une métrique pour chacune des régions du spectrogramme de modulation de puissance, nous avons proposé la puissance totale de la région. En tant que tel, la puissance d'une région est définie comme l'intégrale du spectrogramme de modulation de puissance normalisé sur la région, comme décrit dans (6.2). En plus des traits caractéristiques, P_1, P_2 et P_3, dérivés des trois régions identifiées, respectivement R_1, R_2 et R_3, les ratios entre les traits caractéristiques, c.-à-d., $P_1/P_3, P_2/P_1$ et P_2/P_3 ont également été calculés. Les traits caractéristiques du domaine de la modulation (RG3) ont été extraits pour chacun des spectrogrammes normalisés obtenus à partir des époques de 8 s, pour les 28 canaux (20 électrodes + 8 signaux bipolaires virtuels). Outre les traits caractéristiques proposés, les traits caractéristiques spectraux (PSD) et AM (MOD) ont également été calculés. Le Tableau 6.2 présente une liste des traits caractéristiques calculés pour les enregistrements rsEEG sélectionnés manuellement, bruts et améliorés par wICA. Un total de 25% des données disponibles pour chaque enregistrement EEG a été défini pour effectuer la sélection des traits caractéristiques. Les 24 traits caractéristiques principaux ont été sélectionnés en fonction de la valeur F ANOVA entre l'entité et l'étiquette. Pour la classification, un classifieur SVM a été utilisé, avec les paramètres suivants: noyau linéaire, pénalisation l^1 et valeur du coefficient de régularisation par défaut de C = 1. Pour la sélection des traits caractéristiques ainsi que pour la classification, le logiciel à code source ouvert scikit-learn (apprentissage automatique pour Python) [82] a été utilisée. La performance du classifieur a été rapportée par sujet avec LOSO CV. Nous avons évalué le pouvoir discriminant des traits caractéristiques dans les trois ensembles de données rsEEG, c.-à-d., les enregistrements sélectionnés manuellement, bruts et améliorés par wICA, pour quatre tâches de classification: (*i*) Nold vs MA, (*ii*) Nold vs AD1 vs AD2, (*iii*) Nold vs AD1 et (*iv*) AD1 vs AD2. Les Tableaux 6.3 à 6.6 indiquent les performances de classification obtenues pour les tâches testées pour chaque combinaison des ensembles de traits caractéristiques et d'approche d'amélioration du signal EEG.

Une caractéristique notable des cartes topographiques AUC présentées dans les Figures 6.5, 6.6 et 6.7 est que les différences entre les groupes ne sont pas uniformes. Dans la section suivante, nous présentons l'évaluation des performances de classification à l'aide de caractéristiques EEG dérivées d'un nombre limité de canaux. De ce fait, nous avons exploré l'utilisation des nouveaux traits caractéristiques proposés dans une configuration à densité basse composée de seulement 7 canaux, similaire au système évalué dans le Chapitre 5. Nous avons évalué deux positionnements à 7 canaux, le premier positionnement (Figure 6.11a) correspond à celui utilisé dans les expériences rapportées au Chapitre 5, le deuxième positionnement (Figure 6.11b) était motivé par les cartes topographiques AUC présentées dans les Figures 6.5, 6.6 et 6.7 où de meilleures valeurs d'AUC étaient présentes dans les électrodes sur les lobes occipitaux, pariétaux et temporaux. Les performances de classification obtenues pour les tâches testées pour chaque combinaison des ensembles de traits caractéristiques et d'approche d'amélioration du signal EEG sont présentées dans les Tableaux 6.7 à 6.10 pour le positionnement présenté à la Figure 6.11a; et dans les Tableaux 6.11 à 6.14 pour le positionnement présenté à la Figure 6.11b.

0.6.4 Discussion

Étant donné que les traits caractéristiques de l'ensemble de caractéristiques RG3 ont été obtenus de manière heuristique à partir de la comparaison entre les groupes Nold et MA, ils présentent des performances exceptionnelles (exactitude de 88 %) dans la tâche de classification Nold vs MA, Tableau 6.3. De plus, l'utilisation des traits caractéristiques RG3, seuls ou combinés à des traits caractéristiques spectraux, a permis d'améliorer l'exactitude de la plupart des tâches de classification. De ce fait, ces traits caractéristiques semblent être informatifs pour l'évaluation de la progression de la MA, mais en raison de la façon dont ils ont été conçus, ils peuvent ne pas être optimaux pour une telle évaluation. Afin d'améliorer la définition de tels traits caractéristiques, des méthodes de traitement d'images peuvent être utilisés pour extraire d'autres traits caractéristiques du spectrogramme de modulation qui pourraient être plus utiles pour l'identification de différents stades de la MA.

Les traits caractéristiques proposés ont été évalués dans deux configurations à 7 canaux, illustrés à la Figure 6.11. Le premier positionnement, présenté dans la Figure 6.11a, a été proposé pour comparer les performances des nouveaux traits caractéristiques proposés avec les résultats présentés au Chapitre 5. Avec ce positionnement, on peut remarquer dans le Tableau 6.7 que l'utilisation des traits caractéristiques RG3 améliore la classification de base obtenue avec les traits caractéristiques PSD. De plus, pour les signaux améliorés par wICA, l'amélioration était d'environ 70% (comme indiqué dans les Tableaux 5.3 et 6.7) à près de 80%. Le deuxième positionnement à densité basse (présenté dans les Figures 6.11b) présentait une performance de classification conforme à celle obtenue avec le positionnement à 20 canaux pour l'utilisation des traits caractéristiques RG3 et des données sélectionnées manuellement, parce que les électrodes pour cette configuration ont été sélectionnées en fonction de leur pouvoir discriminant, affichées sous forme de valeurs AUC dans la Figure 6.5. Semblable aux résultats présentés dans le Chapitre 5, la réduction des canaux à travers les tâches de classification explorées entraîne une baisse des performances de classification.

Enfin, à partir des cartes topographiques AUC obtenues pour les enregistrements EEG bruts et améliorés par WICA, présentées respectivement dans les Figures 6.6 et 6.7, il est possible d'apprécier que les deux enregistrements conduisent à des valeurs AUC similaires. De ce fait, pour toutes les performances de classification obtenues (Tableaux 6.3 à 6.14) pour les traits caractéristiques dérivés du domaine de la modulation fonctionnent aussi bien avec les enregistrements EEG bruts qu'avec les améliorations wICA, cela peut être dû à la robustesse du bruit dans les traits caractéristiques proposés, une exploration plus poussée est nécessaire pour déterminer cette hypothèse.

0.7 Conclusion

Dans cette thèse de doctorat, nous avons étudié les défis actuels liés à l'utilisation de la rsEEG pour l'étude de la MA: (*i*) la sensibilité des signaux EEG aux artefacts et (*ii*) l'exigence actuelle d'un grand nombre d'électrodes. Pour répondre à ces défis, nous avons étudié: (*i*) l'utilisation de techniques automatisées de manipulation des artefacts et leurs effets sur le diagnostic de la MA basé sur la rsEEG, (*ii*) la viabilité des dispositifs EEG à densité basse dans le diagnostic de la MA et sa performance, et (*iii*) les traits caractéristiques EEG basés sur l'analyse de la modulation, leur conception et leur performance dans le diagnostic de la MA. Le résultat de ces investigations est inestimable pour le développement d'un systeme automatisé, portable et abordable pour le diagnostic et la surveillance de la progression de la MA basé sur l'EEG.

Manipulation automatique des artefacts. La principale difficulté de travailler avec des signaux EEG est leur grande sensibilité aux artefacts. Par conséquent, la plupart des chercheurs ont eu recours à des signaux EEG «sans artefacts», sélectionnés manuellement par une inspection visuelle experte. Malheureusement, cette approche pose de sérieux problèmes qui rendent son utilisation insoutenable dans une clinique pratique. En conséquence, l'automatisation complète du processus de manipulation des artefacts constitue une étape cruciale dans le développement de toute application EEG. Nous avons étudié les effets des méthodes de MAA sur les systèmes de diagnostic de la MA basés sur quatre types de traits caractéristiques EEG. Les résultats expérimentaux ont montré que la performance du diagnostic était améliorée avec l'utilisation des méthodes de MAA (par rapport aux données non traitées). À partir des systèmes de diagnostic de la MA entièrement automatisés évalués, l'utilisation de l'algorithme wICA et de l'ensemble de traits caractéristiques contenant tous les traits caractéristiques extraits présentaient les meilleures performances de classification. De plus, la performance obtenue était conforme à celle obtenue avec l'EEG sélectionné manuellement. Bien que les méthodes de MAA soient fiables pour supprimer certains artefacts EEG courants, elles faussent également les informations EEG, en particulier celles liées à la phase, ce qui entrave les performances des traits caractéristiques et techniques utilisant ces informations. Finalement, nous espérons que l'utilisation de tels outils de diagnostic entièrement automatisés peut aider les cliniciens non seulement à détecter la MA, mais aussi à établir un diagnostic précoce et à surveiller la progression de la maladie.

Dispositifs EEG portables. Les dispositifs EEG de type médical et de recherche ont tendance à être encombrants et à contenir autant d'électrodes que possible, car les méthodes d'analyse de connectivité et de localisation de sources sont plus performantes avec cette configuration. Cependant, l'utilisation de ces dispositifs EEG dans l'évaluation de la MA n'est pas pratique car ils peuvent provoquer un stress sur les participants et impliquer de longs temps d'installation, qui à leur tour prolongent les sessions d'expérience. La littérature sur l'utilisation de dispositifs EEG portables de densité basse est limitée et ne compare pas les performances de classification obtenues avec les performances des installations plus denses. De ce fait, nous avons exploré l'utilisation de dispositifs EEG portables à densité basse (7 canaux) et étudié les effets de la réduction du nombre d'électrodes sur les performances de classification de la MA. En outre, nous avons discuté de la différence entre les conditions de rsEEG en éveil, c.-à-d. les protocoles yeux ouverts et yeux fermés. Les résultats de nos expériences suggèrent qu'il y a une baisse significative des performances de classification en raison de l'utilisation de moins de canaux, et que les protocoles à yeux ouverts et à yeux fermés reposent sur des traits caractéristiques pertinents similaires pour les diagnostics.

Nouveaux traits caractéristiques de modulation. Dans la recherche de la MA, les signaux EEG ont été largement étudiés en utilisant les bandes de fréquences spectrales classiques, définies à l'origine pour les sujets sains. Cependant, cette approche pourrait ne pas être optimale, car la dynamique de l'EEG pendant la présence de la MA pourrait ne pas être bien caractérisée avec ces bandes classiques. Dans cette thèse de doctorat, nous avons exploré les signaux EEG dans le domaine de la modulation, où ils ne sont pas limités aux bandes classiques. Nous avons proposé un ensemble de nouveaux traits caractéristiques basés sur cette représentation de la modulation et montré qu'ils conduisaient à des améliorations des performances de la classification de la MA. Ces traits caractéristiques proposés, lorsqu'ils sont extraits de l'EEG brut, ont abouti à des performances similaires à ceux extraits de l'EEG amélioré par wICA. Cette constatation montre leur robustesse contre les artefacts. Ceci est une découverte intéressante, car elle suggère que les méthodes de MAA peuvent éventuellement être complètement ignorées, rendant ainsi les systèmes de diagnostic encore plus simples et rapides.

Chapter 1

Introduction

1.1 Dementia and Alzheimer's disease

The term dementia is used to encompass a number of neurodegenerative disorders that have their origin in damage and death of neurons. The progression of dementia leads to a decline, and consequently, to loss of both cognitive (e.g., memory, reasoning, communication) and behavioural functions that interfere with an individual's daily life. Among the disorders classified as dementia, Alzheimer's disease (AD) is the most common form, accounting for nearly 70% of dementia cases around the world. AD is ultimately fatal, and to date, there is no cure, only palliative treatments that temporarily slow symptom progression, thus aiming at improving the quality of life of patients, their family and caregivers [2, 3, 4].

In 2015, 46.8 million people were living with dementia worldwide and this number is projected to grow to 74.7 million by 2030, and to 131.5 million by 2050 [3], with similar trend projections for Canada [5]. Moreover, given the demographic differences around the globe, much of these dementia cases (approximately 65%) will take place in low- and middle-income countries, as shown in Figure 1.1. The trends in different regions are driven by their respective population growth and demographic ageing [3]. Dementia represents a significant social and economic impact; in 2015, the estimated worldwide costs related to dementia were approximately US$ 818 billion, and this financial burden is expected to increase to US$ 2 trillion by 2030 [3]. Due to the serious implications of current and future global prevalence and incidence of dementia, associated mortality and global economic cost, the World Health Organization made an urgent call to include dementia as a priority in health agendas around the globe in order to raise awareness, improve early diagnosis and provide better care and support for patients, their families and caregivers [2, 4]. Currently, there are no treatments to cure or alter the progression of AD. However, early diagnosis and management of AD can improve the quality of life of people living with AD, as well as their caregivers [4]. Accurate diagnosis of AD is challenging, as its pathophysiological processes may start up to 20 years before clinical symptoms can be detectable. Moreover, AD symptoms are commonly confused with normal aging processes, thus frequently delaying diagnosis [92, 93]. In addition, as novel disease-modifying drugs are being studied and developed, it is likely that their efficacy would be higher if administered during early stages of the disease [94, 4], thus making early diagnosis a pivotal element in AD research and therapy.

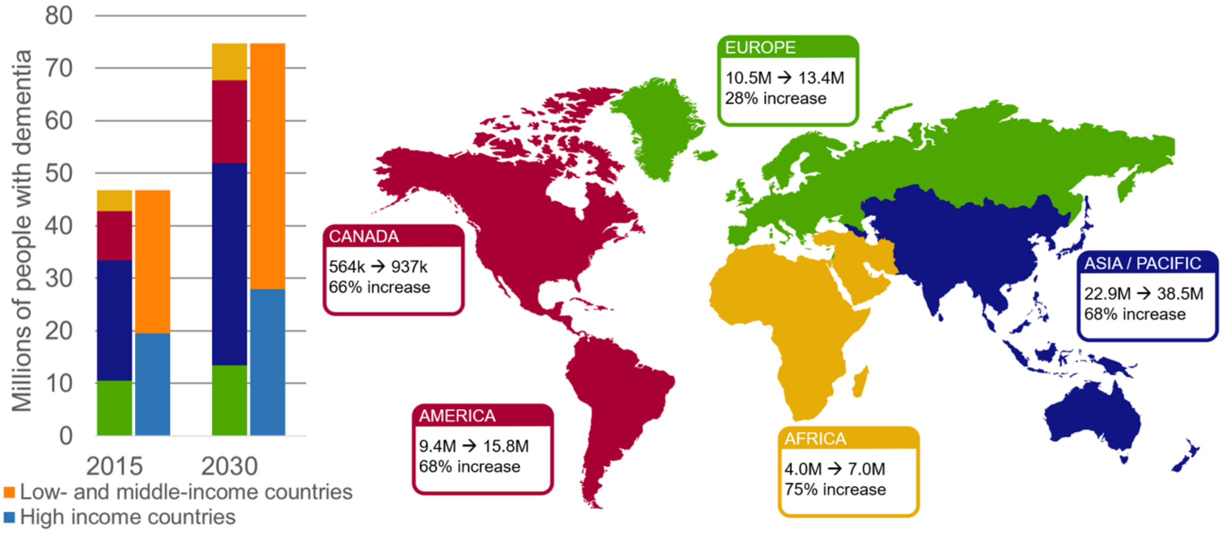

Figure 1.1 – Global prevalence of dementia in 2015 and projected increase by 2030.

According to its symptoms, AD can be classified into three stages: preclinical, mild cognitive impairment, and dementia due to AD [6].

1. *Preclinical AD.* Changes in the brain, blood and cerebrospinal fluid related to AD start to occur, but the patient does not show any symptoms. This phase may start years (or even decades) before the first clinical symptoms of dementia appear [7, 95]. The possibility of detecting AD in this preclinical stage would offer a pivotal opportunity for therapeutic interventions [96].

2. *Mild cognitive impairment (MCI).* In this early stage, the person still functions independently but may feel some memory lapses, difficulties coming up with the right word or remembering the location of familial places. Friends and family may notice these small difficulties. This stage is often referred as mild or early-stage AD disease. The term MCI has been frequently used in research trials with the objective of including as many individuals as possible with symptoms that were not severe enough to meet current AD diagnostic criteria but might at some point in time. However, it has been observed that 30% of subjects diagnosed as MCI will not progress to AD dementia in a near future [92, 9, 97].

3. *Dementia due to AD.* The patient's ability to function in daily life is seen affected by impairments in memory, thinking and behavior [8]. This stage is frequently subdivided into:
    (a) *Moderate or middle-stage AD.* In this phase, usually the longest one, the person may experience greater difficulty to execute daily tasks such as paying bills, recalling one's own address, getting dressed or controlling bladder and bowels. The patient notices these symptoms, which leads to frustration and anger. Also, in this stage some psychological symptoms start to appear, e.g., suspiciousness, delusions or compulsive behavior.

    (b) *Severe or late-stage AD.* In this final stage, individuals start losing their ability to interact with the environment and their memory and cognitive skills are severely affected. In this phase, the individual needs 24-hour personal care.

The pathophysiological process of AD is thought to start up to 20 years before clinical symptoms can be detectable [7, 96]. Over the last two decades, evidence has shown that the correspondence between pathology and clinical symptoms is not always consistent [6] and the two are best conceptualized as separated continua, which may evolve in parallel but with a temporal offset [7]. As such, AD is regarded today as a continuum rather than discrete stages [95, 98].

1.1.1 Current Alzheimer's disease diagnosis

Today, definite AD diagnosis is only possible post-mortem when analysis reveals the structural brain damage characteristic of the disease. The current clinical diagnostic criteria for AD were developed by the National Institute on Aging and the Alzheimer's Association (NIA-AA) [6, 7, 8, 9]. These criteria are an update of the previous widely used guidelines established in 1984 by the

National Institute of Neurological and Communicative Disorders and Stroke and the Alzheimer's Disease and Related Disorders Association (NINCDS-ADRDA) [72]. Besides the use of medical records and neurological examinations such as the mini-mental state examination (MMSE) [10] and the Clinical Dementia Rating (CDR) [11], the updated guidelines include the use of biomarkers derived from cerebrospinal fluid (CSF) and neuroimaging techniques to support diagnosis of AD in symptomatic individuals [6]. Obtaining a CSF sample requires a lumbar puncture, making the measurement of these biomarkers an invasive and impractical approach, hindering its use in daily clinical practice. As an alternative, blood biomarkers such as plasma T-tau are also being researched, as they can provide similar information as CSF but are a less invasive and less costly alternative [99]. In general, biomarkers for the study of AD are divided in three main categories: A, T and N, where the first two categories, A and T, include biomarkers that are related to the brain amyloidosis and tauopathy processes respectively; and the category N encompasses biomarkers that measure neurodegeneration or neural injury (e.g., CFS T-tau, FDG PET, atrophy in MRI) [98]. Typically, accuracies up to 90% have been reported with current diagnosis methods.

Neuroimaging tools, in turn, such as magnetic resonance imaging (MRI), computed tomography (CT) and positron emission tomography (PET) allow clinicians to investigate the brain damage extension due to AD *in vivo*. Alas, once the disease-related structural damage is detectable by the current spatial resolution of these neuroimaging techniques, AD is already well advanced, i.e., the atrophy in the brain may be already extended [92]. Moreover, these neuroimaging tools are expensive, time-consuming and require intervention by experts, thus limiting their widespread use for AD diagnosis in medium- and low-income countries. Such limitations are also present in remote and rural regions of developed countries (e.g., Canada's North), thus leading to displacements that are neither comfortable nor practical for the patient. In fact, this situation is not limited to rural regions, as even metropolitan areas in Canada can have wait times for a non-emergency MRI as high as six months [100]. Driven by the drawbacks and limitations of CFS and neuroimaging biomarkers, electroencephalography (EEG)-based biomarkers have emerged as a promising tool in the study of AD.

1.2 Electroencephalography

Over the last two decades, EEG has been proven to be a reliable clinical tool for the study of illnesses and cortical disorders [1], such as Huntington disease [101], autism spectrum disorders [102], epilepsy diagnosis and seizure detection [59], cerebral ischemia [103], as well for the development of brain-computer interfaces (BCIs) [104].

EEG consists of recording changes in the electrical potential measured at the individual's scalp with electrodes. These changes have their origin in the electrical activity evoked by synchronous activation of thousands of neurons with similar spatial orientation, referred as *dipoles*, in the cerebral cortex, as depicted in Figure 1.2 [12, 1].

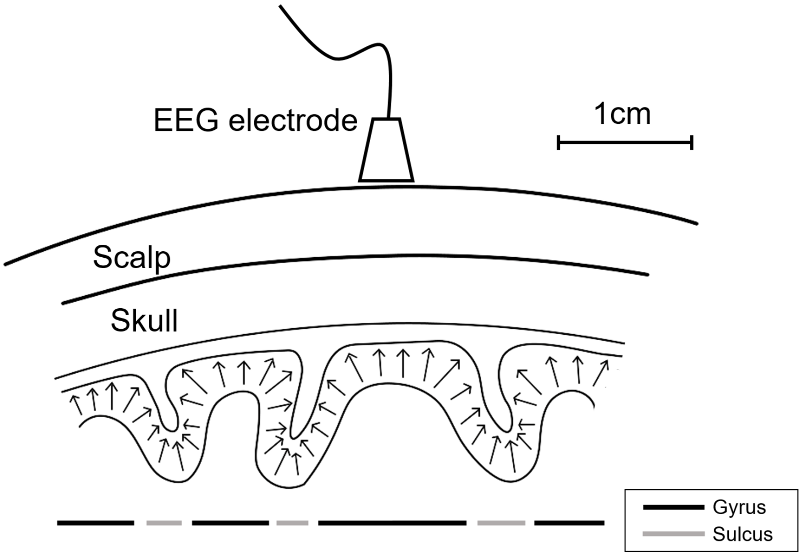

Figure 1.2 – Neuronal origin of the EEG signal. The electrode is more sensitive to electrical activity from zones where the neurons share a similar orientation (gyri), than from zones where neurons have opposing orientation (sulci). Modified from [1].

The electric potentials are measured between electrodes placed on various points on the scalp and a reference electrode that is located electrically "far" from the cortical sources of interest. Common locations for the reference electrode include average mastoids, average earlobes and neck [1, 13]. To avoid variations between subjects with different head sizes and shapes, standard placements or electrode layouts have been proposed, among these the international 10-20 system is the most utilized layout, where the electrodes are placed in a grid that arises from dividing the front-to-back lines (from naison to inion) and the left-to-right lines (from left to right preauricular points) in segments of 20% and 10% of the total distance, covering the whole scalp. Figure 1.3a depicts the 10-20 system layout, it is important to emphasize that higher density variants such as 10-10 and 10-5 systems are utilized as well [105]. The measured electric potentials on the scalp, as shown in Figure 1.3b, present amplitudes < 100 μV and are commonly digitized with sampling frequencies higher than 200 Hz. As such, EEG presents better temporal resolution than other neuroimaging techniques [14].

For analysis, EEG signals are traditionally divided into five major frequency bands, namely: delta (δ) 0.1-4 Hz, theta (θ) 4-8 Hz, alpha (α) 8-12 Hz, beta (β) 12-30 Hz and gamma (γ) > 30 Hz. These frequency bands have been defined based on visual inspection of EEG signals in healthy subjects, and its definition has helped to standardize experimental protocols and has provided useful insights about brain functionality and synchronization [1, 13, 15]. In research, these bands are often divided in subbands, such as low-alpha, high-alpha, low-beta, etc. to perform more specific analyses. Figure 1.3c shows the EEG signal from one electrode decomposed into its major component bands. Additionally, the spectral representation of these bands is depicted by Figure 1.3d. Unlike other biopotentials, such as the electrocardiography (ECG) signal, EEG signals are rarely analyzed visually, thus further signal processing is required to identify patterns and extract valuable information from EEG recordings [15, 13].

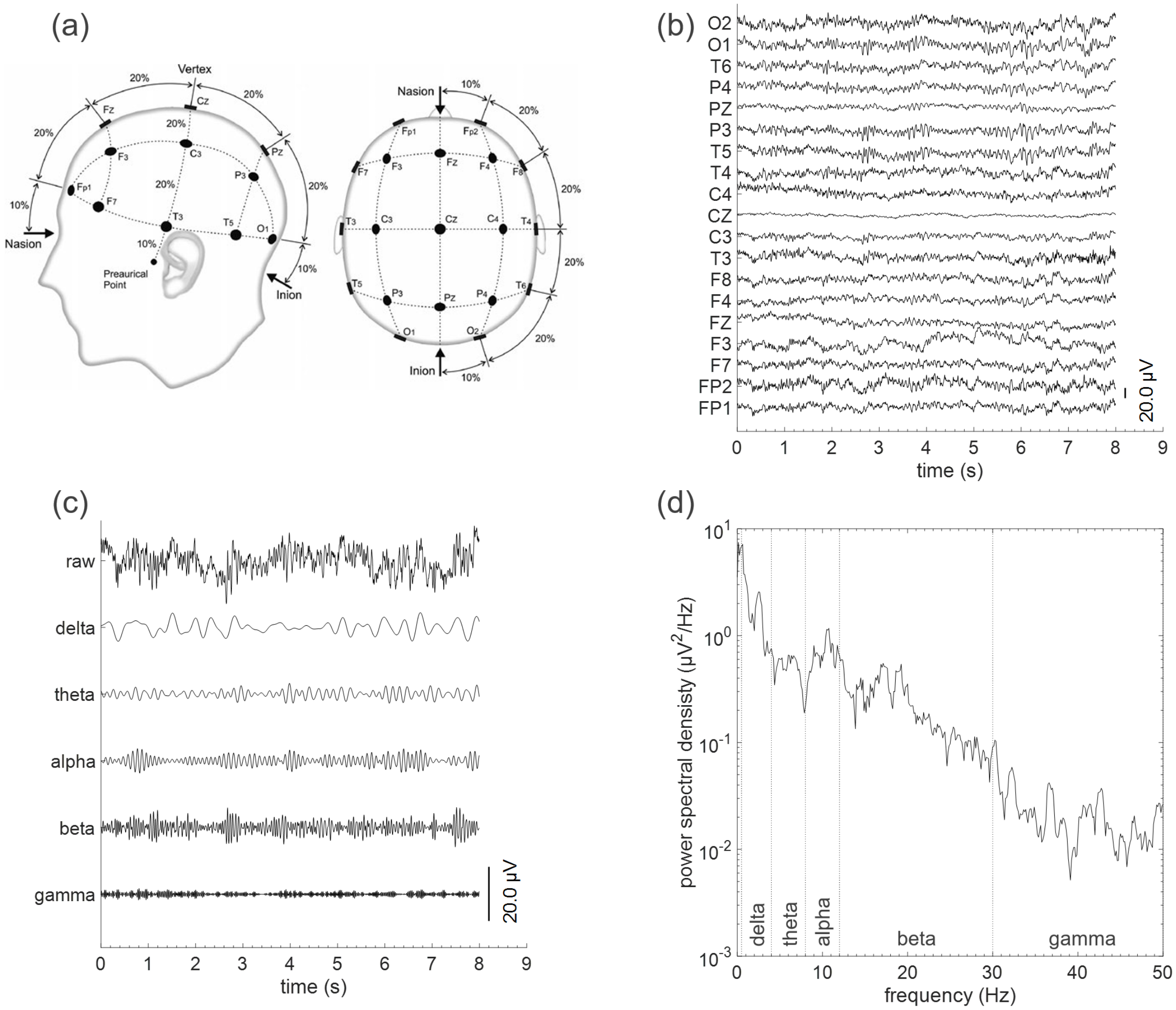

Figure 1.3 – EEG signals. (a) EEG electrode placement in the international 10-20 system layout. (b) EEG signals in the time domain from different electrodes. (c) Decomposition of a one-electrode EEG signal, electrode C3, into frequency bands. (d) Spectral representation of EEG bands for the EEG signal at electrode C3.

1.3 Electroencephalography in Alzheimer's disease study

Since EEG signals have their origin in the underlying activity in the cerebral cortex, EEG-based biomarkers can be used to infer neuronal degeneration and decay in the number of synapses caused by AD progression (biomarkers in category N according to [98]); thus EEG has attracted the interest of researchers for the study and diagnosis of AD. Furthermore, EEG signals have been studied in healthy elderly individuals, showing that there are no substantial changes in EEG associated with healthy aging, thus making EEG a suitable technique for the assessment of functional impairments caused by AD and its progression [16]. Indeed, EEG biomarkers have the potential of serving as support and/or alternative to existing biomarkers (e.g., CSF and neuroimaging), with the advantage of being non-invasive, less expensive and potentially portable.

Over the last few decades, many studies have investigated the effects of AD and its progression on EEG signals. These studies have made use of EEG signals collected under a number of different conditions, typically falling under two classes: resting-state and event-related recordings.

> **Resting-state EEG (rsEEG):** also known as spontaneous or background EEG, is the activity recorded during the absence of any kind of stimulus, thus measuring the endogenous brain activity [18, 15]. As the participant is not required to perform any specific task, EEG acquisition becomes simpler, more comfortable, and less stressing for the participant [38, 106]. The rsEEG recordings comprehend resting-awake state (with either open- or closed-eyes) and sleep recordings.
>
> **Event-related EEG recordings:** consist of EEG signals that are recorded with temporal relationship to the occurrence of a specific event, i.e., EEG signals are time-locked. These events can be related to sensorial perceptive, motor or cognitive processes [1, 15, 107]. Besides being time-locked, when the event-related EEG activity is also phase-locked, these recordings receive the name of event-related potentials (ERPs) [13, 15]. When the event-related EEG activity is not phase-locked, it is often referred to as induced activity [108, 109] and can be analyzed as either event-related (de)synchronization (ERD/ERS) [13, 110] or event-related oscillations (ERO) [107].

Recent results show that biomarkers derived from rsEEG and event-related EEG recordings can be useful for AD diagnosis, obtaining accuracy levels around 70-90%, thus is in line with those achieved with other types of biomarkers [38, 17, 92, 111]. In the literature, recent reviews have been published covering the use of event-related EEG for AD diagnosis [107, 112, 111]. Event-related EEG recordings offer the opportunity to examine the effect of AD on specific brain pathways [24, 113], and in the case of ERPs, recordings can rely on EEG devices with few electrodes due to characteristic scalp distribution of the ERPs [56]. However, event-related EEG recordings require devices for the stimulation and a specific setup between the stimulation device and the EEG equipment. In contrast, rsEEG recordings do not require additional devices, nor the performance of specific tasks by the user, thus are simpler and more comfortable for elderly individuals and AD patients [38, 87, 114]. As a result, most of the published works exploring the utility of EEG signals for AD diagnosis have relied on the analysis of rsEEG. An expanded review on the use of rsEEG for AD diagnosis is provided in Chapter 2.

Notwithstanding, while the use of EEG presents numerous advantages compared with other neuroimaging techniques, a number of challenges also exist and need to be addressed before EEG biomarkers become widely used in clinical practice. The two main limitations hindering the utilization of EEG for AD study, diagnosis and assessment are: (*i*) high sensibility of the EEG to other interfering signals, either of physiological or environmental nature, and (*ii*) the requirement of high-density EEG devices.

1.4 Challenges for EEG-based Alzheimer's disease diagnosis

The major shortcoming in research based on EEG is that the signals are subject to interference from other signals, which can be originated by the participant or by external sources. Collectively, these interfering signals are called artifacts. Some common sources of artifacts include eye movements, blinks, cardiac activity, cranial muscle activity, electrode movement and power grid interference [1, 15, 19, 20]. These artifacts have detrimental effects on EEG signal quality and consequently on AD diagnosis accuracy. As a result, the majority of the published studies have relied on "artifact-free" EEG segments or epochs, which are manually selected through meticulous visual inspection performed by expert clinicians. However, the manual selection of artifact-free epochs is a tedious, time-consuming, and expensive process that introduces human biases and discards a great amount of recorded EEG data [20]. To overcome this issue, artifact handling methods may be employed to increase signal quality or to reduce the reliance on human visual inspection. Alternatively, new artifact-robust features may be developed for improved AD analysis.

Moreover, research- and medical-grade EEG devices typically used for rsEEG-based AD studies have 16 or more electrodes (often 64+), thus making them hard to transport and expensive to fund, especially for low- and middle-income countries. Technological advances, however, over the last few years, have resulted in portable, affordable and wireless commercial EEG devices capable of recording and analyzing EEG signals with laptops, tablets or smartphones [21, 22]. Such advances open doors for portable, low-cost EEG-based AD diagnosis systems that can make an impact in developing countries as well as in geographically-remote regions. As such, the feasibility of such systems should be explored.

1.5 Thesis contributions

The overarching goal of this doctoral research is to develop a portable, low-cost, and automated EEG analysis system that can be used by clinicians worldwide to improve AD diagnosis via a simple resting-state experimental protocol. To achieve this goal, several innovations had to be developed, thus constituting the main contributions of this thesis. More specifically, three main innovations have been proposed, implemented, and evaluated.

1. To remove the need for expert human intervention for the collection of artifact-free data, this thesis is the first to explore the effects of several fully automated artifact handling algorithms on rsEEG signals and gauge their advantages and disadvantages for automated AD diagnosis.
2. To explore the potential of portable low-density devices and alternate resting-awake protocols, this thesis is the first to explore changes in eyes-open versus eyes-closed experimental protocols on diagnostic accuracy, as well as gauge the performance changes by going from an automated 20-channel system to a portable, 7-channel one.
3. Relying on conventional EEG features for diagnostic can be problematic, as discriminatory information can be removed by the artifact handling algorithms or by the reduced number of available channels. Here, a new class of features derived from a spectrotemporal signal representation is presented and shown to (*i*) provide improved robustness against artifacts, (*ii*) potentially bypass the need for a separate artifact removal step, and (*iii*) provide better discriminatory information not only for AD diagnostic purposes, but also for disease progression monitoring.

These three innovations have been described in several manuscripts, as listed below in chronological order. Where appropriate, the chapters of this thesis in which these publications appear are also specified. A list of publications that resulted from tools developed herein but applied in allied domains is also given below for the sake of completeness.

1.6 Publications derived from the thesis

Publications included in the thesis

Articles published in refereed journals

- “The effects of automated artifact removal algorithms on electroencephalography-based Alzheimer’s disease diagnosis”, **Cassani, R.**, Falk, T. H., Fraga, F. J., Kanda, P. A. M., and Anghinah, R., *Frontiers in Aging Neuroscience*, vol. 6, p. 55, 2014. [115] [Chapter 4]

- “Towards automated electroencephalography-based Alzheimer’s disease diagnosis using portable low-density devices”, **Cassani, R.**, Falk, T. H., Fraga, F. J., Cecchi, M., Moore, D. K., and Anghinah, R., *Biomedical Signal Processing and Control*, vol. 33, pp. 261–271, Mar 2017. [116] [Chapter 5]

- “Systematic review on resting-state EEG for Alzheimer’s disease diagnosis and progression assessment”, **Cassani, R.**, Estarellas, M., San-Martin, R., Fraga, F. J., and Falk, T. H., *Disease Markers, in press, 2018.* [23] [Chapter 2]

Under review

- “New artifact-robust EEG modulation features for improved Alzheimer’s disease diagnosis and progression monitoring”, **Cassani, R.** and Falk, T, in preparation, to be submitted to the *IEEE Transactions on Neural Systems and Rehabilitation Engineering* [117] [Chapter 6]

Conference proceedings and abstracts

- “Towards automated EEG-Based Alzheimer’s disease diagnosis using relevance vector machines”, **Cassani, R.**, Falk, T. H., Fraga, F. J., Kanda, P. A., and Anghinah, R., *in Proc. 5th ISSNIP-IEEE Biosignals and Biorobotics Conference: Biosignals and Robotics for Better and Safer Living*, pp. 1-6, May 2014. [90] [Chapter 4]

- “MuLES: An open source EEG acquisition and streaming server for quick and simple prototyping and recording”, **Cassani, R.**, Banville, H., and Falk, T. H., *in Proceedings of the*

20th International Conference on Intelligent User Interfaces Companion, pp 9-12, 2015. [118] [Appendix B]

- "Automated Alzheimer's disease diagnosis using a portable 7-channel electroencephalography device", **Cassani, R.**, and Falk, T. H., *Abstract in IUPESM World Congress, Toronto 2015*, 2015. [119][Chapter 5]

Book chapters

- "Spectrotemporal modeling of biomedical signals: theoretical foundation and applications", **Cassani, R.**, and Falk, T. H., *in Reference Module in Biomedical Sciences*, Elsevier, 2018. [120] [Chapter 3 and Appendix A]

Other publications

Conference proceedings and abstracts

- "EEG-theta modulation is greater in spatial learners than response learners: A scalp-EEG study in young adults tested on a virtual navigation task", Falk, T. H., Banville, H., Bishundayal, S., **Cassani, R.**, Clerico, A., Dahmani, L., Gupta, R., Ratnarajah, A., Phillips, N., and Bohbot, V. D., Abstract and Poster *in Annual Society for Neuroscience Meeting*, 2014. [121]
- "Gaze and BCIs as Gaming Inputs: Opportunities and Open Challenges", **Cassani, R.**, and Falk, T. H., in *EyePlay Workshop, CHI-PLAY2014,*, 2014 [122]
- "Assessment of EEG-based biomarkers of Alzheimer's disease progression", Estarellas, M., **Cassani, R.**, and Falk, T. H., *In Mechanisms, Clinical Strategies, and Promising Treatments of Neurodegenerative Diseases. 13th International Conference AD/PD Vienna, Austria, March 29 to April 2, 2017: Abstracts, Neurodegenerative Diseases*, vol 17 (suppl. 1), pp. 1014, 2017. [123]
- "Respiration rate estimation from noisy electrocardiograms based on modulation spectral analysis", **Cassani, R.**, Narayanan, S., and Falk, T. H., in *the Canadian Medical and Biological Engineering Society (CMBES) Proceedings (Vol. 41)*, 2018. [124]

- "A neurophysiological sensor-equipped head-mounted display for instrumental QoE assessment of immersive multimedia", **Cassani, R.**, Moinnereau, M-A., and Falk, T. H., in the *Tenth International Conference on Quality of Multimedia Experience (QoMEX)*, 2018. [125]
- "Resting-awake EEG amplitude modulation can predict performance of an fNIRS-based neurofeedback task", Trambaiolli, L. R., **Cassani, R.**, Biazoli Jr, C. E., Cravo, A. M., Sato, J. R., and Falk, T. H., in the *2018 IEEE International Conference on Systems, Man, and Cybernetics (SMC)*, 2018. [126]

1.7 Thesis organization

While this introductory chapter has presented the challenges with EEG-based AD diagnosis and laid out the foundation for the contributions described herein, the remainder of this dissertation is structured as follows: Chapter 2 provides an overview of the state-of-the-art in rsEEG for AD assessment and places special focus on the pipeline typically used for AD diagnosis, including pre-processing, epoching, EEG feature extraction, feature selection, and classification. Chapter 3 expands the concept of amplitude modulation analysis of biological signals, its theoretical framework and its potential application on rsEEG signals; this chapter serves as a basis for the new features proposed later in the document. In Chapter 4, in turn, the detrimental effects of EEG artifacts on AD diagnosis are studied and the advantages and disadvantages of automated artifact handling algorithms on AD diagnosis performance are explored. Next, Chapter 5 presents the results obtained when portable low-density EEG devices are used. Eyes-open and eyes-closed experimental protocols are also compared and their effects on AD diagnosis accuracy are quantified. In Chapter 6, we describe the development of new artifact-robust features based on the analysis of the amplitude modulation of rsEEG signals. We validate the usefulness of the proposed features not only via source localization methods, but also via improved classification accuracy for four diagnostic sub-tasks (healthy versus AD, healthy versus mild AD, mild versus moderate AD, and healthy versus mild versus moderate AD). Lastly, Chapter 7 provides the general conclusions of this thesis, as well as future research areas.

Chapter 2

State-of-the-Art in rsEEG-based AD Diagnosis

2.1 Preamble

This chapter is compiled from material extracted from the manuscript published in the journal *Disease Markers* [23].

2.2 Introduction

In the EEG-based study of AD, the use of rsEEG recordings presents various advantages compared with event-related EEG recordings; among those advantages we can cite:

- **Simplicity.** As the participant is not required to perform any specific task, the EEG acquisition session becomes more comfortable and less stressing for the participant [38, 106]. This is critical, as even from early AD stages, participants are often unable to follow the task instructions or complete with the totality of the given tasks [80].
- **Reduced artifacts.** Often during rsEEG recordings, the participant is awake and comfortably sitting with her eyes closed, thus head-movement and eye-related artifacts are drastically reduced. Unfortunately, EEG artifacts cannot be completely avoided, and their presence may

have a detrimental effect in the study of AD through EEG signals; this topic is further developed in Chapter 4.

- **Potential portability.** Being time-locked, event-related EEG recordings require a specific setup and additional equipment to synchronize EEG data with the event (either stimulus or task). This obstructs the portability provided by the miniaturization of EEG devices. This topic is addressed in Chapter 5.
- **Habituation effects.** In contrast with ERPs, rsEEG recordings do not suffer from habituation effects over time [106].

Such advantages make rsEEG a more suitable recording condition for the research on healthy normal elderly controls (Nold) and AD participants; as consequence, most of the published works on the study of AD based on EEG signals have relied on the analysis of awake rsEEG data. In early 2018, we performed a comprehensive review on the use of rsEEG for the study of AD, a total of 112 journal articles published between January 2010 and February 2018 were gathered and meticulously reviewed with the goal of comparing the crucial elements in a rsEEG-based AD diagnosis system, elements such as: experimental protocol, EEG signal acquisition, pre-processing, artifact handling, feature extraction and classification. Moreover, the systematic review pointed out common practices, differences and consensus in the utilization of rsEEG, reported limitations, and recommendations for future studies [23].

In this chapter, firstly an overview of the typically reported effects of AD on the rsEEG signal is provided, followed by the general structure of a rsEEG-based system for AD diagnosis and its comprising elements, then each of those elements is further discussed with regard to the outcomes from the above mentioned literature review.

2.3 Effects of AD on rsEEG

With adoption of quantitative analysis of EEG data, in the last two decades several works have explored the rsEEG abnormalities related to AD; an extensive review of these abnormalities can be found in [17, 24]. Four major effects of AD and its progression on the rsEEG signals have been repeatedly reported.

1. **Slowing.** The power spectrum of the rsEEG signals shift from high frequency components (alpha, beta and gamma) towards low frequency components (delta and theta). This slowing process has been commonly observed in MCI and AD patients [24, 17, 127]. The degree of the power shift has been shown to be proportional to the progression of AD [25, 26]. The slowing of EEG is thought to be the consequence of loss of cholinergic innervations in AD patients [27].

2. **Decrease in synchronization.** Perceived as a reduction in connectivity between cortical regions, a decrease in synchronization has been reported in AD patients. The origin of this phenomenon is not well understood yet, although it is thought to be related to the atrophy in the communication of neural networks [28, 29, 30, 31]. It is interesting to mention that some studies have shown an increase of synchrony in patients with MCI and AD during memory tasks, which is thought to be caused by compensatory mechanisms in the brain [128].

3. **Reduced complexity.** A decrease in the global complexity of the brain electrical activity has been observed in AD patients compared with healthy controls [32, 17, 33]. This decrease is likely caused by massive neuronal death and reduction in non-linear connections between cortical regions, leading to simpler (less complex) EEG dynamics.

4. **Neuromodulatory deficit.** Recent experimental evidence [34, 35] has suggested a neuromodulatory deficit in AD, which may have its origin in the reduction in neurotransmitters due to damage in their brain pathways during AD [17, 27]. As such, modulation analysis has recently been proposed to quantify the non-stationary behaviour in rsEEG [36].

Effects of AD on rsEEG, such as slowing and decrease in synchronization, have been observed in other encephalopathies [129, 130]. Thus, to improve the specificity in rsEEG-based AD diagnosis, it is needed to combine the non-specific rsEEG biomarkers with additional information derived from routine tests and the medical history of the individual. Despite the fact that the effects of AD on rsEEG signals are often regarded independently, it is important to remark that they have their origin in the same phenomenon, that is to say, the loss of neurons in AD that disrupts anatomical brain connectivity at the level of functional networks [37, 33, 17]. Diverse methodologies have been proposed to study and quantify the effects with the final aim of being able to diagnose AD from rsEEG signals. Though the proposed methodologies are different in many aspects, all of them can be considered to have a similar structure, which is presented in the following section.

2.4 A rsEEG-based AD diagnosis system

In general, a system for the diagnosis of AD based on rsEEG signals can be viewed as the structure depicted in Figure 2.1. First, the EEG signals are acquired under a specific experimental protocol that describes the participant status, EEG device and duration of the recording. Second, in the pre-processing stage, recorded EEG signals are bandpass filtered with the objective of removing artifacts. Also, in this stage other methods to reject and/or remove artifacts are implemented. Afterward, during feature extraction the pre-processed EEG signals are split into epochs, for each epoch features are computed to quantify one or more of the effects of AD in the EEG signals. Finally, in the feature translation stage the computed features are used to infer the presence or progression of AD. In the following sections, we present and discuss the different elements that comprise such a system.

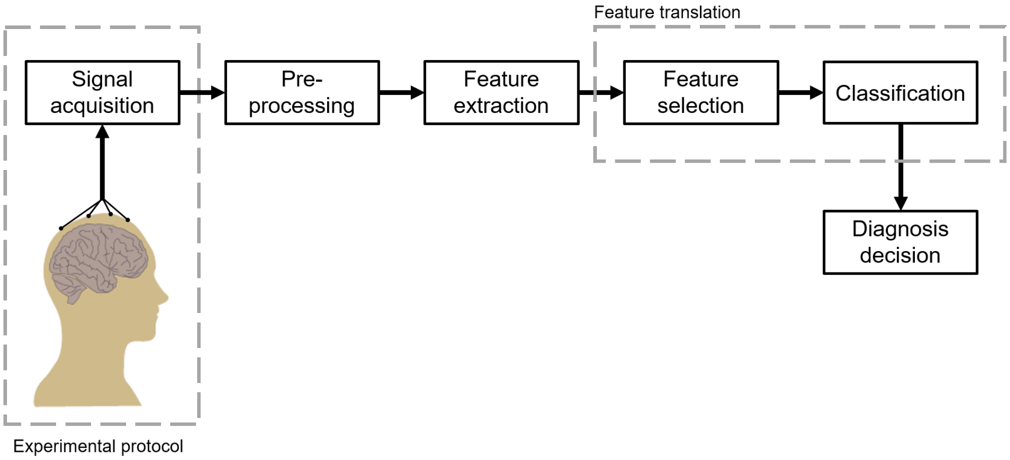

Figure 2.1 – General structure of an EEG-based AD diagnosis system.

2.5 Experimental protocol

2.5.1 Recording conditions

The most common recording condition is resting-awake eyes-closed, wherein the participant is comfortably seated with closed eyes. If drowsiness is noticed (either on the participant's behaviour or on the online trace of the EEG signals), the participant is verbally alerted, and the event is annotated. Resting-awake eyes-closed condition was explicitly reported in 109 of the reviewed articles, indeed it is regarded as a standardized procedure for rsEEG [38]. The eyes-open rsEEG recording condition is also commonly used, despite being prone to eye-movement artifacts. In general, recording conditions are not mutually exclusive, in this sense the experimental protocol can include resting-state and event-related phases; however, this has a direct impact on the total duration of the recording.

2.5.2 Recording duration

Given the target population in AD studies, recording duration becomes a critical factor for the comfort of the participant and, consequently, for the compliance of the recording. From the reviewed articles, the duration of the EEG recording session was not reported in 31 articles. From those that did report duration, values went from 2 to 33 minutes being 10 minutes the average duration. Note that these times do not include the setup time, which is proportional to the number of electrodes used for the rsEEG recording.

2.5.3 Number of channels

The decision regarding the number of electrodes is driven by the trade-off between spatial resolution and participant comfort. EEG systems with 32 or more channels are cumbersome and their electrode placement and adjustment can take 1 hour or even longer for staff with expertise in EEG [39, 40]. Moreover, a long preparation time might evoke undesired cognitive states such as drowsiness, fatigue, frustration or stress in elder participants; these induced cognitive states can alter the rsEEG signal and thus present detrimental effects for AD diagnosis. Another reason to consider for the number of electrodes is use of EEG source localization tools to estimate the approximate location of the electric activity in the brain as described in Section 2.6.4. The reported number of electrodes used for EEG signal acquisition in the reviewed studies varied greatly, from as low as 1 to as high as 256 electrodes, 19 electrodes being the most common number (in 53 articles). The impact of the number of electrodes on diagnosis performance is further explored in Chapter 5.

2.6 EEG pre-processing

In a broad sense, EEG signal pre-processing comprises the manipulations performed on the raw acquired data in order to prepare it for feature extraction [41, 13, 15]. The main goal of pre-processing is to improve the EEG signal quality by eliminating artifacts, as they have detrimental effects on subsequent analyses [42]. The most common pre-processing techniques include time-domain filtering, with notch filters to remove power grid interference (50 or 60 Hz, depending on the country), and bandpass filtering to enhance only EEG-related spectral components. Other techniques include resampling, re-referencing, computation of virtual channels and rejection of bad channels. Most of these techniques are common to almost all neuroscience EEG studies, not only to AD diagnosis; unfortunately, they are often not reported in detail, despite being critical for the replication of results.

2.6.1 Bandwidth

Linear, time-invariant bandpass (digital) filtering is by far the most utilized EEG pre-processing technique; its use relies on the assumption that artifacts and EEG do not share spectral components; thus it is possible to design a filter equal to the EEG bandwidth in such a way that only EEG data are kept [15, 1, 43]. While the lower and upper bounds of the bandwidth depend on the spectral components of interest for a given study, usually for EEG signals the lower bound is in the range of 0.1 to 4 Hz, and this aims to remove the baseline drift from EEG signals, and the upper bound varies in the range of 20 to 200 Hz, and is chosen by the trade-off between between the higher frequency of interest and the reduction of high-frequency electromyography (EMG) artifacts. For the lower bound, the majority of the articles reported a value < 1 Hz; in turn, the most common upper bound was 70 Hz. A crucial aspect in the use of digital filters for EEG is their implementation, either infinite impulse response (IIR) or finite impulse response (FIR). One of the main differences is that FIR filters can be designed to have a linear-phase response, i.e. at the output of the filter all frequency components are delayed by the same amount of time (samples), as such the filter does not cause phase distortion, in other words, the waveshape of the signal with spectral components in the passband is not distorted. Moreover, a special case of linear-phase filters are zero-phase filters, where the phase response of the filter is 0, thus, the filter does not cause phase distortion nor delay. Note that zero-phase filters cannot be causal, thus they need to be implemented offline [131, 13].

Unfortunately, artifacts and EEG generally share spectral components; thus they cannot be separated by bandpass filtering the EEG signal. As such, different artifact handling strategies have to be used to reduce the impact of artifacts on the EEG signal [44, 15].

2.6.2 Artifact handling

After pre-processing, several artifacts are still present in the EEG signals; as such, further processing is needed. Three main approaches are typically followed for artifact handling: ignore, reject or remove artifacts. Ignoring artifacts is only considered in real-time applications, as in the case of some BCI paradigms; in the reject approach, artifactual EEG segments are identified and discarded from further processing steps; finally artifact removal aims to reduce or eliminate the influence of artifacts to preserve as much of the EEG data as possible, even in the case of spectral overlap.

Typically, EEG studies have relied on manual artifact rejection, this is to say, meticulous visual inspection of EEG signals is performed by experts in order to identify and discard artifactual EEG segments [41, 15]. In fact, the majority of reviewed articles, 65, relied on this manual selection of “artifact-free” EEG. However, the manual selection approach presents several problems: (*i*) introduces human biases and errors, resulting in irreproducible methods, (*ii*) it is a tedious, time-consuming and expensive task, and (*iii*) it removes EEG segments with artifacts, thus longer recording sessions are required [44]. Moreover, such dependency on human experts hinders the cost benefits provided by the use of EEG signals in the study of AD. As alternative, other methods have been proposed to reduce the human intervention in the artifact handling process. Depending on whether human intervention is required or not, these methods are classified as ‘semi-automated’ or ‘automated’.

Blind source separation (BSS) methods are often used for artifact removal. In these methods the acquired EEG signals ($X(t)$) are considered to be the linear mixture of signals from sources or components ($A(t)$), where some of these sources are related to brain activity and some to artifacts. As the sources are unknown, finding the unmixing matrix, W, that corresponds to the linear mixture, $X(t) = W^{-1}A(t)$, is generally an ill-posed problem as there are many sources and mixing matrices that can lead to the observed EEG signals [132, 133]. However, by placing constraints on the nature of the components, such as orthogonality or independence between components, it is possible to find a mixing matrix (W^{-1}), and its inverse (W) that allows recovering the component signals from the observed EEG signals. As such in BSS methods for artifact removal, the components $A(t)$ are estimated from the registered signals $X(t)$, once in the component space, artifactual components are identified and discarded, keeping only brain-related components $A_c(t)$, which are used with the mixing matrix to reconstruct the EEG signals, $X_c(t)$, without the influence of artifactual components; this process is depicted in Figure 2.2 [132, 134, 135]. Representative BSS methods include, but are not limited to: principal component analysis (PCA) [136], second order blind identification (SOBI) [137], independent component analysis (ICA) [138] and canonical correlation analysis (CCA) [139], where ICA is the most frequently used [45]. As common practice components associated with artifacts still need to be manually identified by experts to be discarded prior to signal reconstruction, hence the 'semi-automated' classification. While these methods drastically reduce the need for human expert input, they still are prone to human bias. As such, to overcome this limitation, automated BSS methods have been proposed to filter artifacts in the component domain [140], discard components based on their statistics [141, 77, 139], or discard components depending on their correlation with artifact-related signals [44].

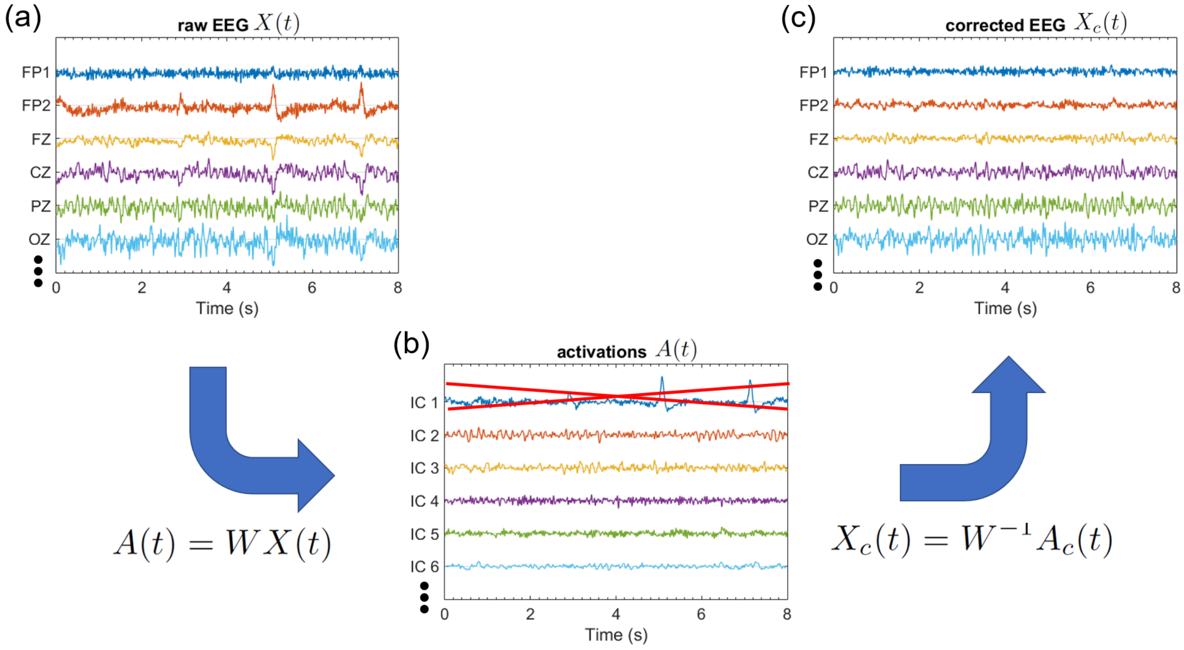

Figure 2.2 – BSS artifact removal approach. (a) Acquired EEG signals are used to compute the components with ICA. (b) Plot of the obtained independent components, $A(t)$, where the first component is related to eye-movement artifacts; thus it is removed from the corrected independent components $A_c(t)$. (c) The corrected EEG signals, $X_c(t)$, are reconstructed from the corrected components; thus the eye-related artifacts are removed.

Additionally, other automated methods include adaptive noise cancellation [142], wavelet denoising [143, 144] and automated rejection of artifactual EEG segments based on their statistical characteristics [141]. From the reviewed articles, eight and nineteen used semi-automated and automated methods respectively. Different artifact handling algorithms have different requirements, such as the number of EEG channels available [145] or the availability of auxiliary channels to convey artifact-related information, such as electrocardiography (EOG) signals to provide information on eye movements [146], and accelerometer and gyroscope signals on head movements [44].

Thorough reviews on artifact handling can be found in [45, 42, 20, 46, 47]. As noted, the literature on EEG artifact handling is extensive; nevertheless there is no current consensus on the best approaches to reduce artifact influence while keeping as much EEG data as possible [45]. However, there is a general agreement that the quality and quantity of the retained EEG data is pivotal to avoid exhausting longer recording sessions.

In Chapter 4 an evaluation of different automated artifact handling (AAH) approaches is provided within the context of rsEEG-based AD diagnosis. Moreover, a discussion on the advantages, disadvantages and challenges for those different approaches is provided.

2.6.3 EEG epoching

For analysis EEG signals are segmented into epochs where the signals present quasi-stationary behaviour. Epoch length can range from 1 to 60 s, and this effect is discussed in Chapter 3. The length of the epochs is dependent of the analyses performed on the EEG. A total of 78 articles reported an epoch length of 10 s or less.

2.6.4 Brain source localization

Given that EEG recordings have their origin in the electric neural activity inside the brain (Section 1.2), by analyzing the observed EEG signals at the scalp it is possible to estimate the electric brain activity that generates the observed EEG. The estimation of the brain activity from EEG signals is known as (brain) source localization or the EEG inverse problem. Similar to the BSS approach, described in Section 2.6.2, the source localization is an ill-posed problem, as the number of unknown parameters is greater than the number of known parameters. As such, constraints have to be used either in the number of sources, or the location of the sources [49, 48]. Among the diverse methods used to solve the EEG inverse problem, the low-resolution brain electromagnetic tomography (LORETA) and its variants are the most popular [48]. The LORETA method computes the current distribution in full brain volume, assuming that the neighbouring neurons are most likely to be active simultaneously and synchronously; due to this assumption, the provided solution is blurred-localized [147]. Further improvements in the LORETA method have led to the development of the standardized LORETA (sLORETA)[148] and exact LORETA (eLORETA)[149], both methods have the same low spatial resolution with zero localization error, however eLORETA provides less-blurry solutions and performs better in the presence of measurement and structured biological noise [150, 149].

The use of source localization methods is frequent in the study of AD, as these methods provide information on the active sources in the brain, helping to identify abnormalities related to the brain presence or progression of the disease. From the reviewed articles, seventeen used source localization; from those, twelve used a layout with 19 electrodes, the rest used layouts with 32 or more electrodes. It is important to note that a greater number of channels usually improves the localization of sources [49, 39], but has negative effects in the practicality of the experiment setup, as mentioned in Section 2.5.3.

2.7 EEG feature extraction for AD study

Feature extraction consists of the collection of techniques that process the EEG signals to derive quantitative characteristics (features) that are proved or potential indicators of the presence or absence of a given phenomenon in the brain activity [50, 41]. These features can be computed from the time-domain EEG signals or from the solutions of source localization. Typically, the proposed rsEEG features for the study of AD have aimed to quantify one of the reported effects of AD on rsEEG signals presented in Section 2.3. As such, in the following subsections we present a survey of features divided in four categories according the effects of AD they aim to evaluate, namely, slowing, reduced complexity, decrease in synchronization or neuromodulatory deficit. In the reviewed articles it was common to observe the use of features aiming to evaluate different effects of AD on the EEG signal in the same article. A full description of all the features here presented is beyond the scope of this doctoral thesis, the interested reader is referred to the corresponding references provided in the section “EEG features” of the systematic review presented in [23].

2.7.1 Slowing

The slowing of the rsEEG was the first effect of AD reported and is the most studied [17]. The quantification of this effect typically relies on spectral features such as absolute and relative EEG-band power, individual alpha peak, frequency peaks in bands, among others. Power features computed from the source localization solutions for classical EEG bands have also been used, e.g., [18]. Lastly, features can be derived from the spectrotemporal representation of the EEG signals [113]. In this sense, the reported slowing features are divided into three categories: spectral, spectrotemporal and source-localization derived. Among these categories, the spectral features, specifically the features related to the power of classical bands and their ratios are the most frequent in the study of AD. From the reviewed articles, 72 explored in diverse ways the slowing of the EEG signal.

2.7.1.1 Spectral power features

As their name suggests, spectral power features measure the power related to the well-defined EEG bands; band power estimation can be performed either in the frequency or time domain [131]. In the frequency domain, the power spectrum density (PSD) is estimated for each epoch with techniques such as the square modulus of the Fourier transform (FT) or the Welch’s periodogram, then the power of band of interested is computed as the integral of the PSD over the correspondent frequency range, as depicted in Figure 1.3d. In the time domain, the pre-processed EEG signal is decomposed by bandpass filters into the time series of each frequency bands of interest, as in Figure 1.3c; then the time series are epoched and power is computed as the average of the samples squared as in (2.1). To allow the comparison among epochs and among subjects, the power of each individual band is then normalized by the pre-processed fullband EEG power.

$$power = \frac{1}{m}\sum_{k=1}^{m} x^2(k) \tag{2.1}$$

2.7.2 Decrease in synchronization

The different metrics to measure the synchronization on EEG signals can be divided according to two criteria, (*i*) the absence or presence of directionality information (causation); and (*ii*) if the metric assumes a linear relationship between the analyzed signals (model-based) or, no assumption of linear relationship (model-free) is made [151]. A general review on synchronization metrics for EEG signals is presented in [152], and reviews on the use of features to assess the decrease in synchronization in AD and MCI subjects can be found in [28] and [153] respectively. A total of 52 articles used features aimed to evaluate the decrease in EEG synchronization due to AD. Among the reported features to measure the decrease in synchronization observed during AD progression, the ones based on coherence, this is to say, magnitude square coherence and phase coherence, are the most used [17].

2.7.2.1 Coherence features

Coherence features have been used as indicators of cortical connectivity, as they measure the co-variance between either two power spectra (termed magnitude square coherence, MSC) or two phase signals (phase coherence) [154]. Coherence is often computed between a pair of electrodes, for a specific EEG band, thus the MSC and phase coherence are defined by (2.2) and (2.3) respectively:

$$MSC = \frac{|P_{xy}|^2}{P_{xx}P_{yy}}, \tag{2.2}$$

$$PhaseCoherence = \arg(P_{xy}), \tag{2.3}$$

where P_{xx} and P_{yy} are the auto-spectra of the signals $x(k)$ and $y(k)$, which are the bandpass filtered signals for electrodes x and y respectively. And P_{xy} is the cross-spectrum between signals $x(k)$ and $y(k)$. The auto-spectra and cross-spectrum can be calculated as:

$$P_{xx} = \frac{1}{m}\sum_{k=1}^{m} \tilde{x}(k)\tilde{x}^*(k), \tag{2.4}$$

$$P_{yy} = \frac{1}{m}\sum_{k=1}^{m} \tilde{y}(k)\tilde{y}^{*}(k), \tag{2.5}$$

$$P_{xy} = \frac{1}{m}\sum_{k=1}^{m} \tilde{x}(k)\tilde{y}^{*}(k), \tag{2.6}$$

where $\tilde{x}(k)$ and $\tilde{y}(k)$ are the analytic signals (concept presented in the Section 3.3.3) for $x(k)$ and $y(k)$ respectively, and $\tilde{x}^{*}(k)$ and $\tilde{y}^{*}(k)$ are the conjugates of the analytic signals.

2.7.3 Reduced complexity

A common approach to evaluate the complexity of EEG signals is the use of nonlinear dynamical analysis, and its features such as correlation dimension [17]. In recent years, the use of features based on information theory has been more frequent; these features include auto-mutual information [155], Shannon entropy [156] and sample entropy [157], among others. From the reviewed articles, 20 of them used complexity metrics in their study of AD.

2.7.4 Neuromodulatory deficit

The amplitude modulation approach has been explored as a tool for the analysis of EEG in order to characterize the deficits in the neuromodulatory activity in the brain due to AD. From the reviewed articles, 5 have explored the neuromodulatory deficit. The changes in the modulating signals or temporal envelopes of the classical EEG frequency bands have been explored by analyzing their statistics [158] or their spectral content [36, 71] with the help of the amplitude modulation rate-of-change features next presented.

2.7.4.1 Amplitude modulation rate-of-change features

These features describe the spectral composition of the temporal envelope of each of the classical EEG bands. Their computation is comprised of three steps: (*i*) the pre-processed EEG is frequency-decomposed by zero-phase FIR filters into the five classical frequency bands (delta, theta, alpha, beta and gamma), (*ii*) the analytic signal for each time series (corresponding to the filtered classical bands) is computed using the Hilbert transform (presented in Section 3.3.3) and from it the temporal envelope is obtained, (*iii*) a second frequency decomposition is performed and the temporal envelope signals are frequency-decomposed in five so-called “modulation bands”, which have been designed to coincide with the frequency ranges of the classical frequency bands. To distinguish between the classic and modulation bands, the latter are referred to as mdelta, mtheta, malpha, mbeta and mgamma. The power of the *band-mband* time series is computed using (2.1). It is important to emphasize that, due to properties of the Hilbert transform (e.g., Bedrosian’s theorem), not all frequency modulation band combinations are valid [36]. Finally, the power of each individual *band-mband* feature is then normalized by the total power of all the valid *band-mband* features. The process to obtain the amplitude modulation rate-of-change features, as well as the description of the valid *band-mband* combinations, is presented in Figure 2.3.

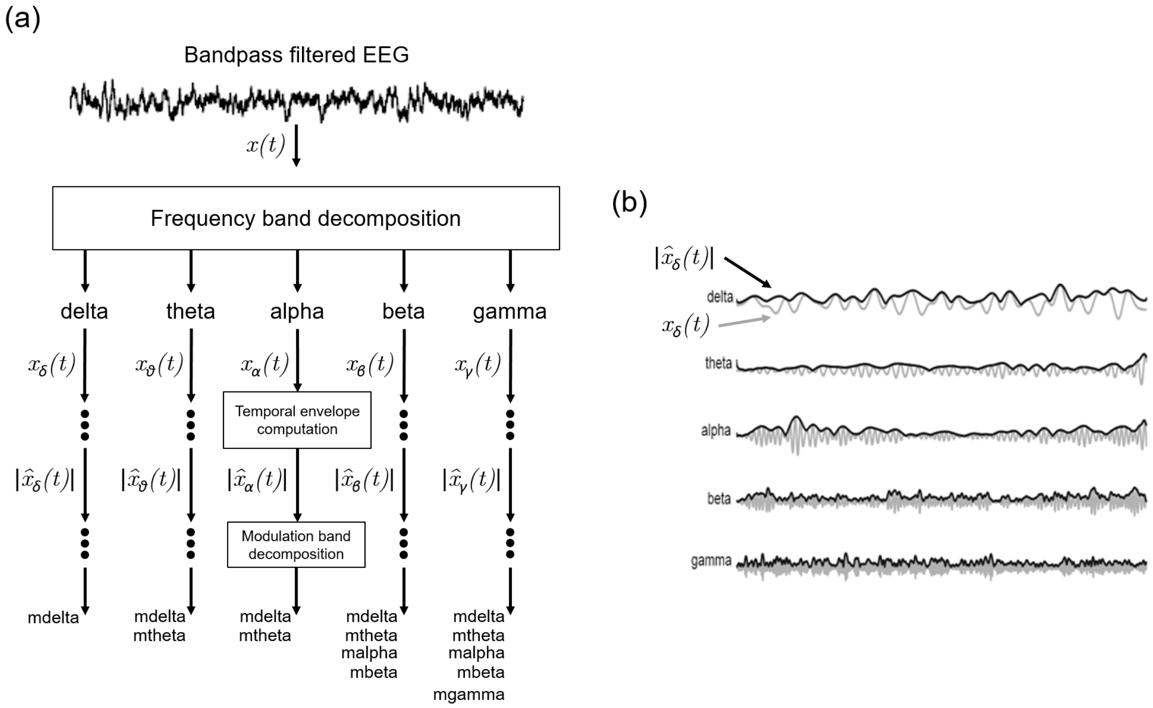

Figure 2.3 – (a) Signal processing steps to compute the amplitude modulation rate-of-change features. (b) Illustration of the bandpass filtered EEG signals and their time envelopes.

The work presented in this thesis builds on these features. For sake of completeness, Chapter 3 expands on the amplitude modulation analysis methods to provide the framework for the EEG features presented in Chapter 6.

2.8 Feature translation

By computing EEG features from the available EEG recordings, for a given epoch a feature vector is obtained, resulting in one or more feature vectors per participant. In this sense, feature translation stands for the set of actions performed on such feature vectors with the aim of building models to: (*i*) evaluate the correlates between the features and AD progression, and/or (*ii*) to perform classification between Nold and AD participants, i.e., diagnosis. In the case of the classification task, the main parts of the feature translation stage are: feature selection, cross-validation and classification.

2.8.1 Feature selection

Feature selection is an optional step that has as goal to select a subset of features to carry on the classification step. As classification based on high-dimensionality feature vectors on limited data (few feature vectors per participant) often leads to bias and over-fitting in classification, the use of feature selection aims to solve these issues in the classification step as it removes redundant or not relevant features, reducing the complexity of the classifier algorithm, which, in general, helps to avoid over-fitting in the classifier [51]. In the AD literature, features are commonly ranked according to their individual predictive value measured as p-value or area under the curve (presented in Section 6.3.3). An evaluation of different feature selection methods in the context of rsEEG-based AD diagnosis can be found in [52].

2.8.2 Cross-validation

When the amount of data (feature vectors) is limited to train and test the classification algorithms, over-fitting can occur by using the same data for training and testing. A way to avoid this is dividing the available data into two sets, one for each task. However, the data selected for training (or testing) may not be representative, leading to biased outcomes. A way to reduce the bias introduced by the data partition consists in repeating the partition several times in different ways; this process is known as cross-validation (CV). One of the most used CV methods is the k-fold CV, where available data is randomly divided into k partitions, then k-1 partitions are used to train the classifier and one set for testing, this process is repeated k times, and the outcome is obtained by combining the outputs obtained for all the k testing partitions; common values for the number if folds are 5, 10 and 100, from these, the 10-fold CV the most commonly used [159]. While the use of 10-fold CV allows to estimate the generalized performance of the proposed classification system, it is prone to optimistic biases because of the random selection of the data partitions, as data samples from the same subject may be found in the training and testing data partitions for the same fold. As a consequence, the classifier is trained and tested on data that are not independent but highly correlated. A way to reduce these biases is the use of the leave-one-subject-out (LOSO) CV. In LOSO CV, from a dataset comprised of data from N participants, the data from N-1 subjects are used to train the classifier while data from the remaining subject are used for testing, this process is repeated for each participant in the dataset. A comparison and discussion about these CV paradigms are presented in Chapter 5.

2.8.3 Classification algorithm

The role of a classification algorithm or classifier is to learn from data the model or transfer function between feature vectors and labels. As the interest is on the diagnosis per subject, once labels have been obtained for each feature vectors, labels related to a given subject need to be combined to provide one label per subject.

According to the type of output provided, classifiers can be divided into two groups, informative or discriminative. Informative classifiers learn the class models, thus to classify a feature vector, the likelihood of each class is computed and the most likely is chosen. Examples of this type of classifier are Bayes quadratic and relevance vector machine (RVM) classifiers. On the other hand, discriminative classification algorithms, such as linear discriminant analysis (LDA) and support vector machine (SVM), learn to model the class boundaries or the binary class membership in order to classify a feature vector directly. In Chapter 4, a comparison between the use of informative and discriminative classifiers for EEG-based AD diagnosis is provided. From reported classifiers, the SVM and LDA algorithms are the most used in the reviewed articles. Lastly, there is a large diversity of classification algorithms in the EEG literature; the interested reader is referred to [51] and [160] for extensive reviews on classification algorithms for EEG signals for BCI applications. In the case of EEG-based AD diagnosis, classification accuracy is the most widely used performance metric. However, given the discrepancies in experiment setups, EEG processing pipelines and cross-validation paradigms, it is not possible to directly compare the results reported in each article.

2.9 Discussion

The reason for using rsEEG recordings for the study of AD mainly lies on its simplicity and on the low impact it represents for the comfort of the elderly participants, who in many cases are suffering dementia. However, this comfort is inversely proportional to the total duration of the session, which is comprised by setup and recording times.

A straightforward path to minimize the recording time is to improve the artifact handling techniques in order to avoid relying on long sessions to compensate for the amount of EEG data that is discarded due to artifacts. The use of semi-automated methods for artifact removal has shown promising results; however it severely compromises the low-cost benefit provided by the utilization of EEG as intervention of human experts is still needed. Thus, specific attention has to be placed on the assessment of AAH techniques. Moreover, many rsEEG features have been proposed for the study of AD; however, their robustness against the presence of artifacts or artifact removal methods has not been explored. Larger electrode layouts lead to better spatial resolution for study the underlying activity and are desirable for EEG features based on source localization. Nevertheless, high-density EEG devices are cumbersome, impractical and imply long preparation times which extend the total duration of the session. In this sense, setup times can be shortened with the use of low-density EEG devices. However, the use of this low-density devices is not common in the EEG-based study of AD, e.g., from the reviewed articles, only five made use of an EEG setup with 8 or less electrodes. Thus the performance of low-density systems needs to be further explored.

2.10 Conclusion

This chapter presented the general structure of an EEG-based system for AD diagnosis and its conforming parts, with the aim of providing a common ground for the aspects reported in the reviewed articles. By using that framework, we discussed the open challenges in the EEG signal processing for the study of AD. These two main challenges, namely, the automated handling of artifacts and its impact on rsEEG features, and the performance of low-density electrode layouts are addressed in Chapters 4 and 5 respectively, to pave the road towards the use of low-cost low-density EEG-based AD diagnosis.

Chapter 3

Spectrotemporal Analysis of EEG Signals

3.1 Preamble

This chapter is compiled from material extracted from the manuscript published as a chapter in the *Reference Module in Biomedical Sciences* book [120].

3.2 Introduction

Commonly, signal processing techniques and methods assume (and frequently require) the signals to be stationary. However, stationarity is a strict assumption rarely met by naturally occurring signals. As such, for practical purposes signals are assumed stationary if they fulfill a softer stationarity definition named ‘wide-sense stationarity’, which requires a constant mean and a time-invariant autocorrelation function. For a zero-mean signal, the equivalent of these conditions in the frequency domain is that of a time-invariant spectrum [53]. In practice, in order to analyze non-stationary signals, as is the case of biomedical signals, with conventional signal processing tools, shorter time segments are considered in which the signal can be treated as stationary. For example, rsEEG signals can be frequently considered quasi-stationary in epochs with duration around 10 s, thus allowing the use of conventional signal processing tools [1, 15, 54, 13]. Therefore, to analyze the non-stationary signals, it is necessary to have a representation capable of registering the changes in frequency content over time, i.e., a spectrotemporal representation.

Interestingly, for a great variety of non-stationary signals, although their spectral content is not constant over time, changes occur in single or multiple periodic ways, resulting in cyclostationarity, which is a second-order periodicity [161, 53]. As such, a non-stationary signal can be modeled as the result of the interaction of two independent signals, a low-frequency signal that changes (modulates) the properties (such as amplitude, phase and/or frequency) of a higher-frequency signal. This interaction is a well known non-linear process called modulation. When the signal is modeled as the product between a modulating signal (low-frequency), and a carrier signal (high-frequency), the modulating signal changes exclusively the amplitude of the carrier signal; this process is denominated amplitude modulation [162, 163].

The amplitude modulation (AM) approach has shown to be an important tool for the analysis and synthesis of non-stationary processes in diverse fields such as telecommunications [164], oceanography [165], speech and music perception [166, 167, 162, 168], as well in the study of biological signals, such as ECG [169, 170], EEG [67, 71, 36], photoplethysmogram (PPG) [171], respiration sounds [172], and neuronal perception of stimuli [173], among others. Indeed, it has been suggested that the presence of amplitude modulation in biological signals is a consequence of the processes of control, synchronization, regulation and inter-system interaction found in biological systems [67]; thus the analysis of spectral changes over time is essential for the study and understanding of biological systems from their measured non-stationary signals.

This chapter presents the theoretical foundation and existing applications of the field of spectrotemporal signal analysis applied to biomedical signals and more specifically EEG. It is organized as follows: First, a brief overview of conventional spectrotemporal signal representations is provided, followed by formalization of the amplitude modulation analysis and the introduction of the modulation spectrogram as an invertible spectrotemporal representation that allows the analysis and synthesis of signals. Lastly, the relationship between the amplitude modulation rate-of-change features (Section 2.7.4.1) and the modulation spectrogram is provided.

3.3 Spectrotemporal representation

The temporal dynamics of the EEG signal are highly non-stationary and exhibit continuous changes on all the time scales [55, 1], i.e., its spectral content change over time; thus the Fourier transform (FT) does not sufficiently describe the dynamics of these signals. In this sense, a time-dependent spectral representation is needed. The fundamental idea to obtain the spectrotemporal representation of a non-stationary signal is to split the signal into shorter segments and perform a time-to-frequency transformation for each segment. Figure 3.1a presents a non-stationary time signal, which is comprised of two major oscillations that are visible in its spectral representation presented in Figure 3.1b; however, the information about when each oscillation occurred is lost. By dividing the signal into shorter segments (Figures 3.1c, 3.1e and 3.1g) and calculating their respective spectral representations (Figures 3.1d, 3.1f and 3.1h), it is possible to study the dynamics of the signal. As the spectral representation is calculated from shorter segments of the signal, the temporal uncertainty is reduced; thus it is possible to localize time changes in the spectral content. However, the value of the minimum resolvable frequency increases, that is, the frequency uncertainty augments. This relationship is known as the Gabor uncertainty principle, where the product of uncertainties or "spreads" in time and frequency for a signal is greater or equal to a fixed constant c.

$$\Delta t \Delta f \geq c \ . \tag{3.1}$$

The spectrotemporal representation or spectrogram of a time signal is a complex-valued time-frequency function $X(t, f)$ that can be written as:

$$X(t, f) = |X(t, f)| e^{j\theta(t,f)} \ , \tag{3.2}$$

with $|X(t, f)|$ being the amplitude spectrogram and $\theta(f, t)$ its associated phase. Analog to the power spectrum, the power spectrogram is defined as $|X(t, f)|^2$. In the literature, it is common to find terms *power spectrogram* and the (complex-valued) *spectrogram* utilized as synonyms. Three of the most utilized approaches to calculate the spectrotemporal representation of a signal are the short-time Fourier transform, the continuous wavelet transform and the Hilbert transform. These approaches are presented in the next subsections followed by a comparison among them.

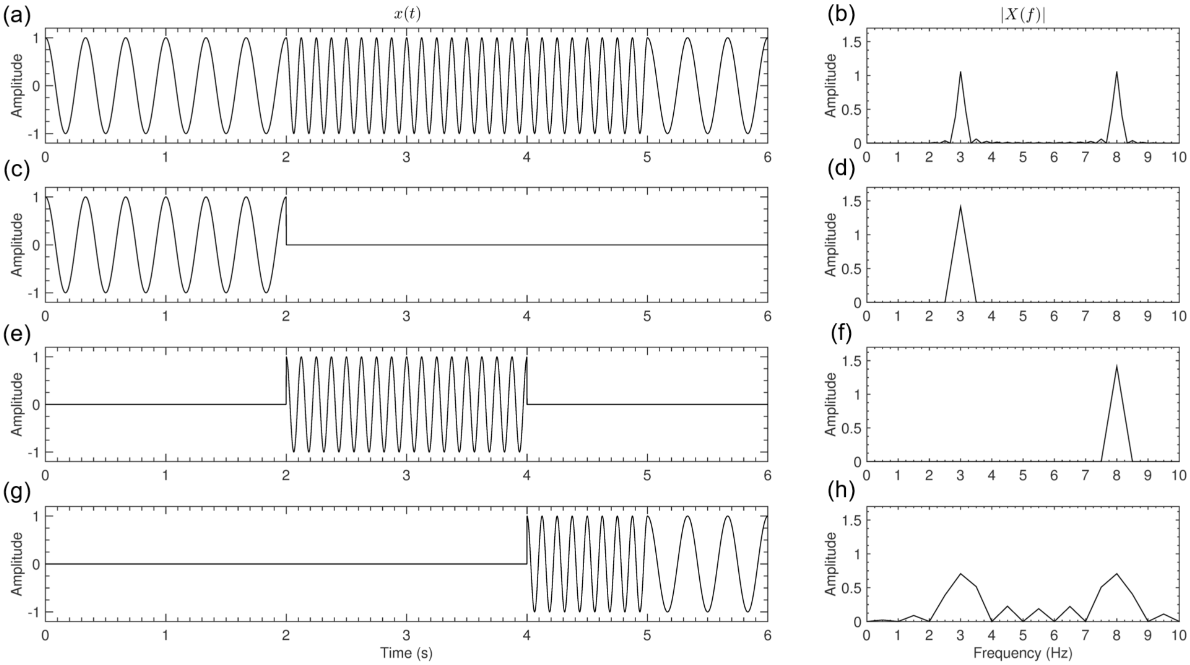

Figure 3.1 – Concept of spectrotemporal representation of a signal. (a) and (b) present a time signal and its amplitude spectrum respectively. (c), (e) and (g) present shorter segments of the complete signal, their corresponding amplitude spectra are depicted in (d), (f) and (h) respectively.

3.3.1 Short-time Fourier transform approach

As presented in Figure 3.1, the natural approach to obtain the spectrotemporal representation of a signal $x(t)$ is to obtain the FT for contiguous shorter segments of the signal; this is in fact the principle in the short-time Fourier transform (STFT) approach. Then, the time-dependent spectral representation of $x(t)$ is defined as:

$$X(t, f) = \int_{-\infty}^{\infty} x(t_1 + t) w(t_1) e^{-j2\pi f t_1} dt_1, \tag{3.3}$$

where $w(t)$ is a window function that possesses two main purposes: (i) segment the signal $x(t)$ into a finite duration T s, and (ii) reduce frequency leakage in the FT by reducing the sharp edges in the signal segment. While the first tentative window choice would be a rectangular window, as shown in Figure 3.1, such window choice presents edge effects due to discontinuities that lead to frequency leakage. In order to reduce the frequency leakage, bell-shaped windows have been proposed, with the Hamming window being the most widely used; it is defined as:

$$w(t) = \begin{cases} 0 & \text{if } |t| > T/2 \\ 0.54 + 0.46\cos(\frac{2\pi t}{T}) & \text{if } |t| < T/2. \end{cases} \tag{3.4}$$

In order to maintain the energy of the original segment of the signal tapered by the window function, the latter is commonly scaled such that its total energy is equal to unity, i.e.,

$$\int_{-\infty}^{\infty} |w(t)|^2 dt = 1. \tag{3.5}$$

The signal processing steps to obtain the spectrotemporal representation using the STFT approach is summarized in Figure 3.2.

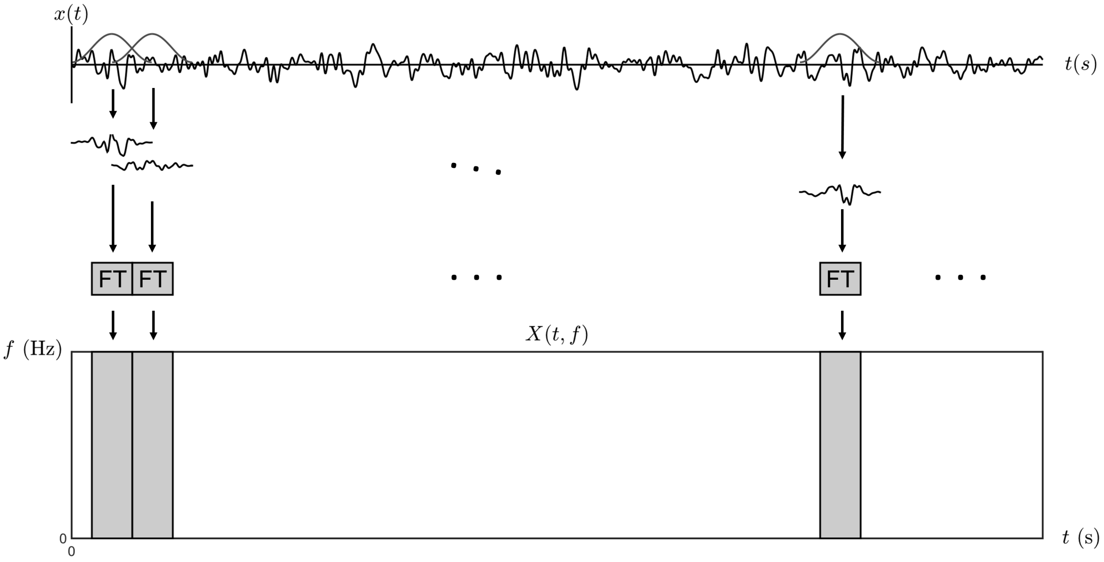

Figure 3.2 – Signal processing steps involved in the calculation of the spectrogram using the STFT approach using the Hamming window.

The duration of the window controls the temporal and, consequently, the frequency resolution, as per (3.1); thus for a window with duration T s, the minimum resolvable frequency is $1/T$ Hz.

When the STFT is continuous, or in the discrete case, the shift t equals one sample; then (3.3) can be further simplified by applying a change to the reference of time and noting that $d(t_1 - t) = dt_1$, i.e.:

$$X(t,f) = \int_{-\infty}^{\infty} x(t_1)w(t_1 - t)e^{-j2\pi f(t_1 - t)}dt_1. \tag{3.6}$$

Given that the function $w(t)$ is time symmetric, $w(t_1 - t) = w(t - t_1)$, and changing the sign in the exponential, then (3.6) can be rewritten as a convolution, thus the formula for the STFT becomes:

$$X(t,f) = \int_{-\infty}^{\infty} x(t_1)w(t - t_1)e^{j2\pi f(t - t_1)}dt_1 = x(t) \star w(t)e^{j2\pi ft}. \tag{3.7}$$

In practice, the shift between consecutive windows t can be larger than one sample. In such cases, the result is a downsampled version of the spectrogram. By utilizing a window length of T s, low frequencies, close to $1/T$ Hz, will have only a few cycles to be accurately resolved, while higher frequencies will have a large number of cycles, thus will be accurately frequency-resolved. An alternative to "equalize" this number of cycles as a function of the frequency is addressed by the use of the continuous wavelet transform, as detailed next.

3.3.2 Continuous wavelet transform approach

The continuous wavelet transform (CWT) provides an alternative to extract time-localized information from a signal by calculating the time convolution of the signal with the analyzing wavelet. To calculate the spectrotemporal representation of a signal by using the CWT, it is necessary to perform the convolution between the signal $x(t)$ and a family (or set) of wavelets $\tilde{\psi}_f(t)$ defined for a specific range of frequencies, i.e.:

$$X(t,f) = x(t) \star \tilde{\psi}_f(t). \tag{3.8}$$

To extract amplitude and phase, the wavelet functions need to be complex-valued and well localized in time and frequency. Among the wavelets that are suitable for complex spectrotemporal signal characterization, the most commonly used is the complex Morlet wavelet, which consists of a complex oscillation with a fixed frequency (frequency localization) tapered by a Gaussian window (time localization), [174, 13, 175]. The template or mother wavelet for the complex Morlet wavelet family is defined as:

$$\tilde{\psi}_{f_0}(t) = A(\sigma_t)e^{-t^2/2\sigma_t^2}\, e^{j2\pi f_0 t}, \tag{3.9}$$

with

$$A(\sigma_t) = \frac{1}{\sqrt{\sigma_t\sqrt{\pi}}} \qquad \text{and} \qquad \sigma_t(f_0) = \frac{n_c}{2\pi f_0}, \tag{3.10}$$

where $e^{j2\pi f_0 t}$ is the complex oscillatory component with frequency of f_0 Hz, $e^{-t^2/2\sigma_t^2}$ is the Gaussian window with a temporal standard deviation of σ_t, $A(\sigma_t)$ is utilized to assure that the wavelet energy is equal to one (as per (3.5)), and the parameter n_c approximately determines the number of cycles at the frequency f_0 inside the Gaussian bell. Substituting (3.9) in (3.8) we obtain:

$$X(t,f) = x(t) \star A(\sigma_t) e^{-t^2/2\sigma_t^2}\, e^{j2\pi f t}. \tag{3.11}$$

Thus, the CWT approach to calculate the spectrotemporal representation of signal $x(t)$ is summarized in Figure 3.3.

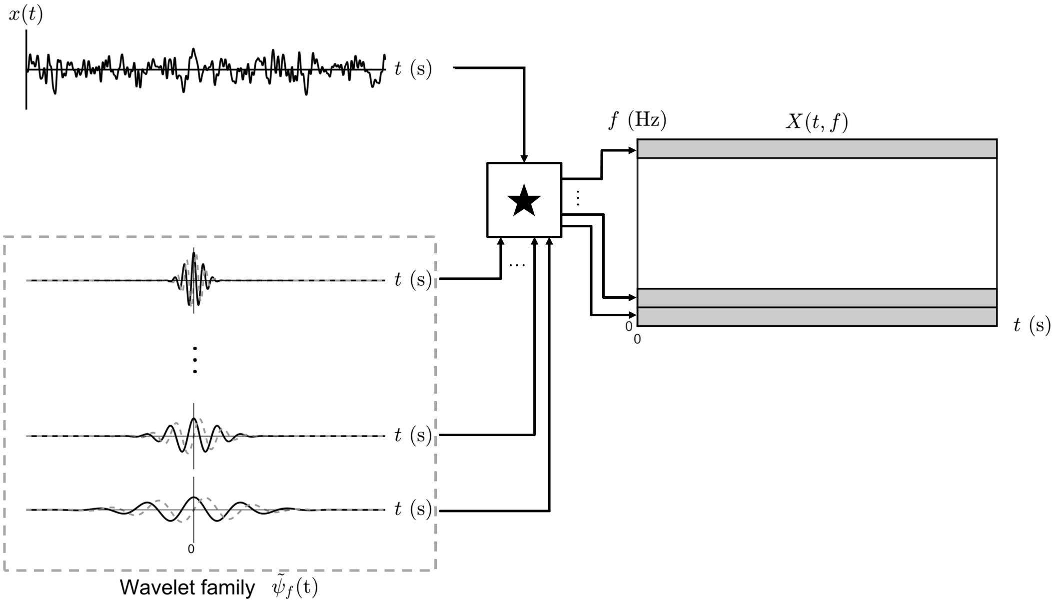

Figure 3.3 – Signal processing steps involved in the calculation of the spectrogram using the CWT approach, the $\star$ symbol indicates the convolution of the time signal with each one of the complex wavelets (the black line is the real part and gray line is the imaginary part) in the wavelet family.

As shown in (3.9), the parameter n_c is related to the time and frequency resolutions in the obtained spectrotemporal representation; in practice values between 4 and 6 provide a good trade-off for the temporal and spectral localizations. As such, the spectra for the set of wavelets defined in (3.9) are given as:

$$\Psi_{f_0}(f) = \mathcal{F}\left\{\psi_{f_0}(t)\right\} = A(\sigma_t)\sigma_t\sqrt{2\pi}\, e^{-f^2/2\sigma_f^2} \star \delta(f - f_0), \tag{3.12}$$

where the bandwidth of the spectrum $\Psi_{f_0}(f)$ is given by the Gaussian component $e^{-f^2/2\sigma_f^2}$ with

$$\sigma_f = \frac{1}{2\pi\sigma_t} = f_0/n_c. \tag{3.13}$$

3.3.3 Hilbert transform approach

Before expanding in the Hilbert transform approach, it is necessary to introduce a concept important for this approach, i.e., that of the analytic signal [163]. Let's start from the generalization that any real bandpass signal $u(t)$ can be rewritten as:

$$u(t) = a(t)\cos(\phi(t)), \tag{3.14}$$

where $a(t)$ and $\phi(t)$ are the instantaneous parameters of the signal; $a(t)$ is the instantaneous amplitude or temporal envelope, and $\phi(t)$ is the instantaneous phase. For a real signal $u(t)$ there is an infinite number of function pairs $[a(t),\phi(t)]$ that satisfy (3.14). However, with the use of the analytic signal it is possible to associate any real signal with a unique pair of functions $[a(t),\phi(t)]$. The analytic signal is a complex temporal representation of a real signal that has been useful in signal processing due its advantageous characteristics. A real signal $u(t)$ is uniquely associated to an analytic signal $\tilde{u}(t)$, if the latter fulfills the following conditions:

1. Is related to the real signal $u(t)$, as $u(t) = \mathrm{Re}\left\{\tilde{u}(t)\right\}$
2. Its spectrum is $\tilde{U}(f) = 2\mathrm{H}(f)U(f)$,

   with $U(f) = \mathcal{F}\left\{u(t)\right\}$ and $\mathrm{H}(f)$ is the Heaviside function defined as:

$$\mathrm{H}(x) = \begin{cases} 0 & \text{if } x < 0 \\ \frac{1}{2} & \text{if } x = 0 \\ 1 & \text{if } x > 0. \end{cases} \tag{3.15}$$

As the analytic signal $\tilde{u}(t)$ is a complex signal, it can be written as:

$$\tilde{u}(t) = u(t) + jv(t) = |\tilde{u}(t)|e^{j\arg(\tilde{u}(t))}. \tag{3.16}$$

The characteristic that has been useful in signal processing is that the module and phase of the analytic signal correspond to the instantaneous amplitude and instantaneous phase of its associated real signal $u(t)$ presented in (3.14) by:

$$a(t) = |\tilde{u}(t)| = \sqrt{u(t)^2 + v(t)^2}, \tag{3.17}$$

$$\phi(t) = \arg(\tilde{u}(t)) = \arctan\left(\frac{v(t)}{u(t)}\right). \tag{3.18}$$

While the analytic signal can be found for broadband signals, its usage for narrow-band limited signals provides meaningful results for the instantaneous parameters. In order to find the analytic signal associated with $u(t)$, the imaginary part of the analytic signal is needed. Expressing the analytic signal in (3.16) in the frequency domain results in:

$$\tilde{U}(f) = U(f) + jV(f). \tag{3.19}$$

From the second condition of the analytic signal, we can determine the spectrum of $v(t)$ by using:

$$\tilde{U}(f) = \begin{cases} 0 & \text{for } f < 0 \quad \text{then: } V(f) = \quad jU(f) \\ U(f) & \text{for } f = 0 \quad \text{then: } V(0) = \quad 0 \\ 2U(f) & \text{for } f > 0 \quad \text{then: } V(f) = \quad -jU(f) \end{cases} \tag{3.20}$$

thus we can rewrite (3.20) as:

$$V(f) = -j\text{sgn}(f)U(f) \tag{3.21}$$

with sgn(f) being the sign function. Indeed, (3.21) is the frequency representation of the Hilbert transform (HT) of a signal, $\mathcal{H}\{\cdot\}$. Multiplying the spectrum $U(f)$ by $-j\text{sgn}(f)$ produces a rotation by -90° in positive frequencies and a rotation of 90° in negative frequencies. For this reason, the Hilbert transform is also frequently known as the quadrature filter. Obtaining the inverse Fourier transform (IFT) of (3.21) results in

$$v(t) = \mathcal{H}\left\{u(t)\right\} = \hat{u}(t). \tag{3.22}$$

Then, the analytic signal for any real signal $u(t)$ can be obtained as:

$$\tilde{u}(t) = u(t) + j\mathcal{H}\left\{u(t)\right\} \tag{3.23}$$

or its equivalent in the frequency domain:

$$\tilde{u}(t) = \mathcal{F}^{-1}\left\{2\mathrm{H}(f)U(f)\right\}. \tag{3.24}$$

In summary, given a real signal $u(t)$, the Hilbert transform allows its corresponding analytic signal to be found, from which, in turn, instantaneous amplitude and instantaneous phase can be computed in a straightforward manner.

In the Hilbert transform approach to calculate the spectrotemporal representation, a broadband signal $x(t)$ is first decomposed in band-neighboring signals by customized filterbanks. The Hilbert transform is then utilized to find the analytic signal for each of the band-neighboring signals, and from them, their respective instantaneous amplitude and instantaneous phase. This process is depicted by Figure 3.4.

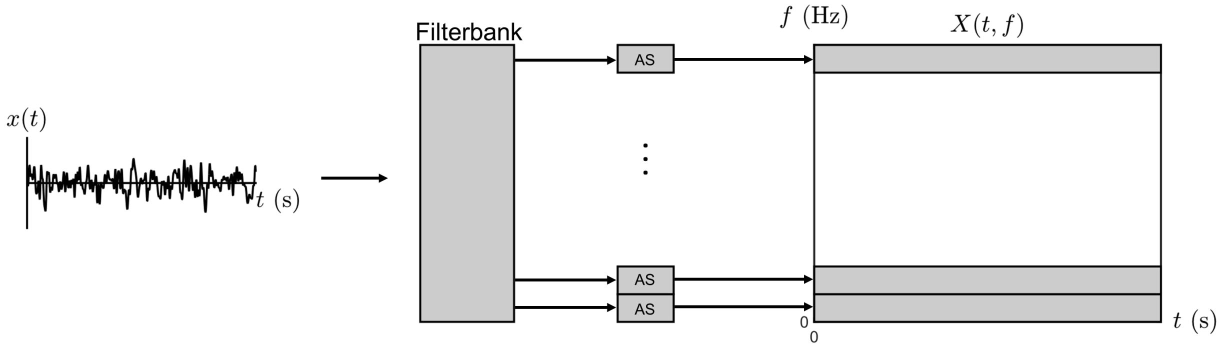

Figure 3.4 – Signal processing steps involved in the calculation of the spectrogram using the HT approach. The block "AS" uses the Hilbert transform to calculate the corresponding analytic signal.

Let's consider a narrow bandpass filter around f_0 Hz, with a real-valued impulse response $c_{f_0}(t)$, transfer function $C_{f_0}(f)$, and an associated bandwidth B_{f_0}, then the result of filtering the signal

$x(t)$ with such a filter is $x_{f_0}(t)$, given as:

$$x_{f_0}(t) = \mathcal{F}^{-1}\left\{X_{f_0}(f)\right\} = \mathcal{F}^{-1}\left\{X(f)C_{f_0}(f)\right\}. \tag{3.25}$$

The analytic signal for $x_{f_0}(t)$ can then be obtained by substituting (3.25) in (3.24), thus resulting in:

$$\tilde{x}_{f_0}(t) = \mathcal{F}^{-1}\left\{2\mathrm{H}(f)X_{f_0}(f)\right\} = \mathcal{F}^{-1}\left\{2\mathrm{H}(f)X(F)C_{f_0}(f)\right\}, \tag{3.26}$$

which can be written as a convolution operation

$$\tilde{x}_{f_0}(t) = x(t) \star \mathcal{F}^{-1}\left\{2\mathrm{H}(f)C_{f_0}(f)\right\}. \tag{3.27}$$

Note that the point-wise product $2\mathrm{H}(f)C_{f0}(f)$ scales the transfer function $C_{f0}(f)$ and only its positive frequency part is kept. This new one-side filter can be expressed as a lowpass filter $C(f)$ with bandwidth equal to B_{f_0} shifted by f_0,

$$\tilde{x}_{f_0}(t) = x(t) \star \mathcal{F}^{-1}\left\{C_{B_{f_0}}(f - f_0)\right\} = x(t) \star c_{B_{f_0}}(t)e^{2\pi f_0 t}. \tag{3.28}$$

Note that the subindex B_{f_0} in the lowpass filter $c_{B_{f_0}}(t)$ does not indicate the central frequency of the filter, but the bandwidth B_{f_0} associated with it. Finally, when this process is repeated for all the filters in the filterbank, the spectro-temporal representation of $x(t)$ obtained by using the Hilbert transform approach can be expressed as:

$$X(t, f) = x(t) \star c_f(t)e^{j2\pi f t}, \tag{3.29}$$

where the subindex f in the lowpass filter impulse response $c_f(t)$, indicates that the filter bandwidth is associated with a given value of f.

3.3.4 Comparison among approaches

By comparing equations (3.7), (3.11) and (3.29) that are used to calculate the spectrogram with STFT, CWT and HT approaches respectively, it is possible to observe that the spectrotemporal representation $X(t, f)$ is the result of the convolution between the time signal $x(t)$ and a tapered complex oscillatory function $e^{j2\pi ft}$. Such an algorithm can be written in a more general fashion as:

$$X(t,f) = x(t) \star \lambda_f(t)e^{j2\pi ft}, \tag{3.30}$$

where $\lambda_f(t)$ is a real-valued time window function (lowpass filter), which can be different for different values of f. As a consequence, the product $\lambda_f(t)e^{j2\pi ft}$ can be seen as a filterbank. The main difference among the STFT, CWT and HT approaches lies in how the window $\lambda_f(t)$ is defined, and as consequence how the time and frequency uncertainties are handled.

The STFT approach can be obtained by making $\lambda_f(t) = w(t)$ in (3.30), where $w(t)$ is a window function with constant duration T s for all the values of f. This is reflected as a time resolution Δt and consequently a constant frequency resolution Δf in the time-frequency space (see Figure 3.5a). The uniformity of the time-frequency bins presents a drawback for low frequency components, i.e., those close to $1/T$ Hz, as they are not accurately represented since the window duration comprises just a few cycles at those frequencies, thus resulting in frequency leakage. The division of the time-frequency space is optimized when the window duration is equal to the duration of the stationary segments of the signal. The CWT approach, in turn, uses an infinite time Gaussian window with a standard deviation inversely proportional to f, as per (3.10). Then, according to (3.11), $\lambda_f(t) = A(\sigma_t)e^{-t^2/2\sigma_t^2}$. Despite the fact that the duration of the Gaussian bell is infinite, it is possible to determine a nominal or effective duration Δt, which corresponds to the duration of a rectangular pulse with amplitude such that the area of this rectangle is equal to the area of the original signal, i.e.:

$$\Delta t = \frac{\int_{-\infty}^{\infty} A(\sigma_t)e^{-t^2/2\sigma_t^2}\,dt}{A(\sigma_t)} = \sigma_t\sqrt{2\pi}. \tag{3.31}$$

As such, for the CWT approach the minimum resolvable frequency Δf is equal to $1/\Delta t$ (Figure 3.5b). Lastly, in the HT approach, $\lambda_f(t) = c_f(t)$, where $c_f(t)$ is a lowpass filter that is defined according to the application. If the window $c_f(t)$ is constant for different values of f, the sectioning of the time-space space is similar to that obtained with the STFT. On the other hand, if the duration of $c_f(t)$ is inversely proportional to f, then the time-frequency space sectioning will be similar to the one obtained with the CWT approach. However with the use of the HT approach, the duration of the window for each value of f is defined in an application-wise manner (Figure 3.5c). Overall, despite the STFT, CWT and HT approaches handle the uncertainty principle differently; neither is capable of avoiding the trade-off between time and frequency uncertainties. Given the correct parameters, it is possible to obtain similar results with the three approaches; an empirical comparison between these methods can be found in [176].

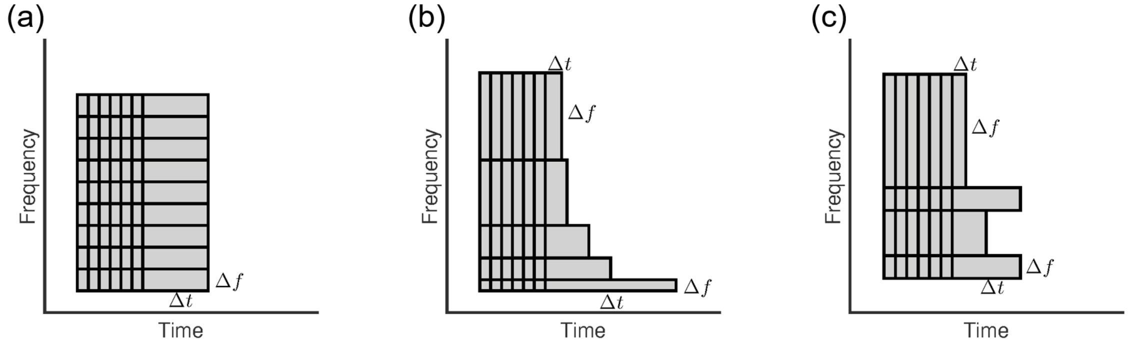

Figure 3.5 – Time-frequency uncertainty for: (a) STFT, (b) CWT and (c) HT approaches.

The power spectrogram, which is defined as $|X(t,f)|^2$, can be utilized to compute the power of the signal for a specific time interval (τ) in the range of frequencies (ν) as:

$$power_{\tau\nu} = \int_{\tau}\int_{\nu} = |X(t,f)|^2 df dt. \tag{3.32}$$

However, this only holds if filters in filterbank $\lambda_f(t)e^{j2\pi ft}$ are orthogonal, as in the STFT approach and the HT approach (if the filterbank is designed with that property). For the CWT, when the central frequency for the kernels is linearly spaced, the filterbank $\lambda_f(t)e^{j2\pi ft}$ is not orthogonal, which has as consequence that the time series related to each wavelet kernel are highly correlated; therefore redundant information is present. However, in the analysis of biomedical signals, this orthogonality requirement can be loosened and relevant information can be derived directly from the spectrotemporal representation.

3.3.5 Spectrotemporal analysis in EEG

In order to illustrate the similarities and differences in the approaches to calculate the spectrotemporal representation of a signal, Figure 3.6 shows the power spectrograms computed using the STFT, CWT and HT approaches for a 10-second segment of rsEEG signal acquired in the electrode Cz during closed-eyes awake condition.

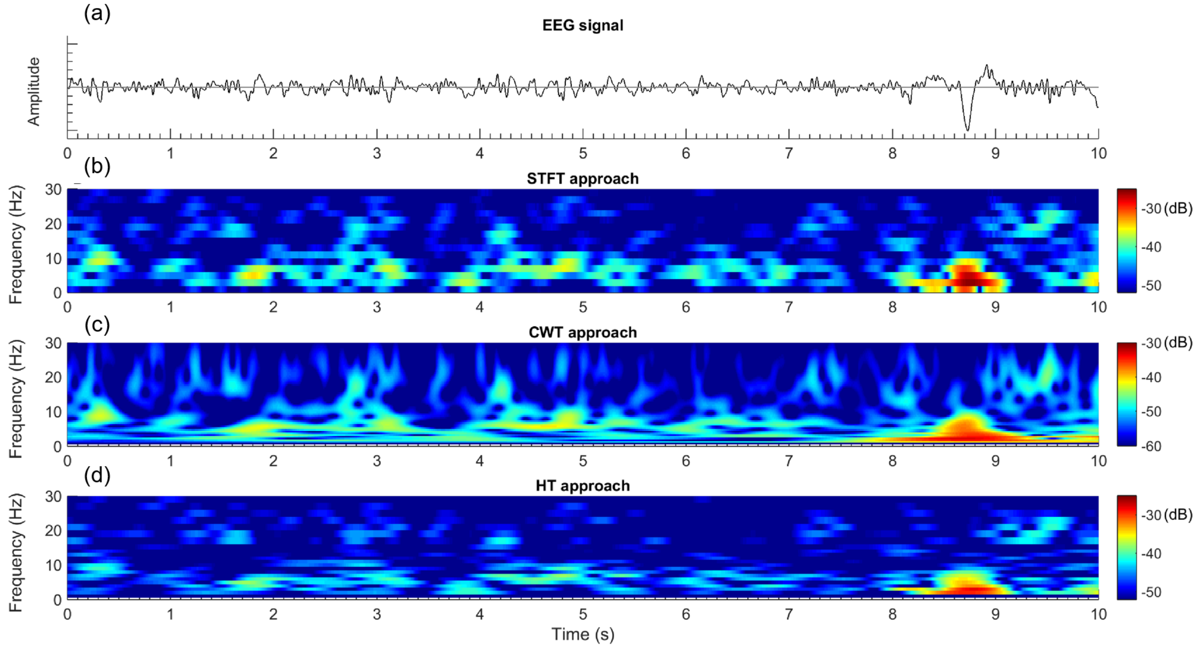

Figure 3.6 – Comparison of power spectrograms obtained with different approaches. (a) EEG signal. (b) Power spectrogram obtained with the STFT approach using a window duration of 0.5 s. (c) Power spectrogram calculated using the CWT with a parameter $n_c = 6$. (d) Power spectrogram obtained with the HT approach with a filterbank comprised of 23 non-overlapping filters, of which 15 are 1-Hz-bandwidth filters in the range 0 to 15 Hz, and 8 are 2-Hz-bandwidth filters in the range 15 to 31 Hz.

The utilization of the spectrotemporal representation of EEG signals has been of grand utility as it allows to explore the non-stationary characteristics of EEG signal, e.g., the estimations of the instantaneous amplitude and phase obtained with this representations are the base for analysis such as connectivity for different frequencies, power-power, power-phase, and phase-phase cross-frequency couplings. The analysis of the EEG spectrotemporal representation has been used to study ERPs [55, 13, 56], ERD and ERS for motor-imagery BCI [57], sleep EEG studies [58], and in the case of awake rsEEG for the detection of events that disrupt the “stationary” behaviour, such as epileptic seizures [59].

In the context of AD, wavelet transform (either continuous or discrete) is the most commonly used approach to compute the spectrotemporal representation of the EEG signals. From this representation several features have been proposed to measure the effects of AD on rsEEG, e.g., the statistics of the CWT coefficients [60], complexity measurements of the CWT spectrotemporal representation [61], wavelet coherence [62, 63], HT- and CWT-derived phase synchrony [65], parameters from the (discrete) wavelet [113], wavelet compression [177], among others. Moreover, diverse works have explored the utilization of models based on time-frequency “bumps” to describe the spectrotemporal representation of the EEG signals [64, 65], or of the components obtained with BSS [66], with the final goal of developing features or performing synchronization assessment [65] to discriminate between healthy controls and AD participants.

While the spectrotemporal representation $|X(f,t)|$ is helpful to identify time-occurring spectral changes, it does not provide information on the periodic nature of these changes. The modulation spectrogram as defined next, overcomes this limitation.

3.4 Modulation spectrogram

The spectrotemporal representation of a signal $x(t)$ presents information on how amplitude and phase change over time for different frequency components. A natural extension of that representation is the modulation spectrogram, which characterizes those amplitude changes in the framework of amplitude modulation analysis, providing a representation of second-order periodicities, i.e., modulation frequencies. These modulation frequency components are sometimes referred to as “hidden periodicities” as they are not present as spectral components in the “conventional” frequency representation of the $x(t)$ signal.

In the framework of amplitude modulation analysis, a signal $x(t)$ can be expressed as the product of a low-frequency modulating signal $m(t)$, and a high-frequency or carrier signal $c(t)$:

$$x(t) = m(t)c(t), \tag{3.33}$$

with the following two assumptions: (*i*) there is no spectral overlap between $m(t)$ and $c(t)$, and (*ii*) $m(t)$ is a real non-negative signal. When $m(t)$ takes negative values, the amplitude modulation process becomes over-modulated, i.e., possesses a modulation index larger than 1. In this scenario, the modulating signal $m(t)$ cannot be recovered by analyzing only the envelope of the carrier signal $c(t)$.

Let's use the following numerical example to introduce the concept of the modulation frequency domain; consider a time signal $x(t)$ defined as:

$$x(t) = (1 + \cos(2\pi f_m t))(\cos(2\pi f_c t)), \tag{3.34}$$

with $f_m = 2$ Hz and $f_c = 25$ Hz. Comparing (3.34) with the AM model presented in (3.33), it can be seen that the modulating signal is $\cos(2\pi f_m t)$ (an offset of amplitude 1 is added to ensure that the modulating signal is non-negative), and the carrier signal is $\cos(2\pi f_c t)$. The time and frequency representations for $x(t)$, $m(t)$ and $c(t)$ are depicted by Figure 3.7. The spectrum for $x(t)$ can be found by using the product-of-cosines trigonometric identity, and is equal to:

$$\cos(\alpha)\cos(\beta) = \frac{1}{2}\left[\cos(\alpha + \beta) + \cos(\alpha - \beta)\right], \tag{3.35}$$

then,

$$x(t) = \cos(2\pi f_c t) + \cos(2\pi f_m t)(\cos(2\pi f_c t),$$
$$x(t) = \cos(2\pi f_c t) + \frac{1}{2}\left[\cos(2\pi(f_c + f_m)t) + (\cos(2\pi(f_c - f_m)t)\right],$$

whose spectral representation is:

$$X(f) = \frac{1}{2}\left[\delta(f - f_c) + \delta(f + f_c)\right] + \frac{1}{4}\left[\delta(f - f_c - f_m) + \delta(f - f_c + f_m) + \delta(f + f_c - f_m) + \delta(f + f_c + f_m)\right]$$
$$X(f) = \frac{1}{2}\left[\delta(f - 25) + \delta(f + 25)\right] + \frac{1}{4}\left[\delta(f - 27) + \delta(f - 23) + \delta(f + 23) + \delta(f + 27)\right]$$

The frequency representation of the modulating signal $m(t)$ depicted in Figure 3.7a, is the modulation spectrum, which is shown in Figure 3.7b. As such, the modulation spectrum $M(f)$ is an indicator of the second order periodicities present in the signal $x(t)$. Unlike the carrier signal spectral components of $C(f)$, shown in Figure 3.7d, the spectral components of modulating signal $M(f)$ are not represented in the spectrum $X(f)$ depicted in Figure 3.7f, but can be obtained by analyzing the changes in amplitude for the first periodicity (see Figure 3.8).

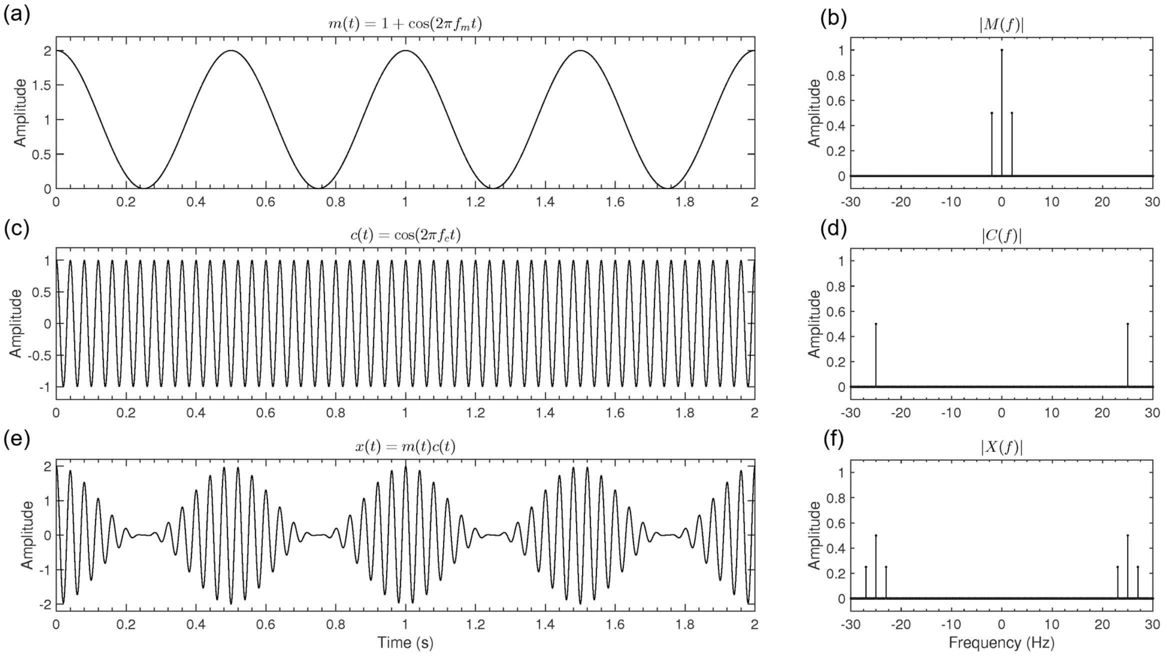

Figure 3.7 – Illustration of the AM process. (a) Temporal representation for the modulating signal $m(t)$; its spectrum is shown in (b). (c) Carrier signal $c(t)$; its spectrum is shown in (d). (e) Resulting signal $x(t)$; its spectrum is shown in (f).

According to (3.33), the modulating and carrier signals are not necessarily monochromatic waves; as in the example signal described in (3.34). Nevertheless, the instantaneous amplitude and phase need to be calculated in narrow-band signals to possess a straightforward physical meaning. In the spectrogram $X(t, f)$, for a given frequency component f_0, its amplitude changes over time are given as $|X(t, f_0)|$; these changes can be studied in the framework of amplitude modulation. This is to say, the spectrum for the amplitude time-series of each frequency component in $|X(t, f)|$ is calculated; thus, the modulation spectrogram is a 2D complex-valued representation of the conventional frequencies components versus their modulation spectra, i.e.:

$$X(f, f_{mod}) = \mathcal{F}_t \{|X(t, f)|\} = |X(f, f_{mod})| e^{j\theta(f, f_{mod})} \ , \tag{3.36}$$

where $\mathcal{F}_t \{\cdot\}$ indicates the Fourier transform over the time dimension and f_{mod} indicates the modulation frequency dimension. The signal processing steps required to obtain the modulation spectrogram are depicted in Figure 3.9. In essence, the modulation spectrogram consists of a double transformation: given a time signal $x(t)$, its corresponding spectrotemporal representation $X(t, f)$

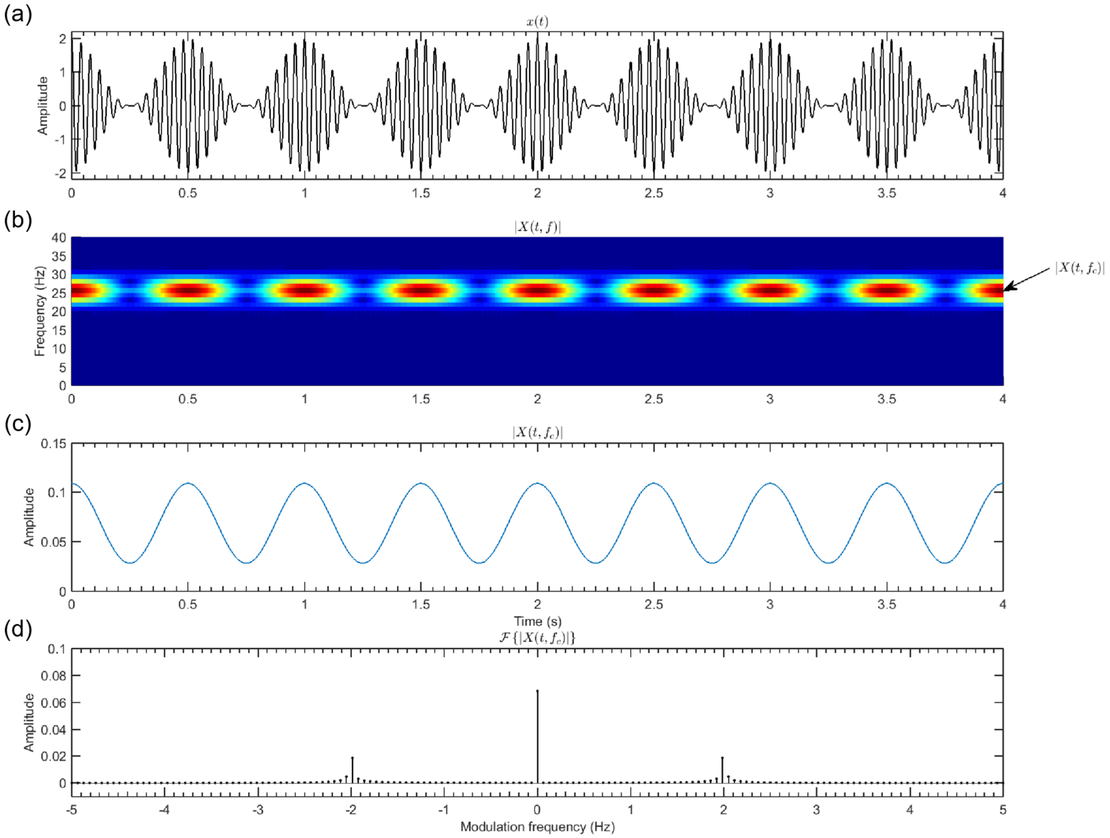

Figure 3.8 – Amplitude modulation analysis. (a) Temporal representation for signal $x(t)$; this signal is the result of the AM process depicted in Figure 3.7. (b) Its corresponding amplitude spectrogram $|X(t,f)|$, where the row corresponding to the amplitude temporal changes in the frequency of the carrier signal f_c is indicated. (c) Time series for the amplitude changes for $|X(t,f_c|$. (d) Its corresponding spectral representation.

is computed, then a time-frequency transformation is performed over the amplitude time series for all the frequency components of $|X(t,f)|$, hence obtaining the modulation spectrogram $X(f,f_{mod})$.

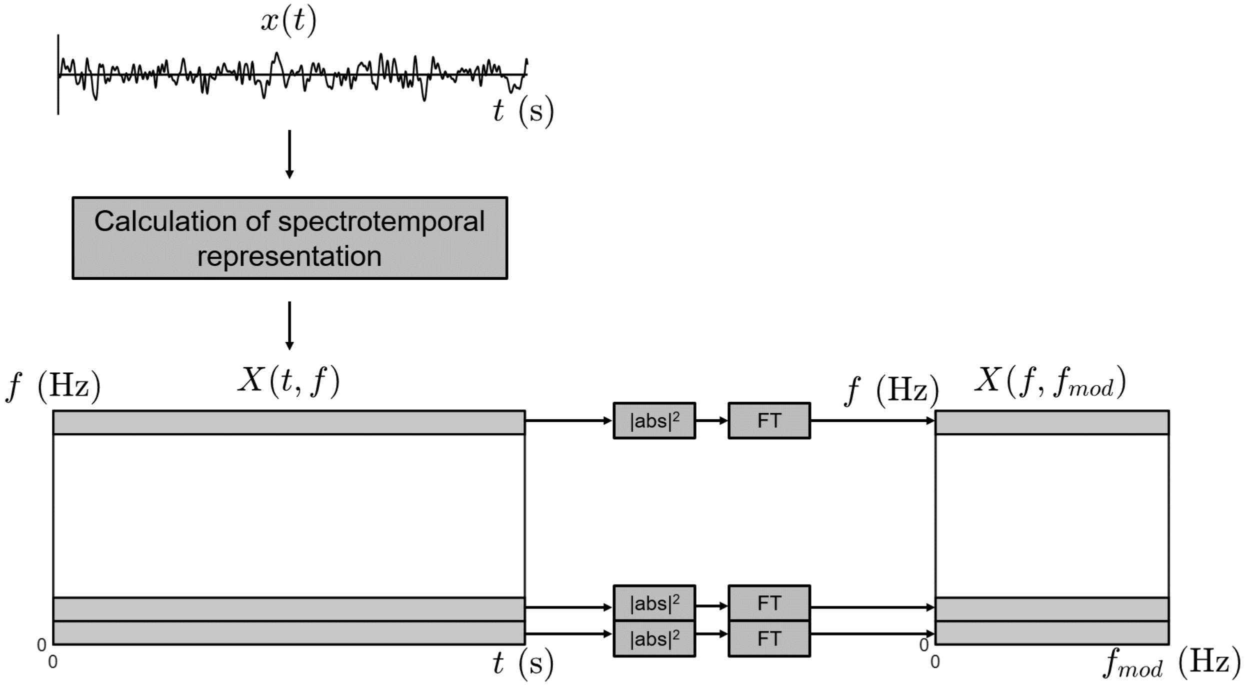

Figure 3.9 – Signal processing steps involved in the calculation of the modulation spectrogram from the complex spectrogram of a time signal. The block "|abs|" indicates the absolute value, and the "FT" indicates the use of the Fourier transform.

Similar to the power spectrum and the power spectrogram, the power modulation spectrogram is defined as $|X(f, f_{mod})|^2$.

The amplitude modulation analysis differs from the "cross-frequency coupling" analyses, as the latter ones typically measure the correlation between power-power, power-phase, or phase-phase between two frequency components of a signal. Therefore, cross-frequency coupling methods cannot be utilized to study modulation as the AM modulating frequencies do not appear as elements in the frequency axis in $|X(t, f)|$. The modulation spectrogram is the modulation-domain representation of a real signal that provides the possibility of studying non-linear interactions in biological systems.

3.4.1 Filtering in the modulation domain

Often, the signal of interest is measured in a noisy manner or is corrupted by co-occurring phenomena. These competing signals overlap in time and frequency but, given their varying nature, they become separable in the modulation domain. Given that the modulation spectrogram is the result of a double transformation, as depicted in Figure 3.9, if both transformations are invertible, then the time signal, $x(t)$, can be recovered from its modulation spectrogram $X(f, f_{mod})$. This process opens the door to filtering in the modulation domain, i.e., enhance or cancel components that are only separable in the modulation domain, and then the time signal is recovered. The signal processing steps required to perform filtering in the modulation domain for a signal $x(t)$ are depicted in Figure 3.10.

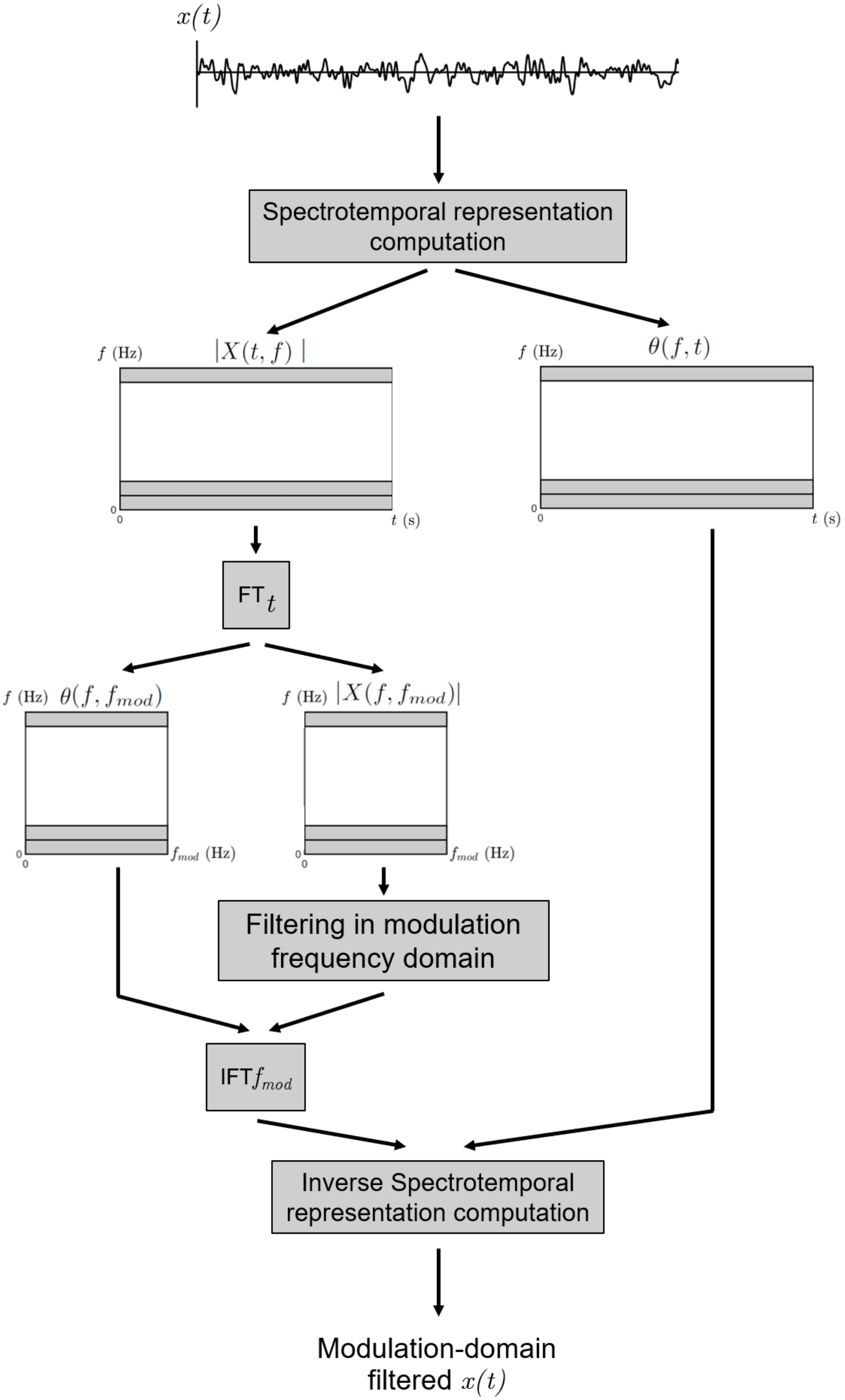

Figure 3.10 – Signal processing steps involved in filtering in the modulation domain a time signal. The block “FT$_t$” indicates the use of the Fourier transform over the time axis, and the block “IFT$f_{mod}t$” indicates the use of the inverse Fourier transform over the modulation frequency axis.

From Figure 3.10, it is possible to note that the processing is performed on the amplitude spectrogram and the phase of the original mixed signal is used for reconstruction. Filtering in the modulation domain has been proven to be useful in applications such as heart and lung sound separation [172] and ECG enhancement [170].

3.4.2 Relationship between modulation spectrogram and AM rate-of-change features

The AM rate-of-change features presented in Section 2.7.4.1 were proposed as a way to characterize the spectral power distribution of the temporal envelopes for the classical EEG bands. When these features are compared with the modulation spectrogram formulation, it is possible to appreciate that the AM rate-of-change features also consist of two consecutive transformations. First a spectrotemporal transformation is carried out with bandpass filters (designed after the classical EEG bands) followed by the HT; for the second transformation, the spectral analysis of the temporal envelopes is performed in discrete frequency bins that correspond to the classical EEG bands as shown in Figure 2.3. As such, the relationship between the AM rate-of-change features and the modulation spectrogram is presented in Figure 3.11.

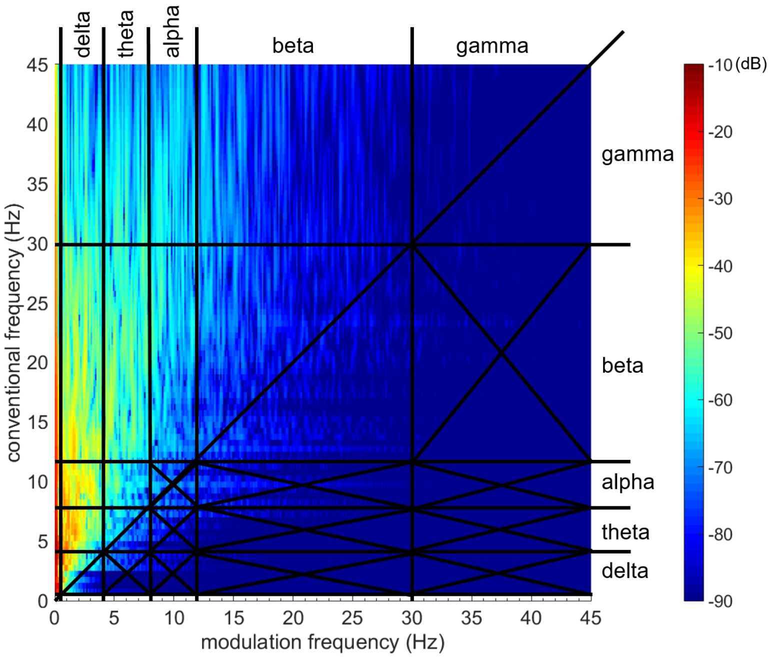

Figure 3.11 – Relationship between power modulation spectrogram and AM rate-of-change features.

In this sense, an AM rate-of-change feature defined as $band - mband$ can be computed from the modulation spectrogram as the integral over the region delimited by *band* in the conventional frequency axis and *mband* in the modulation frequency axis:

$$band - mband = \int_{mband} \int_{band} = |X(f, f_{mod})|^2 df\, df_{mod}. \tag{3.37}$$

From Figures 3.11 and 3.37, an imposed limitation in modulation domain regions that are studied can be appreciated. In Chapter 6 we present and discuss the results obtained by using the entire modulation spectrogram for AD diagnosis.

3.4.3 Modulation spectrogram of EEG

One of the aspects that have not been widely explored is the phenomenon of amplitude modulation of the EEG [67]. An outstanding characteristic of rsEEG is that its temporal dynamics are non-stationary and present continuous changes on different time scales [68]. These changes are driven or affected by a variety of mechanisms including the effects of the brain pathways (or systems) of neurotransmitters such as dopamine, acetylcholine, serotonin, norepinephrine, etc. The projections of these pathways are widely spread in cortical areas and are very likely to be an important source of the observed temporal variability in the brain activity dynamics and thus in rsEEG recordings [55, 69, 70].

The modulation analysis of rsEEG has been suggested as a promising approach for the characterization and assessment of different neurological disorders. In the study of AD, for example, a neuromodulatory abnormality has been reported with potential origin in the impaired brain pathways caused by neuronal loss. The performance of the AM rate-of-change features, for the classification of healthy controls versus mild/moderate AD (90.6% accuracy), surpasses the performance obtained with traditional features such as spectral-peak per EEG band (81.3% accuracy). The AM rate-of-change features, in fact, were shown to provide complementary information to traditional features; thus they could be fused to obtain further gains [36, 71]. These results show that the modulation spectrogram can be useful for AD diagnosis. To illustrate this, the average (across electrodes) power modulation spectrograms (obtained with the STFT approach) for healthy controls and mild Alzheimer's disease patients are presented in Figures 3.12a and 3.12b, respectively. An extensive exploration on the use of the modulation-domain representation of the rsEEG signals for AD diagnosis is provided in Chapter 6.

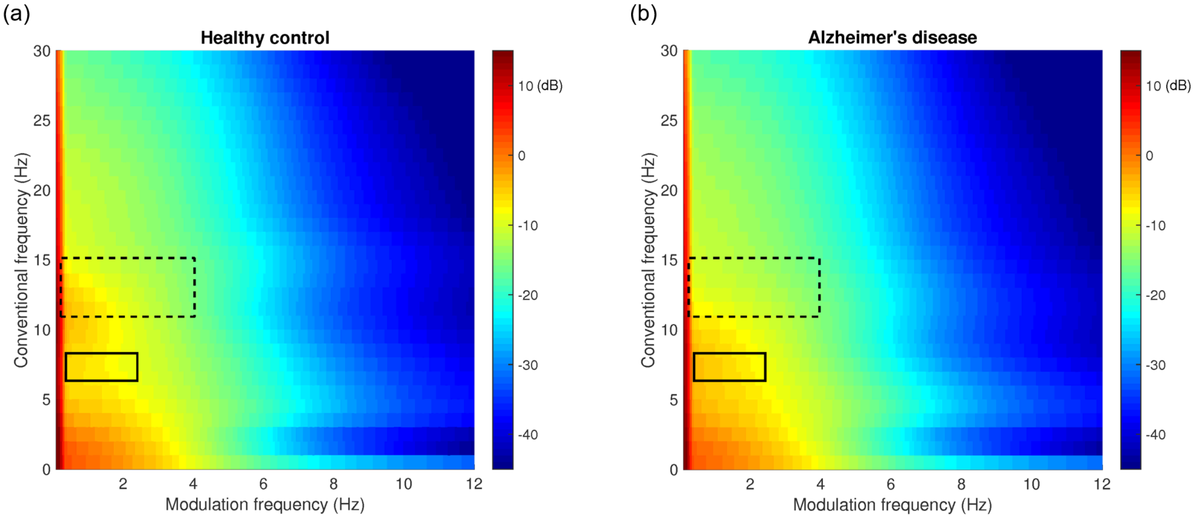

Figure 3.12 – Average power modulation spectrogram for: (a) healthy control and (b) mild Alzheimer's disease patients. The main differences are indicated in the black boxes.

3.5 Conclusions

In the last few years, the so-called amplitude modulation approach has shown to be relevant in the analysis and synthesis of quasi- and non-stationary signals where the conventional spectral analysis has limitations. In this chapter, we have presented the theory and EEG applications related to the spectrotemporal and amplitude modulation analysis of EEG signals. Moreover, the concept of the modulation spectrogram was introduced and presented as a useful tool for analysis of rsEEG as it allows for the discovery of new insights for AD diagnostics, as well as filter noisy signals in conditions where conventional time- and frequency-domain analyses are not suitable. The amplitude modulation analysis of rsEEG for AD is used in Chapter 6.

Chapter 4

Towards Automation: Effects of EEG Artifacts on AD diagnosis

4.1 Preamble

This chapter is compiled from material extracted from the manuscripts published in *Frontiers in Aging Neuroscience* [115], and in the proceedings of the *5th SSNIP-IEEE Biosignals and Biorobotics Conference: Biosignals and Robotics for Better and Safer Living* [90].

4.2 Introduction

As mentioned in Sections 1.4 and 2.6.2, EEG data quality and quantity are compromised by the presence of artifacts; as such, typically EEG-based AD diagnosis systems have relied on manual selection by experts of “clean” EEG segments. In order to progress towards automated EEG-based diagnosis of AD, the impact of using AAH methods needs to be investigated.

The detrimental effects of EEG artifacts within the scope of AD diagnosis have not been deeply investigated. By 2014, the potential benefits and drawbacks of using AAH algorithms were still unknown regarding AD diagnosis. The aim of this chapter is to present the methods and discuss the results from the exploration performed on the combinations of automated methods for artifact handling (rejection and removal) and rsEEG features, as well as the impact on overall AD diagnosis accuracy. Recent work presented in [178] proposed a method to automate the identification of artifactual BSS components and compared it against the identification performed by experts. Besides reporting promising results on the use of a sample entropy metric for the identification of artifactual BSS components, the authors reported an improvement in the classification (Nold vs AD) accuracy by using the enhanced EEG signals based on the manual identification of artifactual BSS components performed by experts, compared with the performance of using the bandpass filtered raw EEG data.

4.3 Materials and methods

4.3.1 Brazil AD dataset

Participants

Fifty-nine participants were recruited from the Behavioral and Cognitive Neurology Unit of the Department of Neurology and the Reference Center for Cognitive Disorders at the Hospital das Clinicas in São Paulo, Brazil. AD diagnosis was made by experienced neurologists according to NINCDS-ADRDA criteria [72] and classified based on the Brazilian version of the MMSE [73]. Participants were divided into three groups. The first group (Nold) consisted of 24 cognitively healthy normal elderly controls; the second group (AD1) comprised 20 mild-AD patients; the third group (AD2) consisted of 15 patients with moderate-to-severe AD symptoms; see Table 4.1 for further details in the demographics of this dataset. Inclusion criteria for the Nold group included a CDR score $= 0$ and MMSE score ≤ 25, as well as no indication of functional cognitive decline. Inclusion criteria for the AD1 group, in turn, included $0.5 \leq$ CDR ≤ 1 and MMSE ≤ 24; lastly, inclusion criteria for the AD2 group were CDR score $= 2$ and MMSE ≤ 20. For inclusion to the two AD groups, an additional criterion used was the presence of functional and cognitive decline over the previous 12 months based on detailed interviews with knowledgeable informants. Patients from the AD cohorts were also screened for diabetes mellitus, kidney disease, thyroid disease, alcoholism, liver disease, lung disease or vitamin B12 deficiency, as these can also cause cognitive decline. Ethics approval was obtained from the Research Ethics Office and participants consented to participate in the study. Data from this study is referred to henceforth as the “Brazil” AD dataset.

Table 4.1 – Demographics for the Brazil AD dataset.

Group identifier	Subjects (female)	Age [years]	Education [years]	MMSE
Nold	24 (12)	66.3 ± 8.8	10.0 ± 3.4	28.5 ± 1.7
AD1	20 (11)	74.8 ± 6.3	5.3 ± 3.0	19.2 ± 5.2
AD2	15 (9)	75.0 ± 11.8	4.1 ± 3.8	12.8 ± 5.0
AD1 + AD2	35 (20)	74.9 ± 8.9	4.8 ± 3.4	16.4 ± 6.0

EEG acquisition

Twenty-channel EEG signals were acquired with the participants awake, relaxed, and with their eyes closed for at least eight minutes. EEG was recorded with 12-bit resolution and 200 Hz sampling frequency using Braintech 3.0 instrumentation (EMSA Equipamentos Médicos INC., Brazil). Scalp electrodes were placed according to the International 10-20 montage system in the locations depicted in Figure 4.1; electrode impedance was kept below 10 kΩ, and bi-auricular (attached) electrodes were used as reference.

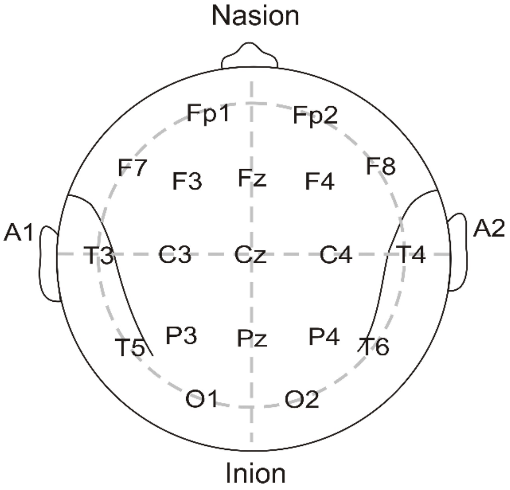

Figure 4.1 – EEG electrode placement for Brazil AD dataset, 20 channels.

Moreover, based on evidence of an inter-hemispheric disconnection with AD [17, 76, 36, 75, 179], we also explored the use of virtual inter-hemispheric bipolar signals, which are the electric potential difference measured between a pair of electrodes symmetrically located in each hemisphere. The term "virtual" is used because these signals are mathematically computed as the subtraction of the two recorded unipolar signals involved [1]. The eight bipolar signals used in this work were the inter-hemispheric signals Fp1-Fp2, F7-F8, F3-F4, T3-T4, C3-C4, T5-T6, P3-P4 and O1-O2.

4.3.2 EEG pre-processing

EEG recordings were filtered with a zero-phase FIR bandpass filter with a bandwidth 0.5-45 Hz. Signals without any additional processing constituted what is referred to as the "raw" EEG dataset. The enhanced EEG signals, in turn, were the raw signals processed by the different AAH algorithms described in the next subsection. Lastly, the raw signals also were visually inspected by two experienced clinicians to obtain several eight-second epochs free of eye blinking, drowsiness, muscle movements, or equipment-related artifacts. This manually selected data was used to obtain a gold-standard system with which the impact of the use of raw and enhanced EEG was benchmarked against.

4.3.3 Automated artifact handling algorithms

Three automated handling approaches were explored within this work: statistical artifact rejection, automated artifact removal based on BSS and wavelet-enhanced ICA. They were chosen based on characteristics of our dataset; more specifically, on the electrode layout (international 10–20 system), number of electrodes (20), absence of EOG signals, and lack of data from alternative modalities (e.g., accelerometers or gyroscopes). In the subsections to follow, a brief summary of the three approaches and a description of their implementations are provided below.

Statistical artifact rejection approach

The statistical artifact rejection (SAR) is an automated method for artifact rejection that utilizes thresholds on the statistical characteristics of the EEG signals to identify epochs that appear to contain artifacts. The implementation of this method was done using the well-known EEGLAB toolbox [180]. The criteria used to reject epochs included: extreme values caused by gross artifacts and amplifier saturation, i.e., greater than $+/- 100\ \mu$V, abnormally distributed data, i.e., 5 standard deviations from average kurtosis, suggesting peaky or flat distributions and "improbable data" computed with an online probability-of-occurrence metric. More details on the SAR method can be found in [141].

Automated blind source separation approach

Through the use of BSS methods, presented in Section 2.6.2, it is possible to decompose the EEG signal into different components and then reconstruct the signal based only on the non-artifactual components, which have been found via a suitable automatic criterion. Here, we explored a cascade configuration made up of two automated BSS (aBSS) approaches, based in SOBI and CCA, developed to separate and automatically identify ocular and muscular artifacts respectively. In the SOBI-based method, second order statistics are used to find components that have nonzero time-delayed autocorrelations and zero time-delayed cross-correlations. Such an approach has been shown to preserve more brain activity compared to other ocular artifact removal methods [181]. In our implementation, the fractal-dimension criterion was used to identify components related to the ocular artifacts, with the premise these components possess lower fractal dimension compared with components related to neural activity, as presented in [77]. In the CCA-based method, EEG data is expressed as a combination of maximally autocorrelated and mutually uncorrelated components, thus components with the lowest autocorrelation values are assumed to be related to muscular artifacts, as muscular activity has been shown to be of wider bandwidth than EEG, and thus have properties similar to white noise [139]. The widely utilized AAR plugin[1] for EEGLAB was used in our experiments to implement the SOBI and CCA methods with the following default parameters: for automated SOBI-based removal, *eigenratio* $= 10^6$, *range* $=$ 2-4, and the *no-EOG reference* option selected; for the CCA-based removal, *emg-psd-ratio* $=$ 10, and *femg* $=$ 15. In the context of this Chapter, the “BSS approach” refers to the use of the automated SOBI method to remove ocular artifacts followed by the automated CCA method to remove muscular-related artifacts.

Wavelet-enhanced ICA approach

The wavelet approach has been used successfully in EEG for the analysis or ERPs [13] and detection of events such as epileptic seizures [59], and it has recently been combined with ICA to perform automated artifact removal. The so-called wavelet enhanced ICA (wICA) approach [140]

---

[1] `https://germangh.github.io/eeglab_plugin_aar/`

applies a thresholding step on the wavelet transform of the obtained independent components (IC) in an attempt to recover any residual neural activity that may be present in components labeled as artifactual. The wICA method operates in five steps: (*i*) the EEG data is decomposed into ICs, (*ii*) the discrete wavelet transform is applied to each IC, (*iii*) thresholding of the wavelet coefficients is performed to differentiate between neural and artifactual coefficients, (*iv*) the inverse wavelet transform is applied to the thresholded coefficients, retrieving with only neural activity in the IC and lastly, (*v*) IC corrected in the wavelet-domain are projected to obtain the enhanced version of the EEG data. A complete description, as well as a comparative analysis between ICA and wICA, is provided in [140]. In our experiments, the wICA toolbox[2] was used with the following parameters: *cleaning artifact tolerance* = 1.25 and an *IC artifact detection threshold* = 4.

Algorithm combination

In these experiments, we have tested the three above-mentioned automated algorithms alone, as well as in a cascade configuration, more specifically, we tested the SAR+aBSS and SAR+wICA combinations. Thus a total of seven EEG datasets are defined: raw, SAR, aBSS, wICA, SAR+aBSS, SAR+wICA and manually selected; Figure 4.2 presents the pipeline for the computation of such datasets. Overall, the experimental results obtained with the automated algorithms and their combinations (i.e., SAR, aBSS, wICA, SAR+aBSS, SAR+wICA) are compared with the performance obtained with the "raw" EEG data, which represents the "baseline" performance, and the performance obtained with a system based on manually selected EEG data, this system is referred to as the "gold-standard".

---

[2] `http://www.mat.ucm.es/~vmakarov/downloads.php`

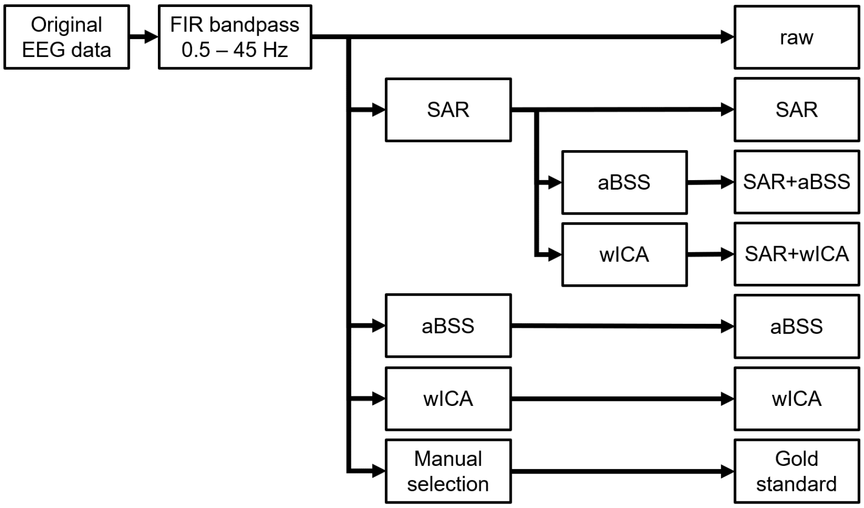

Figure 4.2 – Processing pipeline used for the computation of AAH datasets.

4.3.4 Feature extraction

Several EEG features have been proposed in the literature over the last decade and shown to accurately discriminate between healthy controls and AD patients as described in Section 2.7. However the effects of EEG artifacts on these features are unknown, as well as their effects on overall AD diagnosis performance. Here, we focused on three commonly used EEG feature categories, namely, spectral power, coherence, and the recently-proposed AM rate-of-change. The description of these features can be found in Sections 2.7.1.1, 2.7.2.1 and 2.7.4.1 respectively. Once the raw, manually selected, enhanced EEG datasets were computed, the eight proposed bipolar signals (Fp1-Fp2, F7-F8, F3-F4, T3-T4, C3-C4, T5-T6, P3-P4, and O1-O2) were computed, and each of the 28 available channels was split into 8-second epochs with a 1-second epoch shift.

As for the spectral features, we compute the relative band power for the five classic EEG bands for each of the 28 EEG signals (20 electrodes + 8 virtual bipolar signals). The band power was computed as the power of an individual band normalized by the fullband EEG power. A total of 140 (28 × 5) spectral-based features were computed per epoch. Coherence features consisted in MSC and phase coherence; both metrics were computed for each of the five classic EEG bands. Following the evidence of a reduced inter-hemispheric connectivity with AD [17, 75], coherence features were computed for each classic EEG band for the eight inter-hemispheric electrode pairs; thus a total of

40 MSC features and 40 phase coherence features were obtained. The AM rate-of-change features were computed for all the *band-mband* combinations based on the five classic EEG bands; however not all these combinations make sense, as highlighted in Section 2.7.4.1. As such, only 14 AM rate-of-change features were considered for each channel. Finally, Table 4.2 presents a list of the computed features.

Table 4.2 – Computed features for each 8-s epoch.

Feature group	**Features**
Spectral	delta
(Computed for each of the 28 channels)	theta
	alpha
	beta
	gamma
Magnitude square coherence	delta_msc
(Computed for each of the 8 inter-hemispheric pairs)	theta_msc
	alpha_msc
	beta_msc
	gamma_msc
Phase coherence	delta_pha
(Computed for each of the 8 inter-hemispheric pairs)	theta_pha
	alpha_pha
	beta_pha
	gamma_pha
Amplitude modulation rate-of-change	delta-mdelta
(Computed for each of the 28 channels)	theta-mdelta
	theta-mtheta
	alpha-mdelta
	alpha-mtheta
	beta-mdelta
	beta-mtheta
	beta-malpha
	beta-mbeta
	gamma-mdelta
	gamma-mtheta
	gamma-malpha
	gamma-mbeta
	gamma-mgamma

Computed features were grouped into four feature sets: PSD (spectral features), MOD (amplitude modulation rate-of-change features), MSC (magnitude square coherence), and PHA (phase coherence). To explore the complementarity of the extracted features, combined feature sets were also investigated. As such the "ALL" feature set contained all the extracted features and the "PSD+MOD" set was a combination of PSD and MOD feature sets; this latter was motivated by the recent results suggesting the complementarity of the two feature domains for AD characterization [71].

Lastly, an additional method to improve the signal-to-noise ratio (SNR) of the extracted features was used, that is to say, the sliding average (over five epochs) in the feature domain. This procedure was recently shown to improve the clustering of AM rate-of-change features, thus leading to higher diagnostic accuracies [76]. This procedure is akin to the epoch averaging step commonly performed in ERP studies [13], though it differs in the sense that it is performed in the feature domain; as such, it can be seen as a lowpass filter on the (non-linear) feature domain.

4.3.5 Feature selection and classification

The machine learning and pattern recognition literature has presented a plethora of possible feature selection and classification algorithms, which can be fine-tuned to specific applications and feature sets. The goal of the experiments presented herein was to understand the effects of artifacts and automated artifact handling algorithms on different EEG feature sets and consequently on diagnostic performance, and not the effects of different feature selection and classification algorithms. As such, we used a SVM feature selection and classification algorithm that is widely used in the EEG-based AD diagnosis literature (see Section 2.8.3 and [74, 75, 36, 76]). The principle behind the SVM algorithm as classifier is to map data points into a higher dimension in which the data points can be separable by a hyperplane. The open-source software Weka[3] was used for SVM-based attribute evaluation to rank the features and the classifier based on SVM with polynomial kernel, regularization coefficient C = 1, and hyperplane shaping coefficient $\gamma = 0.01$. A description of the SVM-based feature selection and classification algorithms is beyond the scope of this thesis, the interested reader is referred to [182, 159]. Accuracy values reported were computed epoch-wise.

---

[3] `https://www.cs.waikato.ac.nz/ml/weka/`

In our experiments, a contiguous 25% of the available data for each participant was randomly set aside for feature selection and the disjoint remaining 75% was used to train and test the classifier using 10-fold CV. Using disjoint sets for feature selection and classifier training reduces any unwanted biases in the reported performance figures. To remain in line with previous EEG-based AD diagnostic literature [36, 76], feature selection was used to identify the 24 most relevant features for AD diagnosis.

We evaluate the AD diagnosis performance for each of the combinations of the seven artifact handling methods and the six feature sets proposed. The effects of automated artifact handling on AD diagnostic performance were tested under three classification tasks, namely, Task 1: Nold vs. AD1 vs. AD2, Task 2: Nold vs. AD1 and, Task 3: AD1 vs. AD2. The first task explored the more challenging 3-class problem discriminating between healthy aging and two stages of AD. The second, in turn, explored the discrimination performance in the scenario of early detection. Lastly, the third task assessed the EEG-based disease progression monitoring scenario.

For comparison purposes, the so-called “gold-standard” system was used to benchmark the results and was obtained by using the ALL feature set derived from the manually selected EEG dataset and the 5-epoch feature averaging. In Task 1, the gold-standard setup achieved an accuracy of 83.8%. For Task 2 and Task 3, in turn, accuracies of 93.2% and 92.8% were obtained respectively. The classification performances for the combination of automated artifact handling methods and feature sets are presented in Section 4.4.

4.4 Results

In all experiments, the use of feature averaging over 5-epochs, presented in [76], improved the classification performance, as such the results presented in this section all assume feature averaging. Tables 4.3, 4.4 and 4.5 report the accuracy achieved with the baseline system in the top row, followed by ones obtained with the different AAH algorithms for the four feature sets and two combined feature sets (i.e., ALL and PSD+MOD) for Task 1, Task 2 and Task 3 respectively. A careful analysis of the presented Tables suggested that for all three tasks, the wICA algorithm combined with the top-24 features selected from the ALL feature set resulted in the best classification performance. Tables 4.6 and 4.7 show the top-24 features for each of the three tasks, for the gold-standard and the wICA-All system respectively. Feature names are reported as "electrode_feature" where "electrode" represents either the 10-20 electrode positions (e.g., Pz) or the virtual bipolar signal (e.g., P3-P4) and "feature" provides a descriptive indication of the feature as presented in Table 4.2.

Table 4.3 – Accuracy for baseline and AAH-enhanced EEG datasets for each feature set, evaluated under Task 1: N vs. $AD1$ vs. $AD2$. The bold figure indicates the best performance.

	Feature Sets					
	PSD	MOD	MSC	PHA	ALL	PSD+MOD
Baseline	73.2	68.4	60.1	45.7	72.3	73.5
Automated artifact handling algorithms						
SAR	74.1	66.0	60.3	46.5	74.1	72.9
SAR+aBSS	69.1	61.8	56.6	40.7	71.6	70.9
SAR+wICA	72.6	66.4	65.1	46.9	75.7	75.4
aBSS	70.3	65.4	56.4	40.7	67.8	68.5
wICA	75.7	70.5	68.0	48.3	**78.9**	76.5

Table 4.4 – Accuracy for baseline and AAH-enhanced EEG datasets for each feature set, evaluated under Task 2: N vs. $AD1$. The bold figure indicates the best performance.

	Feature Sets					
	PSD	MOD	MSC	PHA	ALL	PSD+MOD
Baseline	83.6	79.6	73.3	64.9	83	82.6
Automated artifact handling algorithms						
SAR	83.4	82.4	75.4	67.4	84.8	84.7
SAR+aBSS	81.9	77.4	73.1	63.4	81.1	82.1
SAR+wICA	87.4	78.1	74.7	64.0	86.9	85.6
aBSS	80.0	74.9	71.8	62.0	79.8	81.1
wICA	89.7	82.2	74.0	67.9	**90.8**	89.4

Table 4.5 – Accuracy for baseline and AAH-enhanced EEG datasets for each feature set, evaluated under Task 3: $AD1$ vs. $AD2$. The bold figure indicates the best performance.

	Feature Sets					
	PSD	MOD	MSC	PHA	ALL	PSD+MOD
Baseline	89.4	85.1	78.5	69.4	89.2	88.6
Automated artifact handling algorithms						
SAR	92.2	86.4	77.4	71.2	91.2	91.0
SAR+aBSS	86.0	80.4	76.4	67.5	88.5	86.7
SAR+wICA	90.2	85.1	82.0	70.9	92.2	92.2
aBSS	84.9	79.2	76.9	66.2	82.5	85.3
wICA	91.3	88.4	86.5	73.0	**96.3**	92.9

Table 4.6 – Selected features used with the gold standard systems. The last four sections show, from top to bottom, the number of features that belong to each of the four feature sets, brain regions, frequency band, and montage, respectively.

Ranking	Tasks		
	N vs $AD1$ vs $AD2$	N vs $AD1$	$AD1$ vs. $AD2$
1	O1-O2_theta	O1-O2_theta	Cz_beta
2	P3-P4_theta	Pz_delta	P4_alpha-mtheta
3	T5_theta-mtheta	Cz_beta-mtheta	P3-P4_delta
4	F7-F8_alpha_pha	Fp2_beta	F7_alpha-mdelta
5	T3_theta-mdelta	Fp1_beta-mbeta	O1-O2_theta_pha
6	P3-P4_delta	O1-O2_alpha	T3_theta
7	Pz_alpha	O1-O2_beta_pha	Oz_beta-malpha
8	O1-O2_alpha	F7-F8_alpha_pha	P3-P4_theta-mtheta
9	C4_alpha-mdelta	T6_delta-mdelta	P3-P4_beta-malpha
10	Fp2_beta	Fp1_delta	O1-O2_theta-mtheta
11	T3-T4_alpha-mtheta	Oz_beta-mbeta	T4_theta
12	T5-T6_beta-mdelta	O1-O2_beta-mtheta	T6_theta-mtheta
13	T6_beta-mdelta	T3-T4_beta-malpha	P3-P4_beta-mbeta
14	T4_theta	F7-F8_beta-mbeta	C3-C4_alpha_msc
15	O1-O2_alpha-mtheta	Pz_alpha	P3-P4_beta
16	O1_delta	Oz_beta	P3-P4_theta-mdelta
17	P3-P4_beta-mtheta	C4_delta-mdelta	T5-T6_alpha_msc
18	T3_theta	Cz_beta-malpha	F7-F8_alpha_msc
19	Oz_beta	F4_theta-mdelta	P4_beta-mbeta
20	F3-F4_theta	F3-F4_delta_msc	T5-T6_delta_msc
21	T6_delta_pwr	Fp1-Fp2_beta_msc	T3-T4_theta_msc
22	C4_delta-mdelta	P3-P4_delta_msc	Fp1_theta-mdelta
23	T3-T4_beta-mbeta	T5_beta	T3_theta-mdelta
24	Pz_delta	Fz_delta	C3-C4_delta_pha
NUMBER OF FEATURES PER FEATURE SET			
PSD	13	9	5
MOD	10	10	12
MSC	0	3	5
PHA	1	2	2
NUMBER OF FEATURES PER BRAIN REGION			
frontal	3	9	3
central	2	3	3
temporal	9	3	7
parietal	5	3	8
occipital	5	6	3
NUMBER OF FEATURES PER FREQUENCY BAND			
delta	5	7	3
theta	7	2	10
alpha	6	3	5
beta	6	12	6
NUMBER OF FEATURES FROM VIRTUAL CHANNELS			
inter-hemispheric	11	10	14

Table 4.7 – Selected features used with the wICA-ALL automated system. The last four sections show, from top to bottom, the number of features that belong to each of the four feature sets, brain regions, frequency band, and montage, respectively. Features with an asterisk represent those with a distribution overlap pre- and post-wICA $\geq$ 80%. Values reported between parentheses represent those with pre- and post-wICA distribution overlap $\geq$ 80%.

	Tasks		
Ranking	N vs $AD1$ vs $AD2$	N vs $AD1$	$AD1$ vs. $AD2$
1	Pz_alpha*	Pz_alpha*	P3-P4_delta
2	C3-C4_delta	P3_alpha*	O1-O2_theta_pha
3	P3-P4_delta	O1-O2_theta*	C3_alpha
4	P3_alpha*	T3-T4_delta	F4_delta
5	P3-P4_delta-mdelta	F7_delta	T4_delta
6	Fp1-Fp2_beta_msc*	C3-C4_beta-mbeta	T3-T4_beta*
7	P3-P4_delta_msc*	F3_delta	T5_beta*
8	T3-T4_delta	O1-O2_delta-mdelta	Oz_beta
9	P3_delta	O1-O2_beta_msc*	Fp1-Fp2_beta_msc*
10	O1_alpha*	Fp1-Fp2_delta_msc*	Fz_beta-malpha
11	T4_theta*	Fp1_delta	F3_beta-mbeta
12	T3_delta	T3_delta-mdelta	T5_theta*
13	T5_beta*	C3_delta-mdelta	T3_alpha*
14	O1-O2_theta*	P4_alpha*	T5-T6_delta_msc*
15	F8_beta	O1_alpha*	C4_delta
16	Cz_beta	T5_beta*	C3-C4_delta_msc*
17	T4_theta-mtheta*	Cz_beta	O1-O2_beta-mtheta
18	C3-C4_beta-mbeta	F8_beta	P3-P4_delta-mdelta
19	F7_beta	T3-T4_beta-malpha	F3-F4_beta-mbeta
20	C3_beta	T3-T4_beta_msc*	T3-T4_delta_msc*
21	F3_delta	F7-F8_beta_msc*	P4_beta-malpha
22	Oz_delta	Fz_beta-malpha	F3-F4_alpha
23	Fz_beta-malpha	T5-T6_theta*	Fp1_theta*
24	C3_alpha*	F3_alpha*	O1_alpha
NUMBER OF FEATURES PER FEATURE SET			
PSD	18(7)	14(8)	13(5)
MOD	4(1)	6(0)	6(0)
MSC	2(2)	4(4)	4(4)
PHA	0(0)	0(0)	1(0)
NUMBER OF FEATURES PER BRAIN REGION			
frontal	5(1)	8(3)	7(2)
central	5(1)	3(0)	3(1)
temporal	5(3)	6(3)	7(6)
parietal	6(3)	3(3)	3(0)
occipital	3(2)	4(3)	4(0)
NUMBER OF FEATURES PER FREQUENCY BAND			
delta	9(1)	8(1)	8(3)
theta	3(3)	2(1)	3(2)
alpha	4(4)	5(5)	4(1)
beta	8(2)	9(4)	9(3)
NUMBER OF FEATURES FROM VIRTUAL CHANNELS			
inter-hemispheric	8(3)	9(6)	11(5)

4.5 Discussion

4.5.1 Automated artifact handling

The three AAH algorithms explored here represented the state-of-the-art applicable to the constraints imposed by our available dataset (fully described in Section 4.3.1), such as the number of channels (20 electrodes) and lack of EOG reference channels. For studies without these limitations, alternative AAH algorithms can be explored. For example, for studies involving EEG with over 64 channels and EOG channels, the automatic EEG artifact detection based on the joint use of spatial and temporal features (ADJUST) [145] and the fully automated statistical thresholding for EEG artifact rejection (FASTER) [146] algorithms can be used. On our 20-channel dataset, we found the use of these two algorithms to lead to over-rejection of components deemed artifactual, thus negatively impacting diagnostic performance. Lastly, if auxiliary signals are recorded simultaneously with EEG data, other algorithms may be used. Representative examples include the use of EOG or signals from optical eye tracking systems to develop adaptive filtering schemes [183, 184], or even the use of gyroscopes in ambulatory EEG systems to flag EEG segments collected during head movements [185].

From Tables 4.3, 4.4 and 4.5, it can be seen that the wICA algorithm combined with classifiers trained on the top-24 features found from the ALL features set resulted in the best classification performance. For the three-class task, such an automated system resulted in a classification accuracy of 78.9%, which was significantly higher than chance, and in line with what was achieved with the gold standard (i.e., 83.8%). For Task 2, in turn, the accuracy obtained was 90.8%; this also compared favorably with the gold-standard performance, which was 93.2%. Interestingly, for Task 3 involving AD1 and AD2 participants, the wICA-based system outperformed the gold-standard, achieving an accuracy of 96.3%; the gold-standard, in turn, achieved a 92.8% accuracy. It is suspected that this improved performance was obtained due to information harnessed from the frontal electrodes, which were often selected by the wICA-processed data, and not from the manually-selected data. Frontal electrodes are susceptible to eye-related artifacts and are likely often discarded by human experts. Notwithstanding, the frontal region has been shown in classical studies to be severely affected by AD progression [186]. These findings show the relevance of an automated system in assisting clinicians with diagnosis. Moreover, from Tables 4.3, 4.4 and 4.5 it can be seen that the aBSS algorithm and its combination with SAR resulted in performance decreases relative to the baseline system trained on raw data for all tested feature sets and tasks. This suggests that while aBSS can be used to reliably remove ocular artifacts [77], its processing also removes important information to discriminated AD from the raw EEG data.

4.5.2 Salient features

The lists of top-selected features presented in Tables 4.6 and 4.7 show that power spectral and AM rate-of-change features are the most salient; combined they represented 96%, 79%, and 70% of the top-24 features for Tasks 1, 2 and 3 in the gold-standard system, and 92%, 83%, and 79% of the top-24 features in Tasks 1, 2 and 3 for the wICA-ALL system. It is interesting to remark that the ratio of the picked AM rate-of-change and spectral features was reduced from the gold-standard systems (Table 4.6) to the wICA-based systems (Table 4.7), suggesting that wICA enhancement had a detrimental effect on the AM rate-of-change features. Phase coherence features, in turn, were seldom selected in both the gold-standard and wICA-based systems, suggesting they play a small role in EEG-based AD diagnosis. When discriminating between the three classes (Task 1), features from the temporal and parietal regions showed to be important across the two scenarios. For the Nold vs. AD1 task, in turn, frontal and temporal regions stood out. For Task 3, features from the temporal and parietal regions stood out for the gold-standard whereas features from the temporal and frontal regions were most salient for the wICA-based system. Frontal region data may be corrupted by eye blinks, thus are likely rejected by human experts. By automatically removing artifacts from EEG data, useful discriminatory information may remain in such electrodes, thus assisting in AD diagnosis.

As for frequency bands, in the gold-standard systems, delta, theta and beta features were most prevalent, amounting to about 80% of the selected features. Theta band features were particularly useful for Task 3, a finding previously reported in the AD severity monitoring literature [187]. In the wICA-based systems, delta and beta band features corresponded to roughly 70% of the selected features for each of the three tasks, followed by alpha band features (15%), thus corroborating previous studies that show the slowing of the EEG with AD (Section 2.7.1). It is important to emphasize that none of the features extracted from the gamma bands were selected. It is hypothesized that this may be due to the fact that such higher frequencies are most sensitive to EEG artifacts, thus are (*i*) often discarded by human experts and (*ii*) may be severely distorted by the enhancement algorithms to a point of removing any existing discriminatory information. Lastly, it was observed that of the top-24 selected features, roughly 40% corresponded to information extracted from inter-hemispheric (virtual bipolar) signals, thus corroborating evidence of an inter-hemispheric disconnection with AD [17, 36, 75].

In order to characterize the effects of the wICA algorithm on the individual distribution of the salient features, for each of the top-24 features in Tables 4.6 and 4.7 we computed their distribution and compared them by calculating the overlap percentage between distributions. This metric was normalized to lie between $0 - 100\%$, with 0 and 100% overlap values suggesting complete change and no change in feature statistics between before and after enhancing respectively. Table 4.7 highlights features that resulted in an overlap greater than 80%, thus can be considered as irrelevant statistical changes. Moreover, coherence features were found to be the least affected by wICA, whereas the AM rate-of-change ones were most affected. For Tasks 1 and 2, alpha and theta bands features were least affected; however, features from such frequency bands only correspond to roughly 30% of the top-24 selected features. Interestingly, features from such bands correspond to 55% and 63% of the features in the gold-standard for Tasks 1 and 3, respectively (see Table 4.6), thus suggesting their robustness to artifacts.

4.5.3 Further exploration on classification type

Once the diagnosis performance was analyzed for all combinations of AAH algorithms and feature sets, we found that the wICA algorithm outperformed all other methods. In Section 2.8.2, we highlighted that the 10-fold CV method used is prone to optimistic biases, as it is likely that data used for training and testing are not disjoint. To avoid this situation we evaluated the Nold vs. AD classification task under LOSO CV. Moreover, we explored the potential benefits of using an informative classification approach, described in Section 2.8.3, by using the RVM classifier. The RVM method uses a probabilistic Bayesian learning framework to find classifiers that have (*i*) fewer basis functions than a comparable SVM and (*ii*) the benefit of explicitly predicting the probability of class membership, thus providing clinicians with a richer pool of information [78].

EEG signals where enhanced with wICA, and features described in Table 4.2 were computed. In LOCO CV, classification still is performed epoch-wise, but the accuracy is subject-wise reported. With this approach and the SVM classifier, a subject is labeled as Nold or AD based on majority vote, i.e., if 50% or more of the epochs are labeled as a given class, thus placing equal weight on all classified epochs. With the RVM, on the other hand, the probabilistic output of each epoch can be used to perform a better-informed majority vote fusion, i.e., majority vote can be performed taking into account only epochs that possess a class membership larger than a threshold X%. In this sense, we explored the effects of membership threshold on the overall diagnostic accuracy. In our experiments, the open-source MATLAB Pattern Recognition Toolbox[4] was used for training the SVM and RVM classifiers. We decided to use MATLAB instead of Weka for two reasons: (*i*) Weka does not provide an implementation of RVM, and (*ii*) to standardize the SVM and RVM machine learning pipelines. Polynomial kernels were used for both classifiers with a regularization coefficient C=1 and and hyperplane shaping coefficient γ=0.01.

Figure 4.3 shows the performance metrics (accuracy, sensitivity and specificity) obtained for the RVM-based system as a function of the class membership threshold. As can be seen, these metrics are collectively optimized for a threshold between 70-75%, after which point the performances monotonically decrease. As such, we use the 75% threshold in the proposed RVM system, i.e., epochs with a class membership below 75% for Nold or AD classes are discarded for the subject pooling. To get a sense of the distribution of EEG epochs that achieved such high class membership probability, Figure 4.4 shows which of the over 300 epochs, per participant, were above (non-shaded) or below (shaded) 75% class probability. As can be seen, the majority of the epochs were classified with high reliability. An example of participants that had the majority of their epochs classified with 75% is participant #2 (indicated in the green box in Figure 4.4); on the other hand, participants such as participant #20 (indicated in the red box in Figure 4.4) had the majority of their epochs classified with less than 75% class membership probability. As can be seen, the RVM classifier provides a richer pool of data for clinicians to use in their assessment relative to SVM systems.

---

[4] `https://github.com/covartech/PRT`

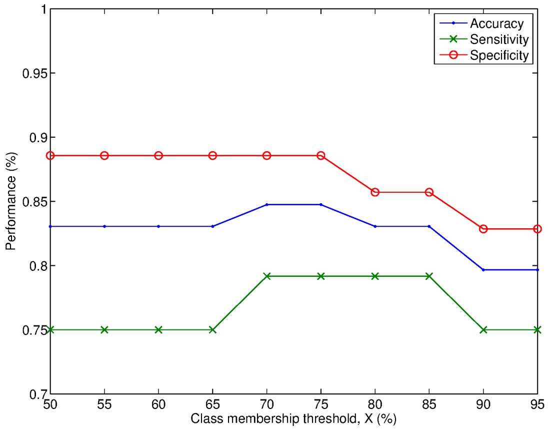

Figure 4.3 – RVM performance as a function of class membership threshold.

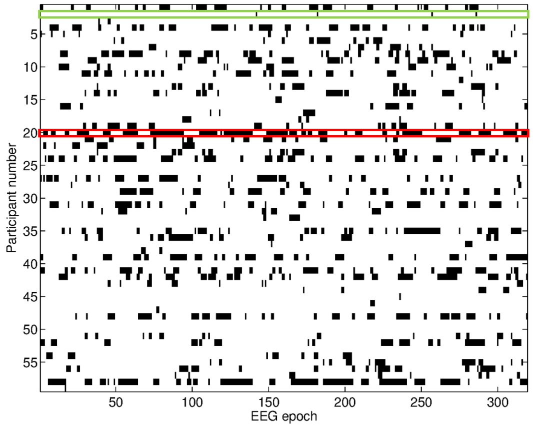

Figure 4.4 – Distribution plot of per-participant epochs classified as having more (unshaded) or less (shaded) than 75% class membership.

Table 4.8 summarizes the performance comparison obtained with the gold-standard benchmark system (manual selected EEG and "ALL" feature set), as well as with the fully-automated SVM- and RVM-based systems, both based on the wICA and "ALL" feature sets. As can be seen, the RVM based system outperforms the SVM-based one across all three performance metrics. Relative to the benchmark system, the proposed RVM system achieved equal accuracy and improved sensitivity, with the advantage of not requiring human intervention. The benchmark system only slightly outperformed the fully-automated tools in terms of specificity, achieving 3% higher performance relative to RVM.

Table 4.8 – Performance comparison of semi-automated benchmark and fully-automated AD diagnostic systems.

System	Accuracy (%)	Sensitivity (%)	Specificity (%)
Benchmark	84.7	75.0	91.4
SVM	81.4	75.0	85.7
RVM	84.7	79.2	88.6

4.6 Conclusions

The last decade has seen a rise in the development of EEG-based tools to assist clinicians with AD diagnosis. The experiments presented in this chapter evaluated the effects of different AAH algorithms on diagnosis performance; the algorithms were tested both alone and in cascade. Experimental results showed the wICA algorithm outperformed the other algorithms across the six investigated feature sets. Overall the performance of the fully-automated systems was in line with the performance obtained with systems based on "artifact-free" EEG data manually selected by human experts. Such findings suggest that human intervention and the discard of useful discriminatory information can be avoided by using automated artifact removal algorithms. Ultimately, it is hoped that such fully-automated diagnostic tools be used to assist clinicians not only with early diagnostics, but also with disease progression monitoring and assessment. Further exploration concerning classification type showed that the use of informative classification can further improve the performance of AD diagnosis system, by performing better-informed classification. Moreover, it can provide a richer pool of information to clinicians, enabling more accurate and earlier Alzheimer's disease assessment, as well as disease progression monitoring.

Chapter 5

Towards Portability: Effects of Low-Density EEG on AD Diagnosis

5.1 Preamble

This chapter is compiled from material extracted from the manuscripts published in *Biomedical Signal Processing and Control* [116].

5.2 Introduction

The miniaturization and affordability of sensors and circuitry has led to the development of portable devices for health monitoring. More specifically, in the area of EEG, this has opened doors to the possibility of performing EEG data acquisition and processing in places other than the typically clinic environment [79]. Such portable devices present interesting advantages compared with their research-grade counterparts, such as: (*i*) reduced hardware-related stress during EEG setup and thus reduced discomfort during recordings, allowing longer recordings in more natural positions or circumstances, such as book reading or TV watching, (*ii*) since wiring is eliminated, transportation of these devices is facilitated, and given their ubiquitous data transmission technologies (e.g., Bluetooth, Wi-Fi or Zigbee), recording and processing of EEG signals on mobile devices has become a reality, and lastly, (*iii*) the lower power consumption requirements have allowed for long-term recordings while subjects are performing their daily activities, thus making ambulatory EEG practical. Reviews on portable EEG devices are presented in [21, 22, 79]. In EEG-based AD research, most of published works have used layouts with 16 or more electrodes as presented in Section 2.5.3. The use of a high number of electrodes for the study of rsEEG is based on the better spatial sampling obtained that can bring better insights of the processes inside the brain; moreover, the use of a large number of electrodes is a requirement for certain EEG features, such as the features based on source localization (Section 2.6.4). In 2015, Neuronetrix, an USA-based company, reported the outcomes from clinical trials to validate the use of ERPs, acquired with a 7-channel EEG device, as markers for the study of AD. The auditory oddball ERP was used and, given its scalp localization, the use of more electrodes was not needed [80, 188].

In order to achieve low-cost automated rsEEG AD diagnosis, the use of low-density devices must be explored, as they will improve the portability and reduce the cost of the EEG devices, but most important, low-density devices present practical benefits in the clinical practice by reducing the setup time and stress related to the use of EEG devices on elderly participants both healthy or with AD [189, 38]. In this chapter, we present the exploration performed on the combination of portable EEG devices and the automated removal of artifacts (presented in Chapter 4) on the analysis of rsEEG for AD diagnosis, to evaluate the viability of portable low-cost EEG-based AD diagnosis.

5.3 Materials and methods

5.3.1 Neuronetrix AD dataset

Participants

Recently, Neuronetrix recruited participants over a 2-year clinical study across seven major Alzheimer's Disease Centres in the USA. The study was approved by institutional review boards for each site, and a written informed consent was obtained from each study participant [80]. One hundred eighty-four participants were divided into those suffering AD and healthy aging subjects. The AD group consisted of 99 participants who were diagnosed according to the NINCSD-ADRDA and DSM-IV criteria, and had a MMSE score between 21 and 26. The second group, Nold, was comprised of 85 healthy subjects matched for age and gender, with an MMSE score ≥ 27. Exclusion criteria were the use of antidepressants other than selective serotonin uptake inhibitors, major psychiatric disorders, and clinically significant neurologic disorders other than AD. Table 5.1 presents the demographics for the participants used in this study. Data from this study are referred to henceforth as the "Neuronetrix" AD dataset.

Table 5.1 – Demographics for the Neuronetrix AD dataset.

Group identifier	Subjects (female)	Age [years]	Education [years]	MMSE
Nold	99 (50)	76.3 ± 7.4	14.2 ± 3.1	29.1 ± 0.8
AD	85 (49)	72.9 ± 7.3	14.9 ± 3.0	23.1 ± 2.9

EEG acquisition

EEG data was acquired during a 15-30 minute auditory oddball ERP test followed by a 3-min resting-awake eyes-open period. As part of a collaboration, EEG data related to the resting-awake period was shared by Neuronetrix with the MuSAE Lab. The Neuronetrix proprietary 7-channel COGNISION™ device (Figure 5.1a) was used for data collection. The device uses a sampling frequency of 125 Hz and biauricular referential electrodes [190]. The electrode layout is presented in Figure 5.1b.

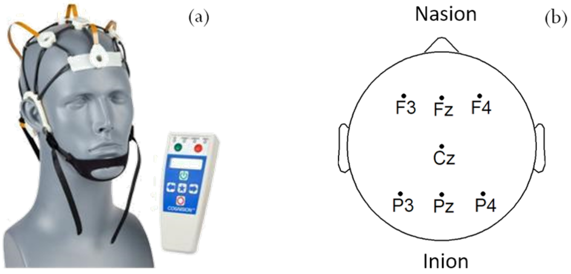

Figure 5.1 – (a) Neuronetrix proprietary COGNISION™ system. (b) EEG electrode placement for the Neuronetrix AD dataset.

5.3.2 Low-density version of the Brazil AD dataset

In order to compare results with the Neuronetrix dataset, the Brazil AD dataset (fully described in Section 4.3.1) was channel-wise decimated to have the same electrode layout as in the Neuronetrix dataset (Fig. 5.1b), and resampled from 200 Hz to 125 Hz. This dataset is henceforth referred as the “Brazil-ld” AD dataset.

5.3.3 Pre-processing and automated artifact removal

The signal pre-processing used for both 7-electrodes datasets was identical to the one described in Section 4.3.2. Moreover, motivated by the findings presented in Chapter 4, we made use of the wICA algorithm for automated artifact removal, with the following parameters, *cleaning artifact tolerance* = 1 and an *IC artifact detection threshold* = 4.

5.3.4 Feature extraction

Spectral power, coherence and AM rate-of-change features were computed as described in Section 4.3.4. Moreover, additional spectral features were computed in the bands low-alpha (8-10 Hz), high-alpha (10-12 Hz), delta-beta (0.5-30 Hz) and theta-beta (4-30 Hz); the separate computation of low- and high- alpha is a widely accepted procedure [18], and delta-beta and theta-beta were computed to assess the broadband effects of AD on rsEEG. Coherence features (MSC and phase coherence) were computed in the inter-hemispheric electrode pairs, and also for front-back pairs, i.e., F3-P3, Fz-Pz and F4-P4. EEG features were computed in 8-second epochs. Table 5.2 presents the list of the computed features.

5.3.5 Classification and statistical analysis

In the experiments presented in Chapter 4, 25% of the available data were set apart for feature selection. To be able to use the 100% of the available data for classification, a SVM classifier was used together with the l^1-norm as penalization, as this presents advantages with respect to the traditional l^2-norm. More specifically, the use of l^1-norm leads to sparse weight vectors; thus feature selection and classification are accomplished in the same step [81]. In our experiments, the open-source scikit-learn (machine learning for Python) [82] SVM implementation was used; the main reason to migrate our pipelines from MATLAB to Python is the Open Source[1] aspect of the latter, which becomes a pivotal aspect when working in teams, sharing code, and contributing to libraries.

---

[1] According to Open Source definition in `https://opensource.org/`

Table 5.2 – Computed features for each 8-s epoch.

Feature group	Features
Spectral (Computed for each of the 7 channels)	delta theta alpha low-alpha high-alpha beta delta-beta theta-beta gamma
Magnitude square coherence (Computed for each of the 5 pairs)	delta_msc theta_msc alpha_msc beta_msc gamma_msc
Phase coherence (Computed for each of the 5 pairs)	delta_pha theta_pha alpha_pha beta_pha gamma_pha
Amplitude modulation rate-of-change (Computed for each of the 7 channels)	delta-mdelta theta-mdelta theta-mtheta alpha-mdelta alpha-mtheta beta-mdelta beta-mtheta beta-malpha beta-mbeta gamma-mdelta gamma-mtheta gamma-malpha gamma-mbeta gamma-mgamma

The SVM classifier was used with the following parameters: linear kernel, l^1-norm penalization, and a default regularization coefficient value of C = 1. In order to evaluate the classifier performance, we computed the accuracy with two different approaches: epoch-wise using 10-fold CV and subject-wise with LOSO CV.

For comparison purposes, we use as benchmark the reported classification performance reported in Table 4.8, which were obtained with the full Brazil dataset, i.e., data from all 20 electrodes, wICA enhanced EEG, SVM classifier and LOSO CV approach. Lastly, to test if the features exhibited a statistically significant difference between the AD and control groups, a Kruskal-Wallis test with Dunn-Sidak post-hoc correction was used [83]. Statistical significance was established at a 1% level.

5.4 Results

Table 5.3 summarizes the classification performance (accuracy, sensitivity, and specificity) for the Benchmark and the different combinations of 7-channel datasets: Neuronetrix (resting-state eyes-open) and Brazil-ld (resting-state eyes-closed), using 10-fold and LOSO CV.

Table 5.3 – Performance comparison of the proposed system in Neuronetrix and Brazil datasets.

System	Accuracy (%)	Sensitivity (%)	Specificity (%)
Benchmark LOSO	81.4	75.0	85.7
Neuronetrix LOSO CV	63.1	68.7	56.5
Brazil-ld LOSO CV	69.5	71.4	66.6
Neuronetrix 10-fold CV	77.3	79.2	75.2
Brazil-ld 10-fold CV	91.4	92.9	89.2

Taking into consideration only the top-35 features for each dataset, Table 5.2 lists such features as well as highlights which are common between the two datasets. Features which exhibited a significant difference ($p < 0.01$) between the control and AD group are followed by an asterisk in the Table. Common features in both datasets are indicated with the symbols $\uparrow$ and $\downarrow$, which in turn indicated whether the median of the respective feature was higher or lower in the AD cohort, respectively.

Table 5.4 – List of the top-35 features from the systems. Features in bold are present in both columns. For common features, symbols ↑ and ↓ indicate whether the median of the feature was higher or lower in the AD cohort, respectively. Features followed by an * presented significant differences between control and AD cohorts; statistical Kruskal-Wallis test ($p < 0.01$) with Dunn-Sidak post-correction. The last two sections show the number of features that belong to each of the four feature sets and frequency bands.

Ranking	Datasets	
	Neuronetrix	Brazil
1	**Cz__alpha*↓**	**Cz__alpha*↓**
2	Cz__theta-beta*	**Pz__beta*↓**
3	**Fz__alpha*↓**	**Pz__theta*↑**
4	Fz-Pz__beta__msc*	Pz__delta*
5	**Pz__beta*↓**	**F3__gamma*↓**
6	**Pz__gamma*↑**	**P4__gamma*↓**
7	Cz__beta*	**P3__delta-beta*↑**
8	Fz__theta-beta	P4__alpha*
9	P3__low-alpha*	P4__beta*
10	Pz__alpha	**Cz__low-alpha*↑**
11	P3__high-alpha	P3__delta*
12	Pz__theta-beta*	**P3__beta*↓**
13	P3__alpha*	**Fz__alpha*↓**
14	Pz__low-alpha	**Pz__gamma↓**
15	F4__theta*	**P3__gamma*↓**
16	**P3__gamma↑**	Cz__high-alpha*
17	**F3__high-alpha*↓**	P3-P4__gamma__msc*
18	**F4-P4__beta__msc↓**	P4__low-alpha*
19	**F3__gamma↓**	P3__theta*
20	**F3-P3__theta__msc*↓**	**F3__beta*↓**
21	F3__low-alpha*	P4__delta-beta*
22	Cz__delta*	F4__beta*
23	Fz__gamma	Cz__delta-beta*
24	Fz__delta-beta	**Fz__high-alpha*↓**
25	**P3__delta-beta↓**	**P4__delta*↑**
26	**P3__beta*↓**	Fz__theta*
27	**Pz__high-alpha↓**	**F4-P4__beta__msc*↓**
28	**F3__beta*↓**	F4__gamma-malpha
29	**Cz__low-alpha*↓**	**P3-P4__theta__msc*↓**
30	**Pz__theta*↑**	P3-P4__alpha__msc*
31	**P4__gamma↑**	Cz__beta-malpha*
32	**P4__delta*↑**	Fz__beta-malpha*
33	F4__delta*	Fz-Pz__theta__msc*
34	Fz-Pz__gamma__msc*	Fz__low-alpha*
35	Fz__delta	**Fz__high-alpha*↓**
NUMBER OF FEATURES PER FEATURE SET		
PSD	31	27
MOD	0	3
MSC	4	5
PHA	0	0
NUMBER OF FEATURES PER FREQUENCY BAND		
delta	4	3
theta	3	5
alpha	11	13
beta	6	8
gamma	6	6

5.5 Discussion

5.5.1 Performance comparison

In Table 5.3 it is possible to appreciate that epoch-wise classification performance was higher when using 10-fold CV than when using LOSO CV. This is due to the fact that 10-fold CV introduces an optimistic bias in the estimation of the classifier performance as discussed in Section 2.8.2. As expected, the reduction in the number of electrodes, from 20 in the Benchmark system to 7 in the proposed system (i.e., Brazil-ld LOSO) led to a decrease in AD diagnosis performance in the Brazil dataset. In general, the performance of the Benchmark (20 electrodes) is considerably higher than the low-density setups; this could be attributed to the fact that a higher density layout presents a broader spatial distribution on the scalp; thus it can register cortical activity from other regions such as temporal and occipital lobes. In addition, a higher density coverage may be able to pick up spatially broad activities caused by deep brain structures, which are the first-affected by AD progression. The main difference between the explored datasets is the recording conditions, while both of them consisted of rsEEG, one is with eyes open (Neuronetrix) and the other (Brazil-ld) with eyes closed. To our understanding this is the first work reporting a thorough comparison between the two conditions within the context of rsEEG-based AD diagnosis. However, in general rsEEG in the eye-open condition is more prone to eye-movement related artifacts, and that may be a reason for the performance difference. Moreover, the somewhat higher results obtained on the Brazil dataset may be due to the fact that the AD and N groups were not education or age-balanced, as in the Neuronetrix dataset. Such factors have been shown to be important in AD progression [191].

5.5.2 Layout comparison

A limitation of the experiments presented in this chapter was the placement of the electrodes, which was set by the ones used in the Neuronetrix study, whose main goal was the evaluation of auditory ERPs in AD. In this sense, further exploration is needed towards the optimal low-density layout for the study of AD with rsEEG. The work presented in [75] explores the performance of different montages for rsEEG-based AD diagnosis, although in a 19-electrode setup.

5.5.3 Salient features

An in-depth analysis of the top-selected features, Table 5.2, shows that almost 50% (17 over 35) of these features are common for the Neuronetrix and Brazil datasets. In both datasets, it can be noted that the AD cohort presents decreased medians for power features corresponding to alpha and beta bands and increased medians for power features in delta and theta bands when compared with the Nold cohort. This shift in the power spectrum from high frequencies to low frequencies during AD is congruent with the slowing effects of AD in the EEG signals previously reported in the literature (Section 2.7.1). Nevertheless, in [84] is reported an increment in gamma band power for the AD cohort, while in [85] and [86] the opposite effect is observed. Such contradictory findings may have origin in the EEG recording conditions, which consisted of resting-awake eyes-open in [84] and resting-awake eyes-closed-eyes in [85] and [86]. The same behaviour was observed in our results where power features in gamma band presented: (*i*) an increment in the Neuronetrix dataset (resting-awake eyes-open condition) and (*ii*) a decrement in the Brazil-ld dataset (resting-awake eyes-closed condition), thus corroborating previous findings. For both datasets, the top feature was alpha power for the Cz electrode, which had a median value significantly lower in AD compared with the Nold, as per Figure 5.2. On the other hand, the opposite behaviour was observed in low frequency power features such as delta and theta, e.g., the median of the theta power for the electrode Pz was significantly higher in the AD cohort, as per Figure 5.3. While alpha power in Cz and theta power in Pz presented significant difference in both datasets, it is possible to appreciate (Figures 5.2 and 5.3) that only one feature does not have sufficient classification power to accurately discriminate the AD and N groups; thus a combination of features is needed.

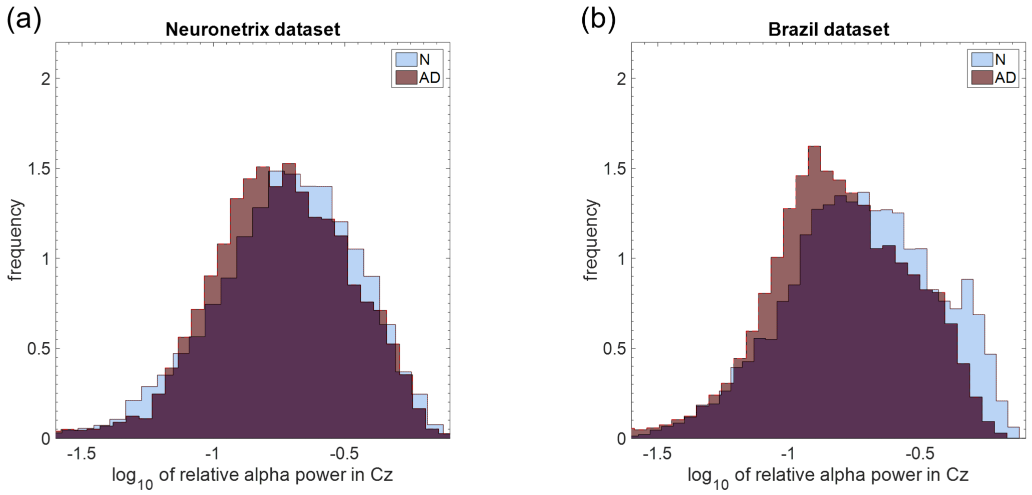

Figure 5.2 – Histograms for alpha relative power in electrode Cz. (a) Neuronetrix and (b) Brazil dataset.

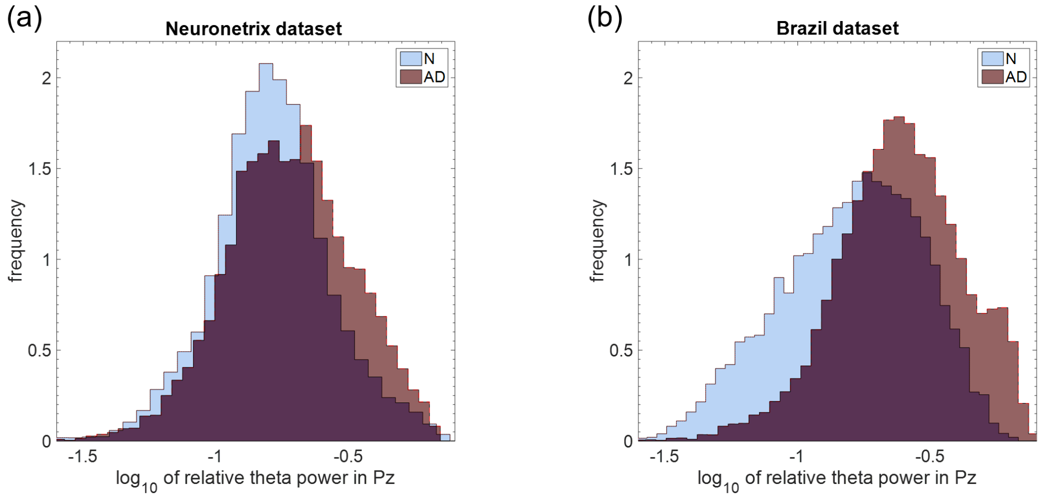

Figure 5.3 – Histograms for theta relative power in electrode Pz. (a) Neuronetrix and (b) Brazil dataset.

Interestingly, AM ratio-of-change features did not appear in the top-35 features for the Neuronetrix dataset. On the other hand, in the Brazil-ld dataset all amplitude modulation features were high frequency bands (beta and gamma) modulated by alpha rhythm. While amplitude modulation features are corrupted by wICA, they provide information that is not present in spectral features, helping to improve classification. Another reason for the low number of amplitude modulation features in the top-35 is that features where a higher frequency band (alpha, beta or gamma) is modulated by a slow frequency (delta or theta) present a high correlation with the power features of the higher band. Figure 5.4 shows the correlation between the power for alpha band in Cz (top feature in both datasets) and power of alpha-mdelta in Cz for the Neuronetrix (Figure 5.4a) and Brazil-ld (Figure 5.4b) datasets.

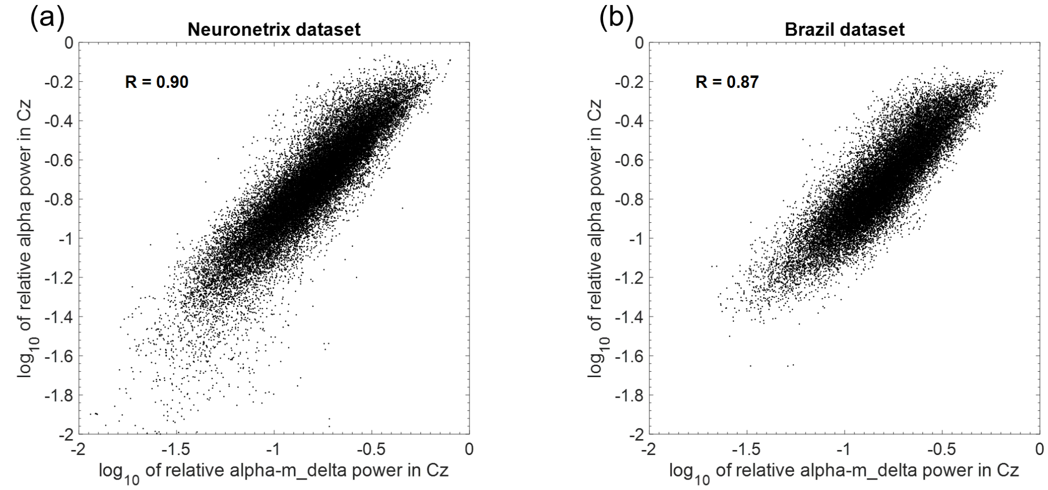

Figure 5.4 – Correlation between features: alpha relative power and alpha-mdelta relative power for electrode Cz. (a) Neuronetrix and (b) Brazil dataset.

The experiments presented in this chapter as well as the ones presented in Chapter 4 have relied on features that are defined by the well-defined frequency ranges of the classical EEG features, which may not be optimal for the EEG-based study of AD. As such Chapter 6 introduces new features based on the entire modulation representation of the EEG signals.

5.6 Conclusions

In this chapter, a fully-automated low-density (7 electrodes) EEG-based system for AD detection has been proposed, tested, and validated. The wICA algorithm was utilized for automated artifact removal. From wICA-enhanced signals, spectral, amplitude modulation and coherence features were computed to quantify the effects of AD on the EEG signals; later, classification between AD and Nold was carried out with a SVM classifier with linear kernel and l^1-norm penalty as a way to skip the feature selection step. LOSO CV was used in order to recreate realistic conditions. The proposed system was evaluated in two different datasets, namely Neuronetrix and Brazil-ld, which consisted of rsEEG data with open and closed eyes, respectively. Results show similarities between the two resting state protocols, specifically in the most relevant features, even when the recording conditions were different. Similar analyses are still needed to assess the performance of such low-density layouts under different experimental protocols for AD diagnosis.

Chapter 6

New Modulation-Domain Features for Improved AD Diagnosis

6.1 Preamble

The content in this chapter is extracted from the manuscript in preparation to be submitted to the IEEE Transactions on Neural Systems and Rehabilitation Engineering [117].

6.2 Introduction

In Chapters 4 and 5, the effects of the utilization of AAH algorithms and portable low-density EEG devices were respectively evaluated in the context of AD diagnosis using rsEEG. So far, the EEG features used in the experiments presented in those chapters relied on classical EEG features and the recently proposed AM rate-of-change features, described in Section 2.7.4.1. However, the formulation of all these features is based on partitioning the EEG spectrum into the traditional frequency bands, which in turn have been defined by the study of EEG recordings from healthy subjects as described in Section 1.2. In fact, most published studies on EEG-based AD diagnosis have used and proposed EEG features defined according to traditional EEG bands. While the use of these conventional frequency bands allows comparing the obtained results with those reported in the literature [87], they may not be the appropriate frequency partition for EEG signals in the study of AD.

Recent works have investigated whether AD diagnosis using rsEEG can be improved by analyzing features computed in frequency bands different from the traditional EEG bands. The work presented in [88] systematically explored the lower and upper frequency bounds for different EEG frequency bands to find the optimal bands for the Nold vs mild-AD classification in a dataset comprised of 24 Nold and 17 mild-AD participants. The discriminative power for each of the explored bands was evaluated with the relative-power (averaged across electrodes) feature for such a band. As a result, three optimized bands (4-7 Hz, 8-15 Hz and 19-24 Hz) were identified and their classification performance was compared with the one obtained with their closest traditional bands: theta, alpha and beta, respectively. In the three cases the features derived from the optimized bands outperformed features from the traditional bands. A more recent work [89] expanded the results found in [88] by using the optimized-band approach not only for spectral features, but also for synchrony features. The approach of optimizing frequency bands was evaluated in the classification of two datasets, one comprised of Nold and AD participants (same dataset as [88]), and the second one comprised of 56 Nold and 25 MCI participants. Similar to the previous results, the bandwidths of the optimized frequency bands differ from the traditional bands, and the use of EEG features derived from these optimized bands improved the classification performance for both datasets. Interestingly, the optimized bands for the two tested datasets were different, suggesting that specific regions of the spectrum are more relevant depending on the AD progression. In both studies ([88] and [89]), the optimized bands did not always correspond to traditional bands; very often they are either a narrow subband of one traditional band, or include frequency components from two traditional bands. These results suggest that optimal features for AD diagnosis may be defined in specific frequency ranges that differ from traditional EEG bands.

Motivated by the promising results obtained with the use of the AM rate-of-change features (which are defined in terms of traditional EEG bands) to characterize the neuromodulatory deficit due AD presented in [36, 90], and the findings obtained with the use of optimized frequency ranges presented in [88, 89], we proposed the use of the modulation spectrogram approach, described in Section 3.4, to analyze the neuromodulatory deficit on the rsEEG signals due AD without the constraint of the traditional frequency bands. This chapter has as goal to present the insights and outcomes obtained by exploring rsEEG signals in the modulation domain.

6.3 Materials and methods

6.3.1 EEG recordings

The exploratory analyses presented in this chapter were performed on the dataset described in Section 4.3.1, which includes 20-channel rsEEG recordings, plus 8 virtual bipolar channels, from 59 subjects in three different populations, Nold, mild-AD and moderate-to-severe AD. The pre-processing of the rsEEG recordings was the same that the one described in Section 4.3.2, and three different versions of the recordings were studied: manually selected, raw, and wICA-enhanced EEG data.

6.3.2 Modified modulation spectrogram

In these experiments we used the modulation-domain representation to characterize the periodicity in the power time series for different frequencies of the EEG signals. To accomplish this, the formulation of the modulation spectrogram presented in Section 3.4 is modified to analyze the power time series rather than the amplitude time series. Henceforth, the modulation spectrograms presented in this chapter are computed as:

$$X(f, f_{mod}) = \mathcal{F}_t \left\{ |X(t,f)|^2 \right\}. \tag{6.1}$$

6.3.3 Receiver operating characteristic curve

The receiver operating characteristic (ROC) curve is the plot of *sensitivity* against 1-*specificity*, for a one-feature binary classification. The ROC curve is generated from the different obtained values for sensitivity and specificity as the discrimination threshold of the feature varies. From this plot the performance of the feature, i.e., the separability of the groups based on that feature, is quantified by calculating the area under the ROC curve (AUC) [91, 192]. Two groups that are perfectly separable lead to an AUC of 1, while a random guess leads to an AUC of 0.5; as the AUC metric is symmetric around 0.5, an AUC value of 0.8 indicates the same separability as an AUC value of 0.2, as illustrated by Figure 6.1.

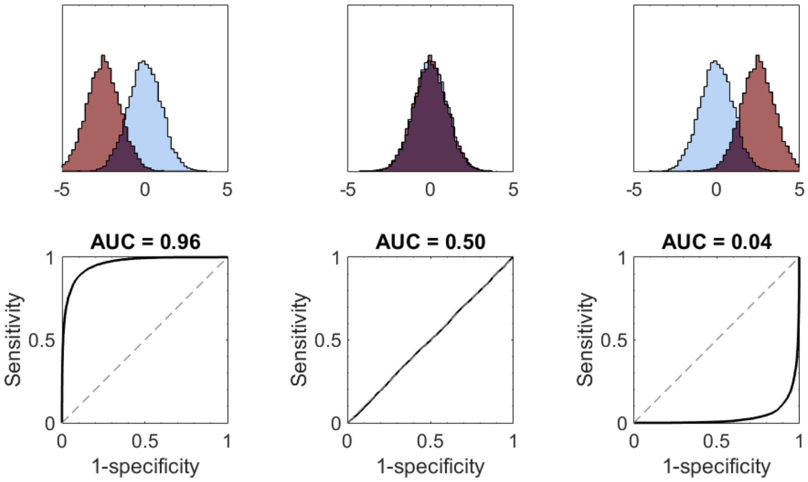

Figure 6.1 – Distribution overlap and its relationship with the ROC and AUC.

6.4 Modulation spectrogram of rsEEG for AD diagnosis

As a first approach, we explored the rsEEG differences in the modulation domain for recordings from Nold and AD participants. For a channel in the rsEEG recordings the spectrotemporal representation $X(t, f)$, was computed using the CWT with the complex Morlet wavelet as mother wavelet for frequencies from 1 to 45 Hz with 1-Hz step and $n_c = 6$. To prevent the use of CWT from introducing phase distortion and delay, the wavelet kernels were designed to be symmetric and have an odd length (L) [131, 13]. Then, the power spectrogram ($|X(t, f)|^2$) was split in 8-second epochs and for each epoch the modulation spectrogram was computed as per (6.1), the power modulation spectrogram ($|X(f, f_{mod})|^2$) was computed for all the epochs in the recording. To allow the comparison of the obtained power modulation spectrograms among epochs and among subjects, each power modulation spectrogram was normalized by its total power. This process is depicted in 6.2.

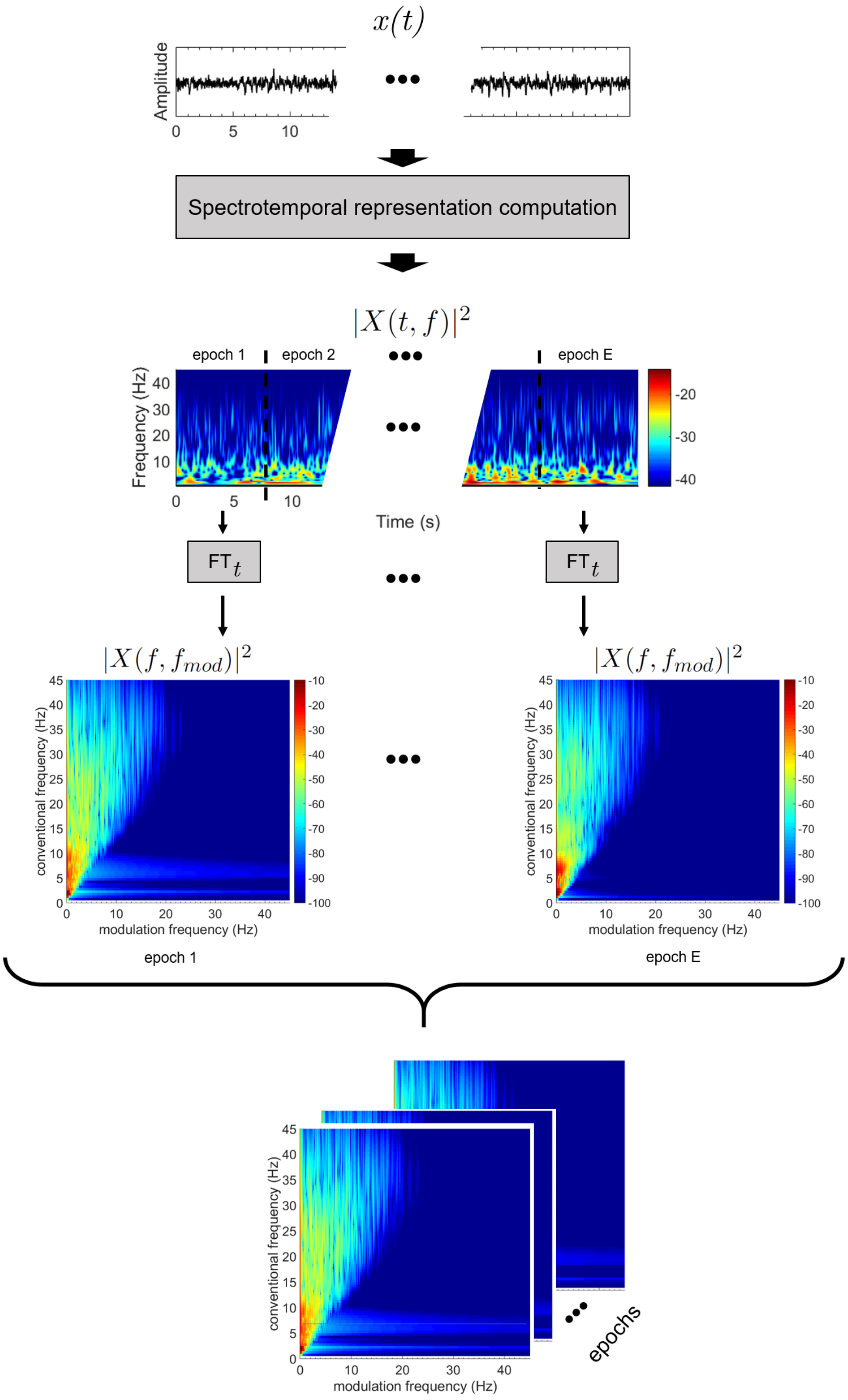

Figure 6.2 – Pipeline for computing the power modulation spectrograms, for one EEG channel.

The processing pipeline presented in Figure 6.2 is performed for each of the (electrode and virtual) channels in the recordings; thus for each subject, a collection of normalized power modulation spectrograms is obtained for each channel as shown in Figure 6.3.

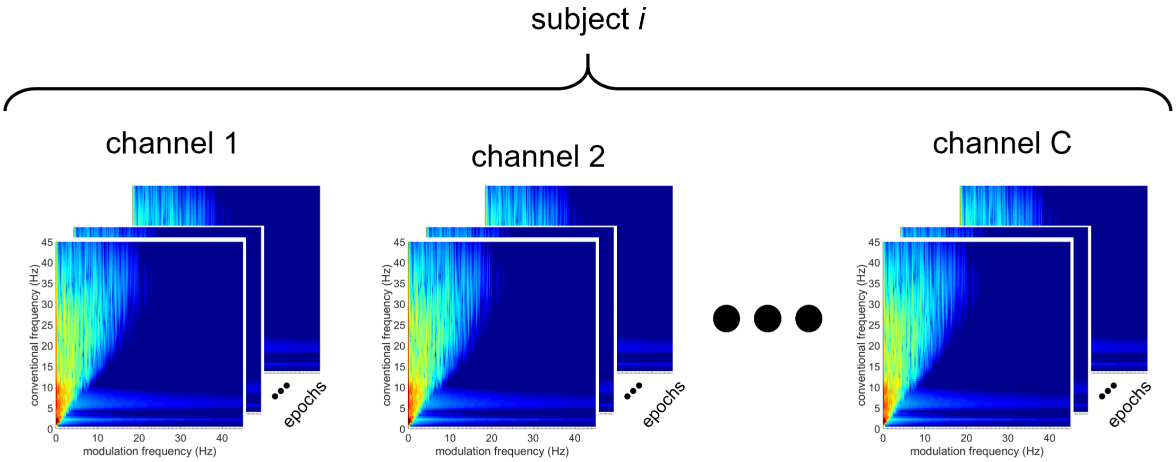

Figure 6.3 – Collection of power modulation spectrograms for a single subject.

The normalized power modulation spectrograms obtained for a given channel were aggregated first over all epochs within a subject, as depicted in Figures 6.2 and 6.3, then over all subjects within each group, resulting in two collections (one per group) of normalized power modulation spectrograms. Then, for each (f, f_{mod}) pair in the normalized power modulation spectrograms, the AUC was computed; this process leads to a representation of the AUC values in the modulation domain. Figure 6.4 depicts this process for one channel.

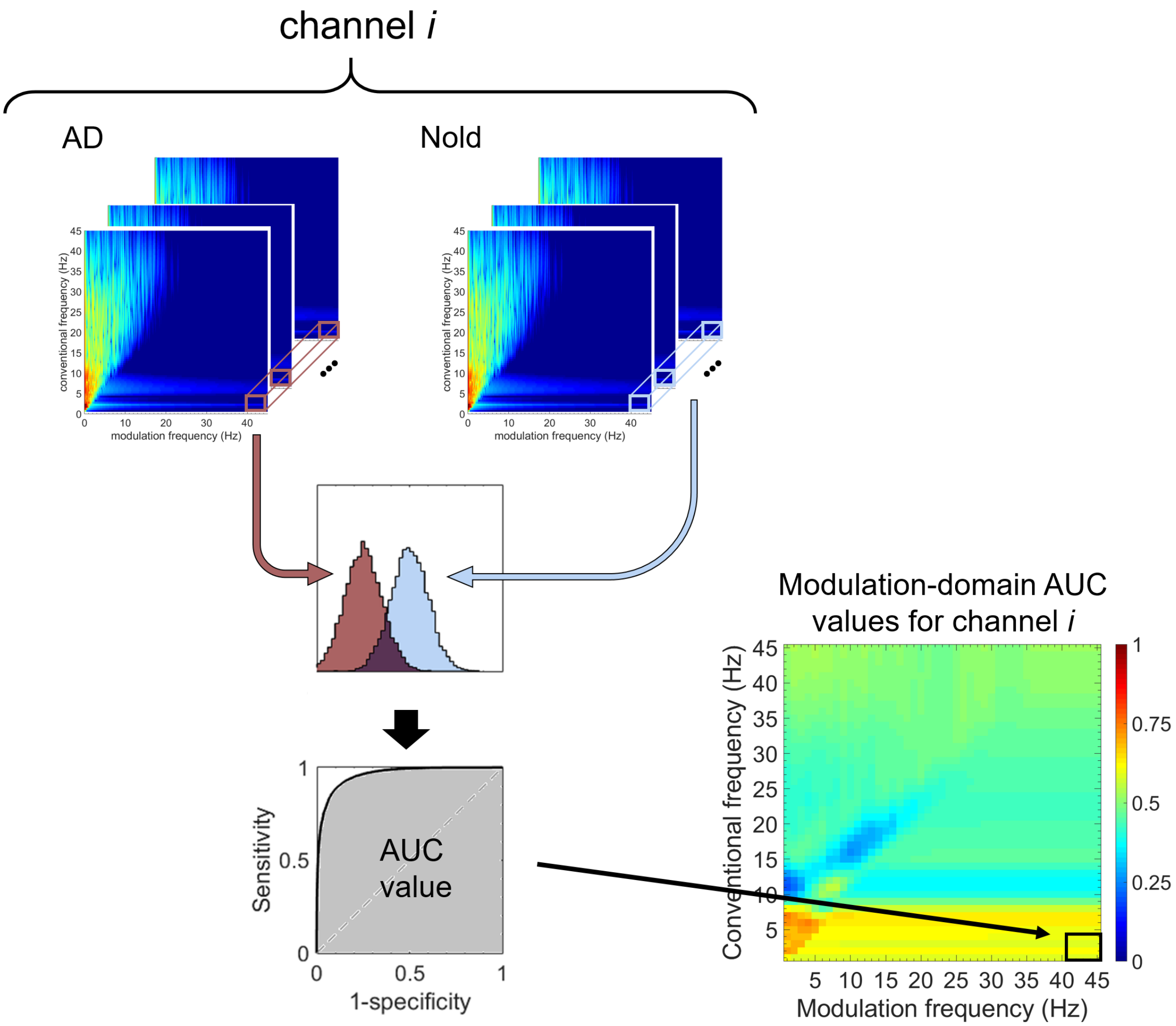

Figure 6.4 – Comparison of power modulation spectrograms between Nold and AD groups for a single EEG channel.

As the computation of the AUC values was performed for all the channels in the recordings, the result is a topographical plot, which presents the AUC values from the group comparison in the modulation domain for each channel in its respective position. Figure 6.5 depicts the topographical plot obtained from the comparison of the normalized power modulation spectrograms between the Nold and AD groups by analyzing the manually selected rsEEG recordings. By comparing the Nold and AD groups using the raw and wICA-enhanced EEG data, similar AUC topographic plots were obtained, as shown in Figures 6.6 and 6.7 respectively.

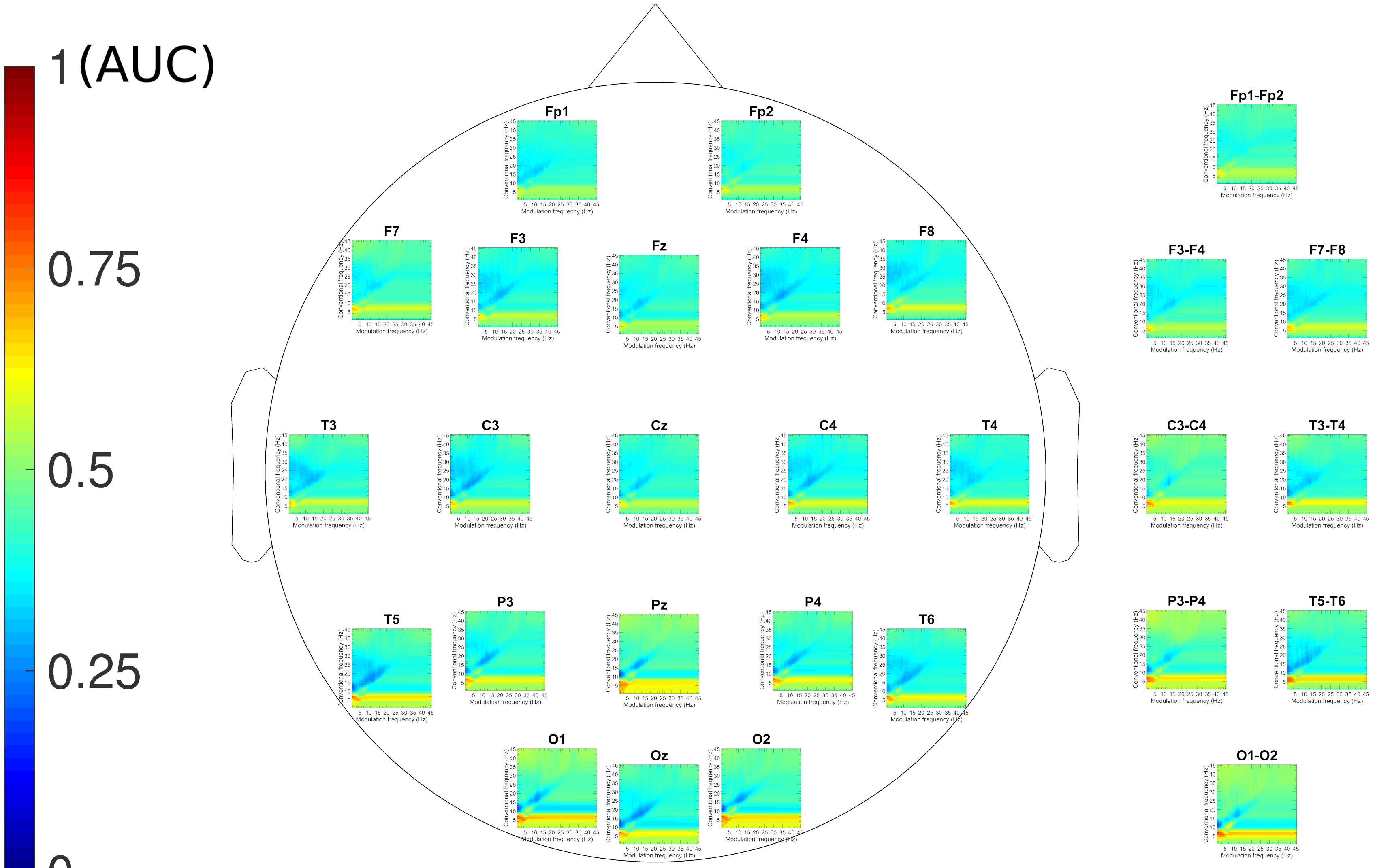

Figure 6.5 – AUC topographical plot for Nold vs AD, derived from manually selected EEG.

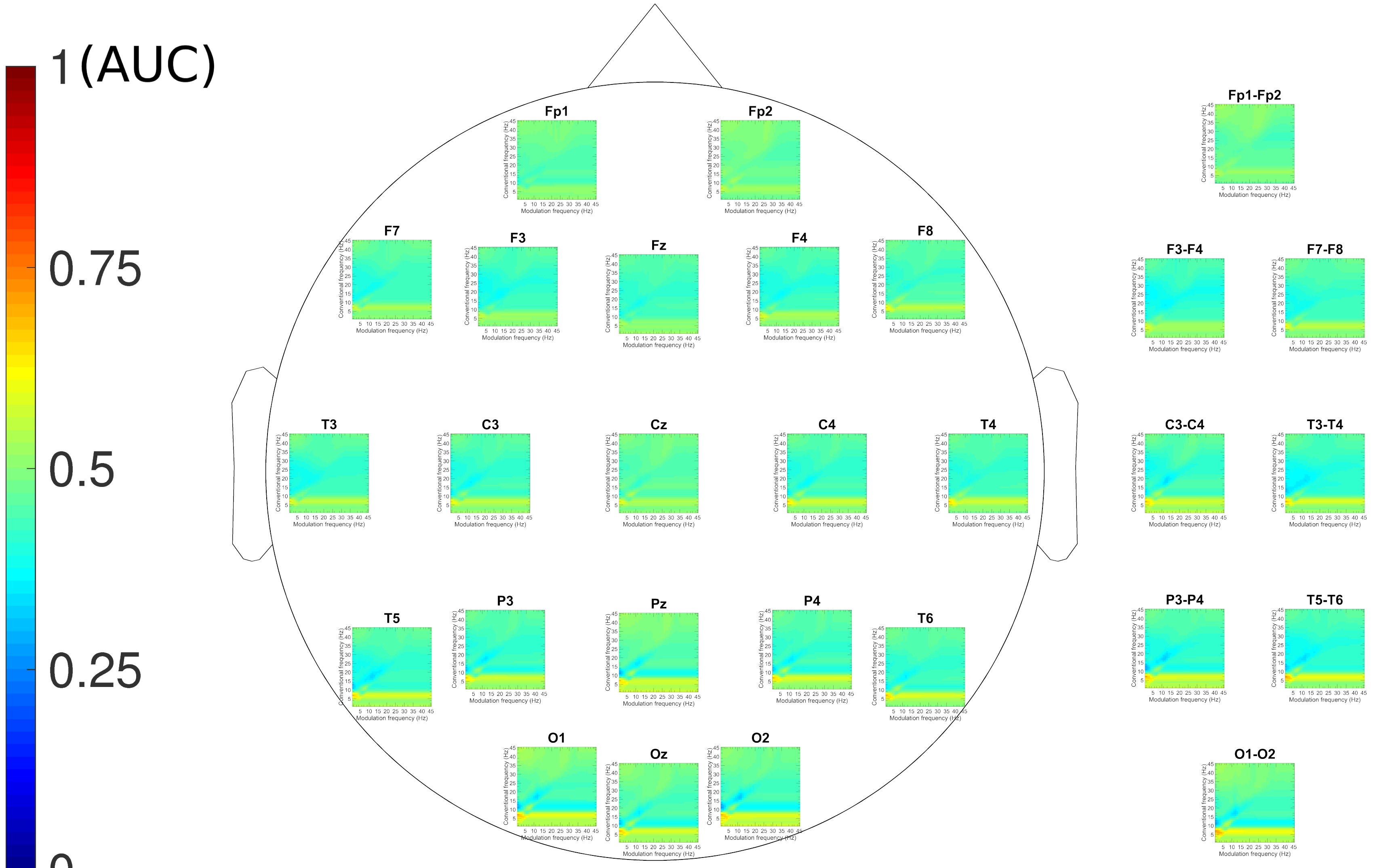

Figure 6.6 – AUC topographical plot for Nold vs AD, derived from raw EEG.

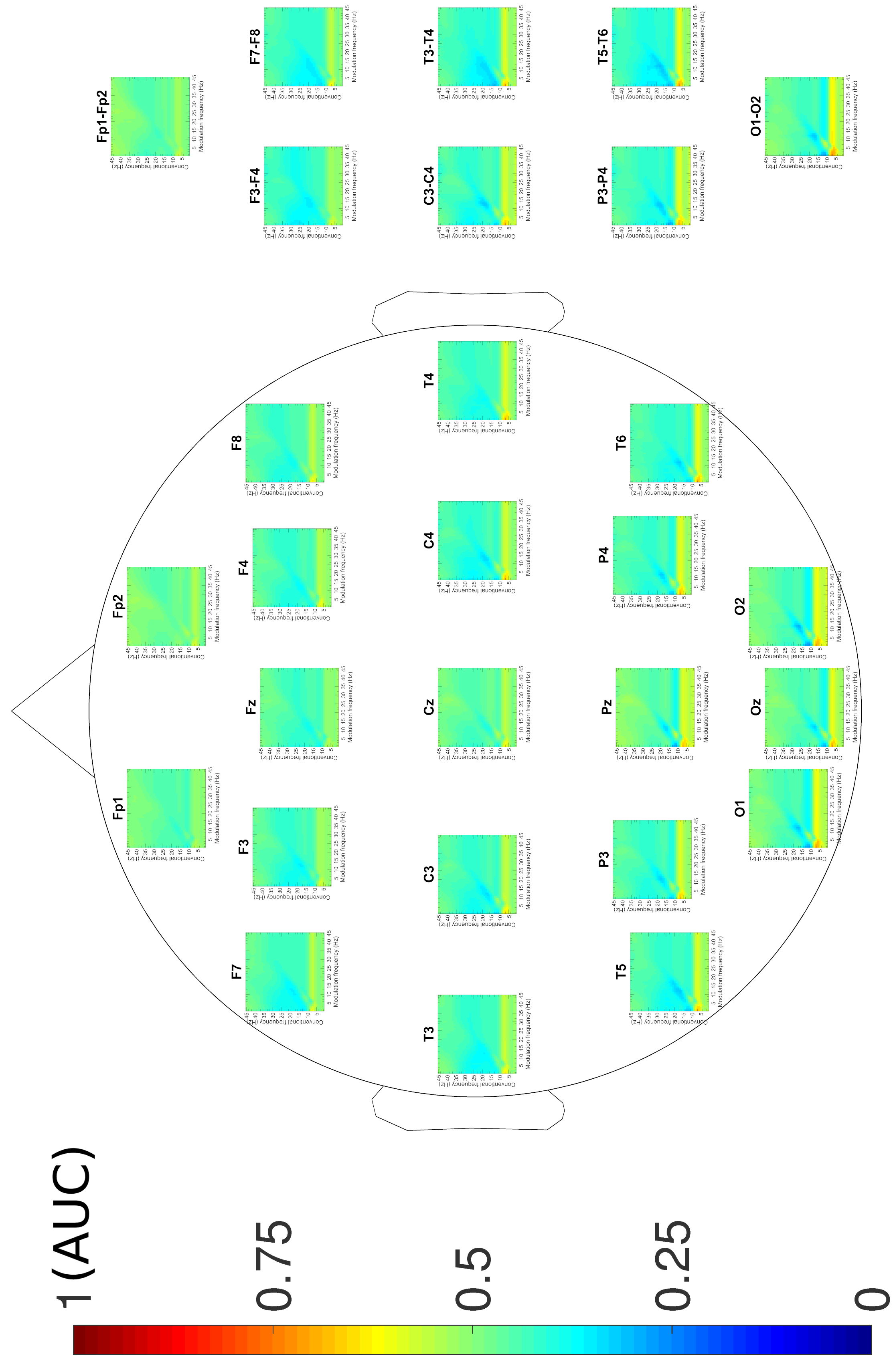

Figure 6.7 – **AUC topographical plot for Nold vs AD, derived from wICA-enhanced EEG**

In the AUC topographical plots obtained from the comparison between Nold and AD groups (Figures 6.5, 6.6 and 6.7), it is possible to identify regions in the modulation domain where the AUC values are far from 0.5. Specifically, there are three regions (R1, R2 and R3) that cluster the best AUC values; these regions are shown in Figure 6.8a that corresponds to the average across the 20 electrodes of the AUC topographical plot presented in Figure 6.5, which was obtained from comparison between Nold and AD groups for manually selected EEG data. In similar manner, the Figures 6.8b and 6.8c present the average across the 20 electrodes of the AUC topographical plot presented in Figure 6.6 and Figure 6.7, which were obtained obtained from comparison between Nold and AD groups for raw and wICA data respectively. Note that the average across channels provides an overall view of differences between groups in the modulation domain facilitating the identification of the regions with better AUC values; however, all the spatial information is removed.

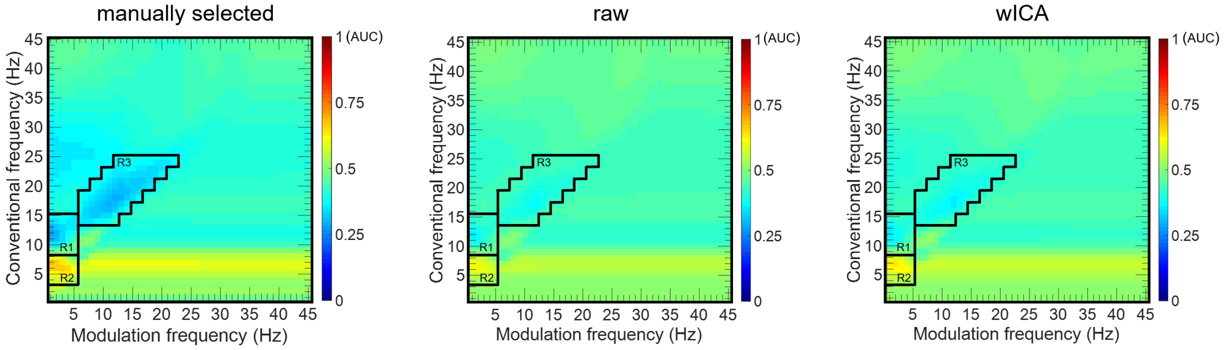

(a) (b) (c)

Figure 6.8 – AUC values averaged across monopolar electrodes from Nold vs AD comparison with: (a) manually selected, (b) raw, and (c) wICA EEG recordings.

Motivated by the identification of these three regions in the modulation domain to differentiate between Nold and AD populations, we proceeded to study their biological origin by estimating the cortical sources responsible for these differences in the modulation domain.

6.4.1 Estimation of current source density

Once the three main regions in the modulation domain were identified as shown in Figure 6.8, to determine if these regions in the modulation domain are related to AD, the manually selected EEG signals were filtered in the modulation domain to keep only R1, R2, R3 and R1+R2+R3 modulation components. Filtering in the modulation domain was performed as described in Section 3.4.1.

The modulation-domain filtered EEG recordings were then used to estimate the electric neuronal activity distribution with eLORETA (described in Section 2.6.4), whose implementation is freely provided by The KEY Institute of Brain-Mind Research, University Hospital of Psychiatry, Switzerland[1]. The used head model and the electrode coordinates are based on the Montreal Neurological Institute (MNI) average MRI brain map, MNI152 template [193]. The solution space was limited to the cortical gray matter, including 6239 voxels with spatial resolution of 5 cubic mm. The corresponding Brodmann areas (BAs) are reported using the MNI space with correction to the Talairach space [194]. The eLORETA cortical current source density solution was computed for eight (predefined in LORETA-KEY software) frequency bands: delta (1.5-6 Hz), theta (6.5-8 Hz), alpha1 (8.5-10 Hz), alpha2 (10.5-12 Hz), beta1 (12.5-18 Hz), beta2 (18.5-21 Hz), beta3 (18.5-30 Hz) and full-band or omega (1.5-30 Hz); the eLORETA solutions were computed in these frequency bands to make possible the comparison between our results and ones reported in the literature. The statistical analysis of localization solutions was performed with the (available in LORETA-KEY software) statistical non-parametric mapping (SnPM) method. The difference in cortical source localization between groups was assessed for each of the eight frequency bands with voxel-by-voxel independent F-ratio tests, based on eLORETA log-transformed current source density power. Cortical voxels with significant differences were identified by means of a non-parametric randomization procedure (5000 randomizations) in the three-dimensional statistical mapping. The mean source power in each voxel and the distribution in the permutated values was compared, with threshold set at a p=0.05 significance level after correction for multiple comparisons across all voxels and frequencies [195]. We used eLORETA method for source localization in order to compare the results with the reported ones in the literature of EEG-based AD study.

Table 6.1 reports the BAs with statistically significant difference (at least $p<0.05$) on eLORETA in the comparison Nold vs AD for manually selected EEG signals. These results are in line with results reported in the AD literature for the comparison between Nold and AD participants where LORETA methods have been widely used [195, 189, 196, 197, 106, 198]. The LORETA solutions obtained for the frequency bands under analysis for the Nold and AD cohorts are depicted in Figure 6.9; these LORETA solutions were obtained with the EEG signals, which were filtered in the modulation domain to keep R1+R2+R3.

---

[1] `http://www.uzh.ch/keyinst/loreta.htm`

Region	***Band*** **Lobe (BAs)**	**Region**	***Band*** **Lobe (BAs)**
R1	*high-alpha (AD < N)* LL (18,19,23,29,30,31,37) OL (7,17*,18*,19*,23,30,31,37) PL (7,19,31,39,40) TL (13,19,20,21,22,37,39,40)	R2	*theta (AD > N)* FL (5,6,31,43,44) LL (20,23,27,28,29,30,31*,34,35,36) OL (19,23,31) PL (5,7,19,31,39,40) TL (13,20,21,22,38,39,41)
R3	*high-alpha (AD < N)* LL (18,19,23,29,30,31) OL (7,17,18,19,23,30,31,37) PL (19,31) TL (19,20,37,39)	R1+R2+R3	*high-alpha (AD < N)* LL (18,19,23,29,30,31,37) OL (7,17*,18*,19*,23*,30*,31,37*) PL (7,19*,31,39,40) TL (13,19,20,21,22,37,39,40)

Table 6.1 – Brodmann areas with statistically significant difference ($p<0.05$); the asterisk indicates $p<0.01$. LL = limbic lobe, OC = occipital Lobe, PL = parietal lobe, TL = temporal lobe, and FL = frontal lobe.

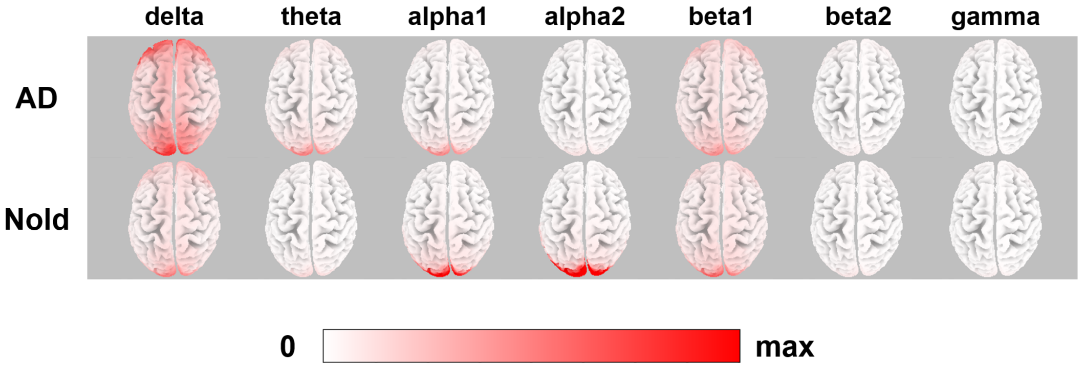

Figure 6.9 – Group average of normalized LORETA solutions, scaled to the max value (average of alpha2 Occipital sources in Nold cohort)

By analyzing Figure 6.8 and the results reported in Table 6.1, it can be noted that filtering the signal in the modulation domain for R1 and R3 conserves the information that roughly corresponds to the band alpha2 (high-alpha), and R2 conserves information related to the theta band. As such, the results presented here suggest that the differences observed in the modulation domain are related to the presence of AD. Given these insights, it is expected that the analysis of these regions in the modulation domain can improve rsEEG-based AD diagnosis. Moreover, filtering the EEG signals in the modulation domain has the potential of enhancing the rsEEG signal as only components of interest for AD diagnosis are kept, while rsEEG components not related to AD or that may be corrupted by artifacts are removed.

6.5 Modulation spectrogram of rsEEG for AD progression

Section 6.4 presented analysis and results over the differences in the modulation domain between Nold and AD groups. However, in those results the AD group encompassed mild-AD (AD1) and moderate-sever-AD (AD2) participants. For that reason, the same analysis was performed between Nold and each of the AD subgroups, and between themselves. Figure 6.10 depicts the average across electrodes obtained from the comparisons Nold vs. AD1, Nold vs. AD2 and AD1 vs. AD2. Interestingly, different patterns in the modulation spectrogram were observed, suggesting this representation in the modulation domain could provide valuable information to additionally perform assessment of AD progression.

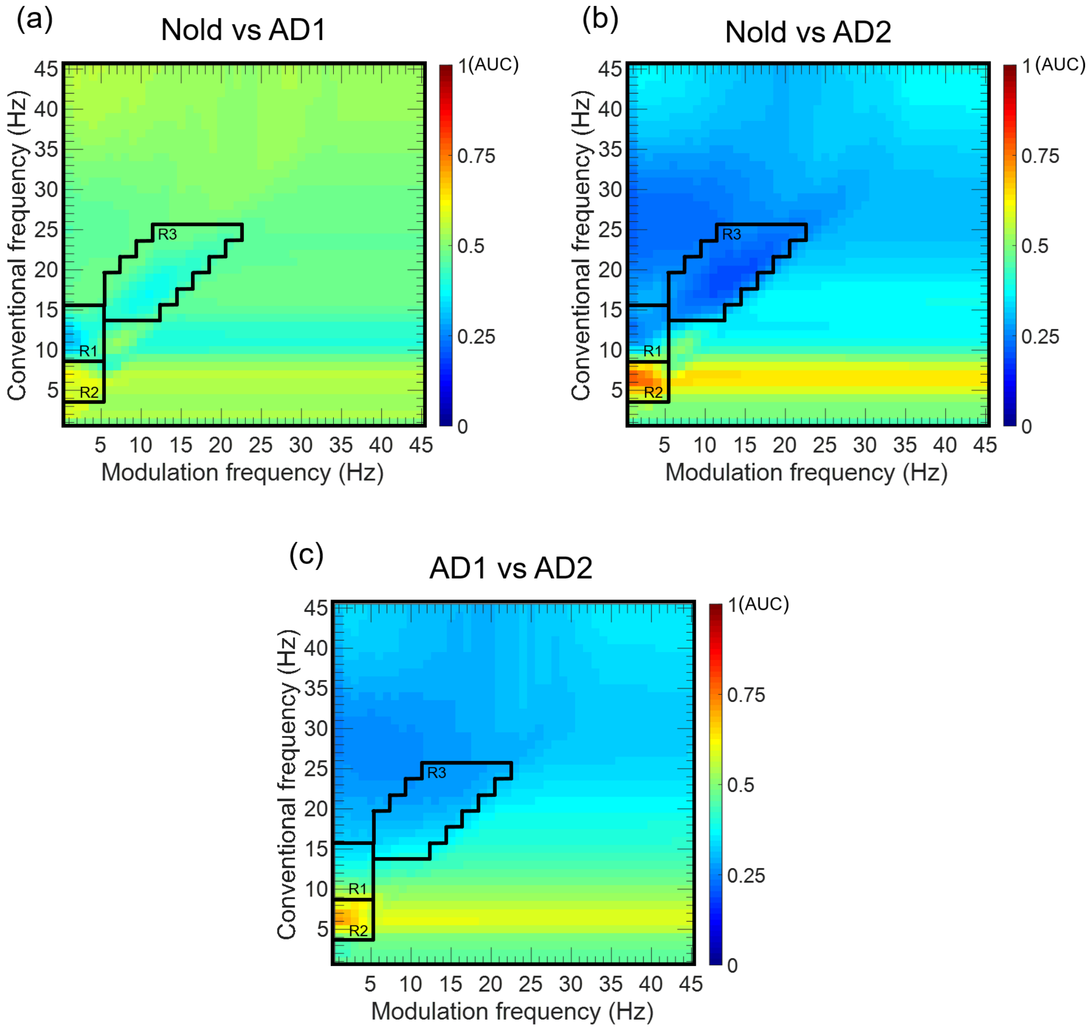

Figure 6.10 – AUC values averaged across monopolar electrodes with manually selected EEG for (a) Nold vs AD1, (b) Nold vs AD2, and (c) AD1 vs AD2 comparisons.

To assess the discriminatory power of the regions in the modulation domain, features based in those regions were proposed and their classification performance was compared with traditional EEG features presented in Section 2.7.

6.6 AD diagnosis using modulation domain EEG features

6.6.1 Modulation domain features

To obtain a metric for each of the regions in the power modulation spectrogram, we proposed the total power of the region as feature for AD diagnosis. As such, the power of a region is defined as the integral of the normalized power modulation spectrogram over the region.

$$P_i = \iint_{R_i} = |X(f, f_{mod})|^2 df\, df_{mod}. \tag{6.2}$$

Additionally to the features, P_1, P_2 and P_3, derived from the three identified regions, R_1, R_2 and R_3 respectively, the ratios between features, namely, $P_1/P_3, P_2/P_1$ and P_2/P_3 were also computed.

6.6.2 Feature extraction

The modulation domain features were extracted for each of the normalized spectrograms obtained from 8-s epochs, for the 28 channels (20 electrodes + 8 virtual bipolar signals). Besides the proposed features, spectral and AM rate-of-change features, described in Sections 2.7.1.1 and 2.7.4.1 respectively, were also computed in 8-s epochs for the 28 channels. Table 6.2 presents a list of the computed features for the manually selected, raw and wICA-enhanced rsEEG recordings.

Table 6.2 – Computed features for each 8-s epoch.

Feature group	**Features**
Modulation domain features	P_1
(Computed for each of the 28 channels)	P_2
	P_3
	P_1/P_3
	P_2/P_1
	P_2/P_3
Spectral features	delta
(Computed for each of the 28 channels)	theta
	alpha
	low-alpha
	high-alpha
	beta
	delta-beta
	theta-beta
	gamma
Amplitude modulation rate-of-change	delta-mdelta
(Computed for each of the 28 channels)	theta-mdelta
	theta-mtheta
	alpha-mdelta
	alpha-mtheta
	beta-mdelta
	beta-mtheta
	beta-malpha
	beta-mbeta
	gamma-mdelta
	gamma-mtheta
	gamma-malpha
	gamma-mbeta
	gamma-mgamma

The computed features were grouped into five feature sets: PSD (spectral features), MOD (AM rate-of-change features), RG3 (power in the modulation regions of interests), and two combinations of these sets, namely, PSD+MOD and PSD+RG3. In the next section we present the results obtained in the AD classification with the proposed RG3 features and compare their classification performance with the one obtained with spectral and AM ratio-of-change features. In our experiments we performed feature averaging over 5 consecutive epochs as described in [76].

6.6.3 Feature selection and classification

A total of 25% of the available data for each EEG recording was set apart to perform feature selection. The top-24 features were selected based on ANOVA F-value between feature and label. For classification a SVM classifier was used, with the following parameters: linear kernel, l^1-norm penalization, and a default regularization coefficient value of C = 1. For feature selection as well as for classification, the open-source scikit-learn (machine learning for Python) [82] was used. The performance of the classifier was reported subject-wise with LOSO CV. We evaluated the discriminatory power of the extracted features (Section 6.6.2) in the three rsEEG datasets, i.e., manually selected, raw and wICA-enhanced recordings, for four classification tasks, namely, (*i*) Nold vs AD, (*ii*) Nold vs AD1 vs AD2, (*iii*) Nold vs AD1 and (*iv*) AD1 vs AD2. Tables 6.3 to 6.6 report the accuracy performance achieved for the tested classifications tasks for each combination of feature sets and EEG signal enhancement approaches respectively.

Table 6.3 – Accuracy for N vs. AD. The bold figure indicates the best performance for each EEG recording.

	Feature Sets				
EEG recordings	PSD	MOD	RG3	PSD+MOD	PSD+RG3
manually selected	79.7	76.3	**88.1**	79.7	81.4
raw	72.9	62.7	76.3	76.3	**78.0**
wICA	74.6	66.1	74.6	71.2	**78.0**

Table 6.4 – Accuracy for N vs. $AD1$ vs. $AD2$. The bold figure indicates the best performance for each EEG recording.

	Feature Sets				
EEG recordings	PSD	MOD	RG3	PSD+MOD	PSD+RG3
manually selected	62.7	52.5	62.7	**64.4**	**64.4**
raw	59.3	37.3	54.2	50.8	**62.7**
wICA	54.2	47.5	52.5	47.5	**57.6**

Table 6.5 – Accuracy for N vs. $AD1$. The bold figure indicates the best performance for each EEG recording.

	Feature Sets				
EEG recordings	PSD	MOD	RG3	PSD+MOD	PSD+RG3
manually selected	**81.8**	75.0	77.3	79.5	75.0
raw	65.9	**72.7**	65.9	**72.7**	**72.7**
wICA	63.6	68.2	61.4	63.6	**72.7**

Table 6.6 – Accuracy for $AD1$ vs. $AD2$. The bold figure indicates the best performance for each EEG recording.

	Feature Sets				
EEG recordings	PSD	MOD	RG3	PSD+MOD	PSD+RG3
manually selected	68.6	48.6	68.6	60.0	**80.0**
raw	65.7	62.9	**74.3**	60.0	**74.3**
wICA	68.6	62.9	**71.4**	65.7	**71.4**

A notable characteristic of the AUC topographic plots presented in Figures 6.5, 6.6 and 6.7 is that the differences between groups are not uniform across the scalp. In the next section, we present the evaluation of the classification performance using EEG features derived from a limited number of channels.

6.7 Classification with low-density EEG

The results presented in Section 6.6.3 were based on features extracted from the layout of 20 (plus 8 virtual bipolar) channels. In this section, we present the performance obtained with the newly proposed features for a low-density setup comprised of only 7 channels, similar to the system evaluated in Chapter 5. We assessed two 7-channel layouts, the first layout (Figure 6.11a) corresponds to the one used in experiments reported in Chapter 5, the second layout (Figure 6.11b) was motivated by the AUC topographic plots presented in Figures 6.5, 6.6 and 6.7 where better AUC values were present in electrodes over the occipital, parietal and temporal lobes. EEG signals from both low-density layouts were evaluated using the same methodology described in Section 6.6.3.

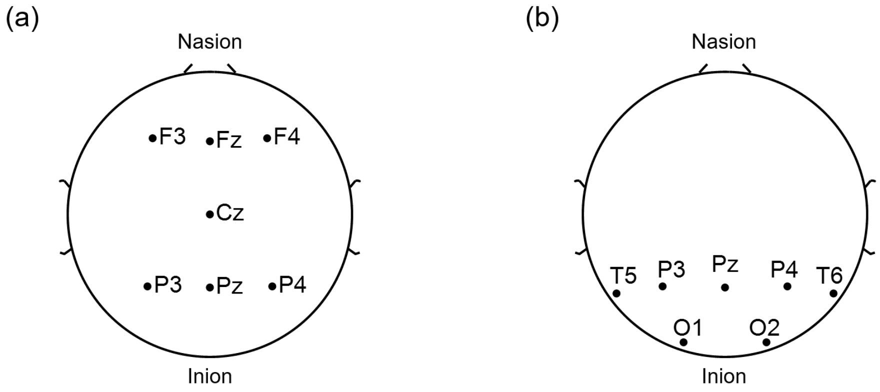

Figure 6.11 – Portable layouts. (a) Layout used for experiments in Chapter 5. (b) Proposed layout based on differences in AUC topographic plots.

Tables 6.7 to 6.10 report the accuracy performance achieved for the tested classifications tasks for each combination of feature sets and EEG signal enhancement approaches, with the use of the 7-channel layout depicted in Figure 6.11a.

Table 6.7 – Accuracy for N vs. AD using the 7-channel layout shown in Figure 6.11a. The bold figure indicates the best performance for each EEG recording.

	Feature Sets				
EEG recordings	PSD	MOD	RG3	PSD+MOD	PSD+RG3
manually selected	81.4	71.2	76.3	81.4	**84.7**
raw	76.3	**79.7**	74.6	74.6	78.0
wICA	71.2	59.3	67.8	71.2	**78.0**

Table 6.8 – Accuracy for N vs. $AD1$ vs. $AD2$ using the 7-channel layout shown in Figure 6.11a. The bold figure indicates the best performance for each EEG recording.

	Feature Sets				
EEG recordings	PSD	MOD	RG3	PSD+MOD	PSD+RG3
manually selected	**67.8**	47.5	59.3	**67.8**	61.0
raw	**61.0**	42.4	**61.0**	54.2	57.6
wICA	52.5	45.8	**57.6**	50.8	52.5

Table 6.9 – Accuracy for N vs. $AD1$ using the 7-channel layout shown in Figure 6.11a. The bold figure indicates the best performance for each EEG recording.

	Feature Sets				
EEG recordings	PSD	MOD	RG3	PSD+MOD	PSD+RG3
manually selected	72.7	68.2	**79.5**	70.5	70.5
raw	63.6	54.5	63.6	65.9	**70.5**
wICA	**70.5**	50.0	65.9	65.9	59.1

Table 6.10 – Accuracy for $AD1$ vs. $AD2$ using the 7-channel layout shown in Figure 6.11a. The bold figure indicates the best performance for each EEG recording.

	Feature Sets				
EEG recordings	PSD	MOD	RG3	PSD+MOD	PSD+RG3
manually selected	65.7	62.9	60.0	60.0	**68.6**
raw	**77.1**	71.4	68.6	68.6	68.6
wICA	**71.4**	65.7	**71.4**	68.6	**71.4**

Tables 6.11 to 6.14, in turn, report the performance achieved for the tested classifications tasks for each combination of feature sets and EEG signal enhancement approaches, with the use of the 7-channel layout depicted in Figure 6.11b.

Table 6.11 – Accuracy for N vs. AD using the 7-channel layout shown in Figure 6.11b. The bold figure indicates the best performance for each EEG recording.

	Feature Sets				
EEG recordings	PSD	MOD	RG3	PSD+MOD	PSD+RG3
manually selected	81.4	81.4	**88.1**	81.4	81.4
raw	78.0	66.1	74.6	78.0	**79.7**
wICA	72.9	62.7	72.9	**76.3**	**76.3**

Table 6.12 – Accuracy for N vs. $AD1$ vs $AD2$ using the 7-channel layout shown in Figure 6.11b. The bold figure indicates the best performance for each EEG recording.

	Feature Sets				
EEG recordings	PSD	MOD	RG3	PSD+MOD	PSD+RG3
manually selected	59.3	52.5	**66.1**	62.7	**66.1**
raw	54.2	47.5	55.9	**59.3**	47.5
wICA	**62.7**	42.4	54.2	52.5	54.2

Table 6.13 – Accuracy for N vs. $AD1$ using the 7-channel layout shown in Figure 6.11b. The bold figure indicates the best performance for each EEG recording.

	Feature Sets				
EEG recordings	PSD	MOD	RG3	PSD+MOD	PSD+RG3
manually selected	77.3	**84.1**	75.0	70.5	65.9
raw	72.7	59.1	70.5	68.2	**72.7**
wICA	65.9	59.1	59.1	63.6	**68.2**

Table 6.14 – Accuracy for $AD1$ vs. $AD2$ using the 7-channel layout shown in Figure 6.11b. The bold figure indicates the best performance for each EEG recording.

	Feature Sets				
EEG recordings	PSD	MOD	RG3	PSD+MOD	PSD+RG3
manually selected	62.9	57.1	65.7	60.0	**65.7**
raw	**74.3**	65.7	68.6	**74.3**	71.4
wICA	68.6	68.6	**74.3**	65.7	68.6

6.8 Discussion

6.8.1 Performance analysis of full 20-channel system

Given the fact that the features in the RG3 feature set were derived heuristically from the comparison between the Nold and AD groups presented in Section 6.4, they present an outstanding performance (88% accuracy) in the Nold vs AD classification task, Table 6.3. Moreover, the use of the RG3 features, either alone or in combination with spectral features resulted for most classification tasks in improved accuracy. As such these features seem to be informative for the assessment of AD progression; however, due to the way they were designed, they may not be optimal for such assessment. In order to improve the definition of such features, image processing methods can be implemented to extract other features from the modulation spectrogram that may be more insightful for the identification of different AD stages.

6.8.2 Performance analysis of 7-channel systems

The proposed features were evaluated in two 7-channel layouts, depicted in Figure 6.11. The first layout, presented in Figure 6.11a, was proposed to compare the performance of the newly proposed features with the results presented in Chapter 5. With this layout, it can be seen in Table 6.7 that the use of the RG3 features improves the baseline classification obtained with PSD features. Moreover, for the wICA-enhanced signals the improvement was from around 70% (as reported in Tables 5.3 and 6.7) to nearly 80%. The second proposed low-density layout (depicted in Figures 6.11b) presented a classification performance in line with that obtained with the 20-channel layout for the use of RG3 features and manually selected data; this is because the electrodes for this setup were selected based on their discriminative power, displayed as AUC values in Figure 6.5. Similar to the results presented in Chapter 5, across the explored classification tasks the reduction of channels leads to a lower classification performance.

6.8.3 Effects of EEG processing in the modulation representation

From the AUC topographical plots obtained for raw and wICA-enhanced EEG recordings, presented in Figures 6.6 and 6.7 respectively, it is possible to note that both recordings lead to similar AUC values. As such, for all the classification performances obtained (Tables 6.3 to 6.14), the modulation-domain-derived features performed as well with the raw EEG recordings as with the wICA-enhanced, this may be due to noise robustness in the proposed features; further exploration is needed to determine this hypothesis.

6.9 Conclusions

In this chapter the use of innovative features derived from the modulation representation of the EEG signal was proposed. The proposed features are based on the modulation-domain as a way to explore the second-order periodicity of the EEG signals without the limitation that is inherent to the utilization of the classic EEG bands. Moreover, the use of such features may lead to insights on the brain activity not only for disorders such as AD but also for the study of the healthy brain.

Chapter 7

Summary, Future Research Directions, and Conclusion

7.1 Summary

In this doctoral thesis we have investigated the current challenges that arise with the utilization of rsEEG for the study of AD, namely:

- High sensibility of EEG signals to artifacts
- Number of electrodes in current EEG devices

To address such challenges, we have investigated: (*i*) the use of automated artifact handling techniques and their effect in rsEEG-based AD diagnosis, (*ii*) the viability of low-density EEG devices in AD diagnosis and its performance, and (*iii*) EEG features based on the modulation analysis, their design and performance in AD diagnosis. In the following subsections, we discuss the contributions of this thesis towards the development of portable, low-cost and automated rsEEG-based AD diagnosis and progression monitoring.

7.1.1 Automated artifact handling

The main difficulty of working with EEG signals is their high sensibility to artifacts. Therefore most researchers have resorted to working with "artifact-free" EEG signals, which are manually selected through expert visual inspection. Unfortunately, the use of this approach presents serious problems that make its implementation unsustainable in a practical clinic. As a consequence, the full automation of the artifact handling process is a pivotal step in the development of any EEG application. We investigated the effects of AAH methods on the AD diagnosis systems based on four types of EEG features. Experimental results showed that the diagnosis performance was improved with the use of AAH methods (compared with unprocessed data). From the fully automated AD diagnosis systems evaluated, the use of the wICA algorithm together with the feature set containing all the extracted features presented the best classification performance. Moreover, the performance obtained was in line with the one obtained with manually selected EEG. While AAH methods are reliable at removing some common EEG artifacts, they also distort the EEG information, specifically the one related to phase, hindering the performance of features and techniques that use that information. Ultimately, it is hoped that the use of such fully automated diagnostic tools can assist clinicians not only with AD detection but early diagnosis and disease progression monitoring.

7.1.2 Portable devices

Medical and research-degree EEG devices tend to be cumbersome and have as many electrodes as possible, as connectivity analysis and source localization methods perform better with this setup. However, the use of these EEG devices in AD assessment is not practical as they can evoke hardware-related stress on the participants, and imply long setup times that, in turn, extend the experiment sessions. The literature on the use of portable low-density EEG devices is limited, and does not compare the classification performance obtained with them against the performance of denser setups. As such, we explored the use of portable low-density EEG devices (7 electrodes), and investigated the effects of the reduction of number of electrodes on AD classification performance. Furthermore, we discussed the difference between awake rsEEG conditions, namely, open-eyes and closed-eyes protocols. The outcomes of our experiments suggest that there is a significant drop in classification performance due to the use of fewer channels, and both open-eyes and closed-eyes protocols rely on similar relevant features for diagnostics.

7.1.3 New modulation features

In AD research, EEG signals have been widely studied using classic spectral frequency bands, which were originally defined for healthy subjects. However, this approach may not be optimal, as EEG dynamics during the presence of AD may not be well characterized with these classic bands. In this thesis, we explore the EEG signals in the modulation domain, where they are not constrained to the classic bands. We proposed a set of new features based on this modulation representation, and showed that they lead to improvements in AD classification performance. These proposed features, when extracted from raw EEG, resulted in similar performances as when extracted from wICA-enhanced EEG. This finding shows their robustness against artifacts. This is an interesting finding, as it suggests that AAH methods may eventually be bypassed completely, thus making diagnostic systems even simpler and faster.

7.2 Future research directions

1. **Diagnosis generalization**: A common issue that arises in the EEG-based AD diagnosis is the huge amount of different experimental setups that have been reported. While most of the studied EEG recordings used the same resting-awake eyes-closed protocol, the session and recording durations are extremely variable. Regarding the EEG signal acquisition, most of the studies reported the use of the 10-20 international system as electrode placement guide, although the number of electrodes change, and in some cases even when the number of electrodes is the same their position is different. For EEG processing, in turn, the most used artifact-handling approach was the meticulous visual inspection by expert clinicians, which is inherently irreproducible and prone to errors. Also, a great diversity of methods have been used for feature selection and classification steps. A direct consequence of this experimental variability is the lack of standardized experimental protocol and EEG processing pipeline, which hinders the comparisons among different approaches across publications and even on the same data. Suggestions to improve this situation are: (*i*) standardization of protocol (resting-awake closed-eyes) and recordings conditions, i.e., minimal number of electrodes (and positions), and minimal duration of recordings; (*i*) development of an open-source baseline EEG pipeline (pre-processing, feature extraction, feature selection and classification); (*iii*)

studies could make use of proven AAH methods to report their results with raw and manually selected EEG signals, and contrast them to the ones obtained with AAH-cleaned signals, as was done in experiments presented in Chapter 4. Unfortunately, the lack of open AD databases containing EEG recordings is one of the most reported limitations in the field [23]. Overshadowed by other biomarkers, derived from CFS, MRI and PET data, EEG-based biomarkers have been not deeply explored for AD diagnosis outside of research. As a consequence initiatives for the study of AD such as the Alzheimer's Disease Neuroimaging Initiative (ADNI) do not include EEG recordings. The availability of such EEG databases would benefit the field, as while most of the studies take caution to avoid optimistic biases due to circular analyses, the proposed methodologies are rarely tested on different AD datasets to determine its validity and generalization.

Lastly, nowadays the progression of AD is regarded as two different time lines that go parallel but change from person to person, namely, the symptoms and the pathology progression, as described in Section 1.1. This consideration is pivotal in the development of EEG datasets for the characterization of AD, as in most of the AD datasets the labels for the participants are given based on the symptoms; however, EEG biomarkers, as all other biomarkers, measure the pathological aspect of AD. Thus ideally, EEG biomarkers should be compared with other neurodegenerative biomarkers, and not only to the diagnosis labels.

2. **Further development on modulation-domain features**: The utilization of features derived from the modulation spectrogram has been proven useful in other electrophysiological signals, e.g., in the estimation of the ECG signal quality [169] and enhancement [170], as well as in respiratory rate estimation from noisy ECG segments [124].

   Moreover, the development of modulation-domain features for EEG signals represents a promising technique for the study of "hidden" second-order periodicities in EEG signals in different recording conditions and paradigms. For example, the work presented in [126] explores the use of the AM rate-of-change features derived from a pre-task rsEEG segment in a functional near-infrared spectroscopy (fNIRS)-based affective neurofeedback paradigm to assess the multimodal approach in characterizing the performance of the users. The results of that work showed that the AM rate-of-change features were a good predictor of the user performance in the fNIRS neurofeedback; thus the predictor could be used to detect fNIRS-BCI illiterate users.

The features presented in this doctoral thesis were heuristically derived from the comparison of modulation spectrograms as described in Section 6.4, thus are fine-tuned for AD detection. As such, they may not be optimal for other EEG-based applications. Instead of designing modulation-domain features for each EEG application, the use of automatic techniques is needed to effectively extract relevant information from the modulation spectrogram. Inspired by the success in image applications and 2D data, the use of convolutional neural networks has been explored in the last few years to study the EEG in 2D representations (e.g., in multichannel time series or spectrograms [199, 200]). Similar approaches can be used for the analysis of the modulation spectrogram to remove the classic band limitation (as in the AM rate-of-change features) and the heuristic definition of features.

3. **Investigate the proposed methods with spatial navigation EEG recordings**: As we mentioned, recording conditions that involve additional hardware or require the participant to follow specific instructions are not suitable for EEG-based low-cost, portable AD diagnosis. Alternatively, with the use of portable EEG devices, recordings in other simple and natural conditions (rather than resting-state) such as reading, watching TV and walking are possible. Among these conditions, spatial navigation in virtual and real environments is of special interest in the study of AD [201, 202]. When exploring and navigating in a new environment, subjects (primarily) rely on one of two different navigation strategies: spatial or response. In the spatial strategy (also known as allocentric), the subject builds in memory a cognitive map based on the landmarks present in the environment and their spatial relationship. On the other hand, the response strategy (also known as egocentric) uses distances and turns based on the subject's current position and orientation (individual landmarks). There is evidence that these two navigation strategies rely on distinct brain areas with the spatial strategy leading to significant activity of the hippocampus, while the response strategy evokes sustained activity in the caudate nucleus [203]. Atrophy in the mediotemporal structures is a distinctive characteristic of AD. Neuropathological evidence suggests that AD-related changes may begin in the entorhinal cortex and subsequently spread to the hippocampus. These changes have been observed in fMRI volumetric studies in AD patients that consistently reveal both volume reductions in the hippocampus relative to age-matched controls, as well as a higher rate of hippocampal decline [17, 202]. Evidence provided by intracranial

electrophysiological recordings has shown a relationship between low frequency oscillations in the hippocampus (and throughout the cortex) and spatial navigation [204, 205].

In 2017, with the goal of a better understanding of the spatial navigation variations among different populations in the world, the mobile-app cognitive task Sea Hero Quest[1] was developed to gather data from more than 2.5 million people around the globe. This data will provide insights in the navigation deficits observed in AD [206]. This kind of mobile development together with the portable EEG opens the door to perform studies with portable EEG recordings during spatial navigation.

The first steps in this topic have been taken with the use of the AM rate-of-change features to analyze EEG data recorded during a spatial navigation task. The results found in this study showed that subjects who navigate using a spatial strategy presented greater theta amplitude modulation in the orbitofontral and ventromedial prefrontal cortices, supporting previous results on EEG and spatial navigation [121].

Lastly, virtual reality (VR) has been used to assist the diagnosis and cognitive training in MCI and AD patients, as it provides a high interaction level in a safe virtual environment; a review on the use of VR in the study of AD can be found in [207]. The study of EEG recordings in immersive VR applications brings new usability challenges that can be addressed with the use of portable EEG devices together with dry electrode technology. A major challenge with the use of VR and portable EEG is the presence of extra artifacts evoked by the movement of eyes, head and body; a potential strategy to remove these artifacts is the simultaneous acquisition of signals related to the origin of the artifacts in order to use them as reference for BSS methods, e.g., signals from EOG can be helpful to detect and remove artifacts related to eye movement, signals from inertial measurement units (IMUs) placed on the headset and controllers can assist to the removal of head and body movements. Within this domain, we have performed initial studies on comfortable recording of EEG, ECG and EOG signals during immersive VR experiences [125].

4. **Multimodal approach for AD study- EEG and eye-gaze tracking**: Eye-gaze tracking (EGT) devices estimate the user's gaze direction and map it into coordinates on a screen or video. This technique has been utilized for research in different fields, such as ophthalmology, neurology, psychology and marketing. In the study of AD, oculomotor system deficits have

---

[1] `http://www.seaheroquest.com/site/en/`

been explored with studies showing weakened saccades, impaired fixations, smooth pursuit dysfunction, and impaired inhibitory saccades [208, 209]. Such effects have been observed by analyzing eye movements to determine the subject's attentional patterns in response to a given stimulus. Alternatively, eye gaze can be utilized not only as diagnosis tool but also as contextual information provider. Research in cognitive psychology has found that unconscious eye movements are strongly associated with underlying mental processes, such as engagement, attention, relational memory or learning [210]. Moreover, EGT data can be used to identify, characterize and correct eye-movement-related artifacts from EEG signals. This is not only relevant for the multimodal approach EEG-EGT but also for the use of VR due to the imminent integration of EGT devices and VR headsets.

Recent works have presented diverse ways to integrate EEG-based systems such as BCIs with other modalities [41]. Among these other modalities, the use of EGT can be used as a direct input, i.e., a pointing element, or an indirect input, i.e., its role is to provide complementary contextual information about the cognitive processes in progress [122]. To the best of our knowledge, combined EEG-EGT analysis has not been used in AD diagnosis, but warrants further investigation. As a step in this direction, the MuLES software [118] has been modified to seamlessly integrate eye tracking with EEG data, thus allowing for automated tagging of EEG data based on visualization of regions of interest in a screen or on the environment. The figure below shows a screenshot of the developed program with segments of EEG labelled in real-time based on eye tracking feedback. A video demo can be found online[2].

---

[2] `https://youtu.be/nJhD1boqa8U`

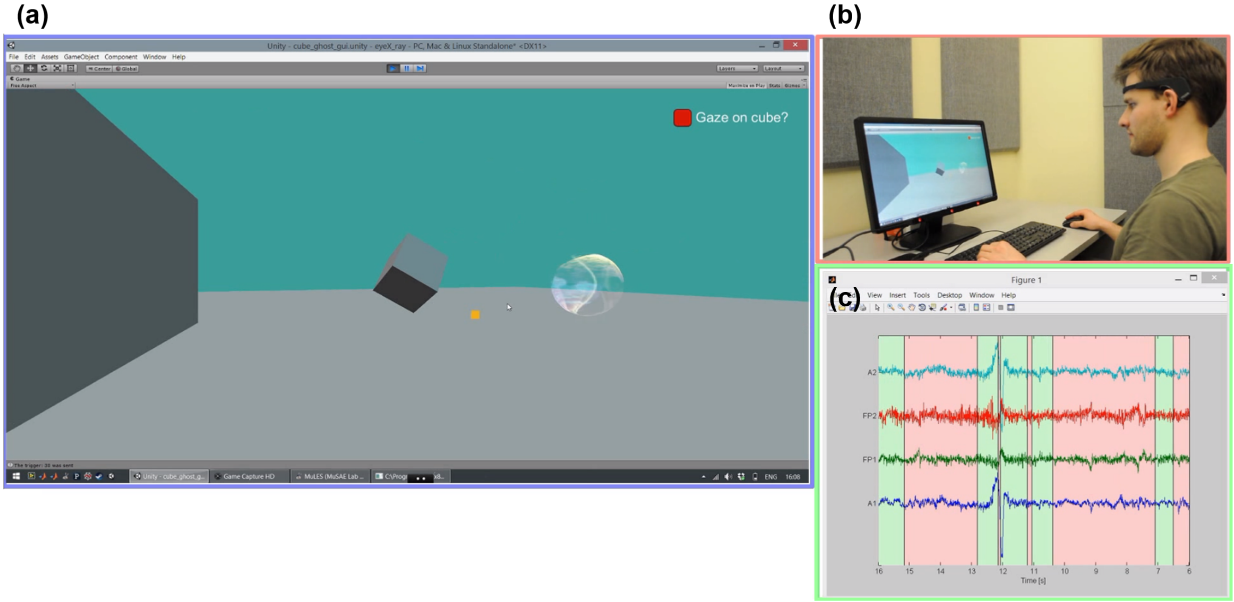

Figure 7.1 – **Real-time EEG segmentation based on eye-tracking information. (a) Screenshot of the 3D navigation task, the yellow square indicates the point of gaze. (b) Experimental setup, the remote EGT device is located at the bottom of the monitor. (c) EEG signals in time domain, where the background colors, either green or red, indicate if the subject was looking at the target (cube) or not respectively.**

7.3 Conclusion

The last decade has seen important advances in the development of EEG-based tools to assist clinicians with the diagnosis of diverse brain disorders, among them dementia due to Alzheimer's disease. Unfortunately, the use of EEG in the clinical practice is not currently part of the routine in the diagnosis and monitoring of AD. In this thesis work we identified and discussed on the major challenges of the utilization of rsEEG for the study of AD, namely, the sensibility of EEG signals to artifacts, and the lack of portability of current rsEEG devices. To address these challenges, we proposed and developed a series of studies, which experimental results are enlightening towards: (*i*) the reduction and removal of human intervention from artifact-handling process, (*ii*) the utilization of portable devices for rsEEG-based AD diagnosis, and (*iii*) the development of specific features to characterize the effects of AD on rsEEG signals. Ultimately, we hope that the innovations presented in this thesis work will boost the research and clinical use of rsEEG as a non-invasive, less expensive and potentially portable technique for the diagnosis and monitoring of AD.

Bibliography

[1] P. L. Nunez and R. Srinivasan, *Electric Fields of the Brain: The Neurophysics of EEG.* Oxford; New York: Oxford University Press, 2006.

[2] World Health Organization and others, *Dementia: A Public Health Priority.* World Health Organization, 2012.

[3] M. Prince, A. Wimo, M. Guerchet, G.-C. Ali, Y.-T. Wu, and M. Prina, "World Alzheimer Report 2015, The Global Impact of Dementia: An analysis of prevalence, incidence, cost and trends," *Alzheimer's Disease International*, p. 87, 2015.

[4] M. Prince, D. R. Bryce, and D. C. Ferri, "World Alzheimer Report 2011: The benefits of early diagnosis and intervention," *Alzheimer's Disease International*, p. 72, 2011.

[5] Alzheimer Society of Canada, "Report summary – Prevalence and monetary costs of dementia in Canada (2016): A report by the Alzheimer Society of Canada," *Health Promotion and Chronic Disease Prevention in Canada*, vol. 36, no. 10, pp. 231–232, Oct. 2016.

[6] C. R. Jack, M. S. Albert, D. S. Knopman, G. M. McKhann, R. A. Sperling, M. C. Carrillo, B. Thies, and C. H. Phelps, "Introduction to the recommendations from the National Institute on Aging-Alzheimer's Association workgroups on diagnostic guidelines for Alzheimer's disease," *Alzheimer's & Dementia: The Journal of the Alzheimer's Association*, vol. 7, no. 3, pp. 257–262, May 2011.

[7] R. A. Sperling, P. S. Aisen, L. A. Beckett, D. A. Bennett, S. Craft, A. M. Fagan, T. Iwatsubo, C. R. Jack, J. Kaye, T. J. Montine, D. C. Park, E. M. Reiman, C. C. Rowe, E. Siemers, Y. Stern, K. Yaffe, M. C. Carrillo, B. Thies, M. Morrison-Bogorad, M. V. Wagster, and C. H. Phelps, "Toward defining the preclinical stages of Alzheimer's disease: Recommendations from the National Institute on Aging-Alzheimer's Association workgroups on diagnostic guidelines for Alzheimer's disease," *Alzheimer's & Dementia: The Journal of the Alzheimer's Association*, vol. 7, no. 3, pp. 280–292, May 2011.

[8] G. M. McKhann, D. S. Knopman, H. Chertkow, B. T. Hyman, C. R. Jack, C. H. Kawas, W. E. Klunk, W. J. Koroshetz, J. J. Manly, R. Mayeux, R. C. Mohs, J. C. Morris, M. N. Rossor, P. Scheltens, M. C. Carrillo, B. Thies, S. Weintraub, and C. H. Phelps, "The diagnosis of dementia due to Alzheimer's disease: Recommendations from the National Institute on Aging-Alzheimer's Association workgroups on diagnostic guidelines for Alzheimer's disease," *Alzheimer's & Dementia: The Journal of the Alzheimer's Association*, vol. 7, no. 3, pp. 263–269, May 2011.

[9] M. S. Albert, S. T. DeKosky, D. Dickson, B. Dubois, H. H. Feldman, N. C. Fox, A. Gamst, D. M. Holtzman, W. J. Jagust, R. C. Petersen, P. J. Snyder, M. C. Carrillo, B. Thies, and C. H. Phelps, "The diagnosis of mild cognitive impairment due to Alzheimer's disease: Recommendations from the National Institute on Aging-Alzheimer's Association workgroups on diagnostic guidelines for Alzheimer's disease," *Alzheimer's & Dementia: The Journal of the Alzheimer's Association*, vol. 7, no. 3, pp. 270–279, May 2011.

[10] A. J. Mitchell, “A meta-analysis of the accuracy of the mini-mental state examination in the detection of dementia and mild cognitive impairment,” *Journal of Psychiatric Research*, vol. 43, no. 4, pp. 411–431, Jan. 2009.

[11] J. C. Morris, “The Clinical Dementia Rating (CDR): Current version and scoring rules.” *Neurology*, 1993.

[12] G. Buzsáki, C. A. Anastassiou, and C. Koch, “The origin of extracellular fields and currents — EEG, ECoG, LFP and spikes,” *Nature Reviews Neuroscience*, vol. 13, no. 6, pp. 407–420, Jun. 2012.

[13] M. Cohen, *Analyzing Neural Time Series Data: Theory and Practice.* MIT Press, 2014.

[14] C. Micanovic and S. Pal, “The diagnostic utility of EEG in early-onset dementia: A systematic review of the literature with narrative analysis,” *Journal of Neural Transmission*, vol. 121, no. 1, pp. 59–69, Jan. 2014.

[15] L. Sörnmo and P. Laguna, *Bioelectrical Signal Processing in Cardiac and Neurological Applications.* Academic Press, 2005, vol. 8.

[16] G. Rodriguez, D. Arnaldi, and A. Picco, “Brain Functional Network in Alzheimer’s Disease: Diagnostic Markers for Diagnosis and Monitoring,” *International Journal of Alzheimer’s Disease*, vol. 2011, pp. 1–10, 2011.

[17] J. Jeong, “EEG dynamics in patients with Alzheimer’s disease,” *Clinical Neurophysiology*, vol. 115, no. 7, pp. 1490–1505, Jul. 2004.

[18] C. Babiloni, C. Del Percio, A. Caroli, E. Salvatore, E. Nicolai, N. Marzano, R. Lizio, E. Cavedo, S. Landau, K. Chen, W. Jagust, E. Reiman, G. Tedeschi, P. Montella, M. De Stefano, L. Gesualdo, G. B. Frisoni, and A. Soricelli, “Cortical sources of resting state EEG rhythms are related to brain hypometabolism in subjects with Alzheimer’s disease: An EEG-PET study,” *Neurobiology of Aging*, vol. 48, pp. 122–134, Dec. 2016.

[19] I. Daly, F. Pichiorri, J. Faller, V. Kaiser, A. Kreilinger, R. Scherer, G. Müller-Putz, and others, “What does clean EEG look like?” in *Conf Proc IEEE Eng Med Biol Soc*, 2012, pp. 3963–3966.

[20] I. Daly, N. Nicolaou, S. J. Nasuto, and K. Warwick, “Automated Artifact Removal From the Electroencephalogram: A Comparative Study,” *Clinical EEG and Neuroscience*, vol. 44, no. 4, pp. 291–306, Oct. 2013.

[21] S. Lee, Y. Shin, S. Woo, K. Kim, and H.-N. Lee, “Review of Wireless Brain-Computer Interface Systems,” in *Brain-Computer Interface Systems - Recent Progress and Future Prospects*, R. Fazel-Rezai, Ed. InTech, Jun. 2013.

[22] V. Mihajlović, B. Grundlehner, R. Vullers, and J. Penders, “Wearable, Wireless EEG Solutions in Daily Life Applications: What are we missing?” *IEEE Journal of Biomedical and Health Informatics*, vol. 19, no. 1, pp. 6–21, Jan. 2015.

[23] R. Cassani, M. Estarellas, R. San-Martin, F. J. Fraga, and T. H. Falk, “Systematic Review on Resting-State EEG for Alzheimer’s Disease Diagnosis and Progression Assessment,” *Disease Markers*, vol. 2018, 2018.

[24] J. Dauwels, F. Vialatte, and A. Cichocki, “Diagnosis of Alzheimer’s Disease from EEG Signals: Where Are We Standing?” *Current Alzheimer Research*, vol. 7, no. 6, pp. 487–505, Sep. 2010.

[25] M. Waser, M. Deistler, H. Garn, T. Benke, P. Dal-Bianco, G. Ransmayr, D. Grossegger, and R. Schmidt, “EEG in the diagnostics of Alzheimer’s disease,” *Statistical Papers*, vol. 54, no. 4, pp. 1095–1107, Nov. 2013.

[26] H. Garn, M. Waser, M. Deistler, T. Benke, P. Dal-Bianco, G. Ransmayr, H. Schmidt, G. Sanin, P. Santer, G. Caravias, S. Seiler, D. Grossegger, W. Fruehwirt, and R. Schmidt, "Quantitative EEG markers relate to Alzheimer's disease severity in the Prospective Dementia Registry Austria (PRODEM)," *Clinical Neurophysiology*, vol. 126, no. 3, pp. 505–513, Mar. 2015.

[27] T. H. Ferreira-Vieira, I. M. Guimaraes, F. R. Silva, and F. M. Ribeiro, "Alzheimer's disease: Targeting the cholinergic system," *Current Neuropharmacology*, vol. 14, no. 1, pp. 101–115, 2016.

[28] C. Babiloni, R. Lizio, N. Marzano, P. Capotosto, A. Soricelli, A. I. Triggiani, S. Cordone, L. Gesualdo, and C. Del Percio, "Brain neural synchronization and functional coupling in Alzheimer's disease as revealed by resting state EEG rhythms," *International Journal of Psychophysiology*, vol. 103, pp. 88–102, May 2016.

[29] T. Koenig, L. Prichep, T. Dierks, D. Hubl, L. Wahlund, E. John, and V. Jelic, "Decreased EEG synchronization in Alzheimer's disease and mild cognitive impairment," *Neurobiology of Aging*, vol. 26, no. 2, pp. 165–171, Feb. 2005.

[30] C. Besthorn, H. Förstl, C. Geiger-Kabisch, H. Sattel, T. Gasser, and U. Schreiter-Gasser, "EEG coherence in Alzheimer disease," *Clinical Neurophysiology*, vol. 90, no. 3, pp. 242–245, 1994.

[31] G. Adler, S. Brassen, and A. Jajcevic, "EEG coherence in Alzheimer's dementia," *Journal of Neural Transmission*, vol. 110, no. 9, pp. 1051–1058, Sep. 2003.

[32] J. Jeong, S. Y. Kim, and S.-H. Han, "Non-linear dynamical analysis of the EEG in Alzheimer's disease with optimal embedding dimension," *Electroencephalography and Clinical Neurophysiology*, vol. 106, no. 3, pp. 220–228, Mar. 1998.

[33] J. Dauwels, K. Srinivasan, M. Ramasubba Reddy, T. Musha, F.-B. Vialatte, C. Latchoumane, J. Jeong, and A. Cichocki, "Slowing and Loss of Complexity in Alzheimer's EEG: Two Sides of the Same Coin?" *International Journal of Alzheimer's Disease*, vol. 2011, pp. 1–10, 2011.

[34] A. W. Laxton, D. F. Tang-Wai, M. P. McAndrews, D. Zumsteg, R. Wennberg, R. Keren, J. Wherrett, G. Naglie, C. Hamani, G. S. Smith, and A. M. Lozano, "A phase I trial of deep brain stimulation of memory circuits in Alzheimer's disease," *Annals of Neurology*, vol. 68, no. 4, pp. 521–534, Oct. 2010.

[35] N. Hansen, "Brain Stimulation for Combating Alzheimer's Disease," *Frontiers in Neurology*, vol. 5, Jun. 2014.

[36] T. H. Falk, F. J. Fraga, L. Trambaiolli, and R. Anghinah, "EEG amplitude modulation analysis for semi-automated diagnosis of Alzheimer's disease," *EURASIP Journal on Advances in Signal Processing*, vol. 2012, no. 1, pp. 1–9, 2012.

[37] C. J. Stam, "Nonlinear dynamical analysis of EEG and MEG: Review of an emerging field," *Clinical Neurophysiology*, vol. 116, no. 10, pp. 2266–2301, Oct. 2005.

[38] F. Vecchio, C. Babiloni, R. Lizio, F. D. V. Fallani, K. Blinowska, G. Verrienti, G. Frisoni, and P. M. Rossini, "Resting state cortical EEG rhythms in Alzheimer's disease: Toward EEG markers for clinical applications: A review," *Supplements to Clinical Neurophysiology*, vol. 62, pp. 223–236, 2013.

[39] C. J. Chu, "High density EEG—What do we have to lose?" *Clinical Neurophysiology*, vol. 126, no. 3, pp. 433–434, Mar. 2015.

[40] M. Lopez-Gordo, D. Sanchez-Morillo, and F. Valle, "Dry EEG Electrodes," *Sensors*, vol. 14, no. 7, pp. 12 847–12 870, Jul. 2014.

[41] H. Banville and T. Falk, "Recent advances and open challenges in hybrid brain-computer interfacing: A technological review of non-invasive human research," *Brain-Computer Interfaces*, vol. 3, no. 1, pp. 9–46, Jan. 2016.

[42] M. Fatourechi, A. Bashashati, R. K. Ward, and G. E. Birch, “EMG and EOG artifacts in brain computer interface systems: A survey,” *Clinical Neurophysiology*, vol. 118, no. 3, pp. 480–494, Mar. 2007.

[43] A. Widmann, E. Schröger, and B. Maess, “Digital filter design for electrophysiological data – a practical approach,” *Journal of Neuroscience Methods*, vol. 250, pp. 34–46, Jul. 2015.

[44] I. Daly, M. Billinger, R. Scherer, and G. Muller-Putz, “On the Automated Removal of Artifacts Related to Head Movement From the EEG,” *IEEE Transactions on Neural Systems and Rehabilitation Engineering*, vol. 21, no. 3, pp. 427–434, May 2013.

[45] J. A. Urigüen and B. n. Garcia-Zapirain, “EEG artifact removal—state-of-the-art and guidelines,” *Journal of Neural Engineering*, vol. 12, no. 3, p. 031001, Jun. 2015.

[46] K. T. Sweeney, T. E. Ward, and S. F. McLoone, “Artifact Removal in Physiological Signals—Practices and Possibilities,” *IEEE Transactions on Information Technology in Biomedicine*, vol. 16, no. 3, pp. 488–500, May 2012.

[47] M. M. N. Mannan, M. A. Kamran, and M. Y. Jeong, “Identification and Removal of Physiological Artifacts from Electroencephalogram Signals: A Review,” *IEEE Access*, pp. 30 630–30 652, 2018.

[48] M. A. Jatoi, N. Kamel, A. S. Malik, I. Faye, and T. Begum, “A survey of methods used for source localization using EEG signals,” *Biomedical Signal Processing and Control*, vol. 11, pp. 42–52, May 2014.

[49] C. M. Michel, *Electrical Neuroimaging.* Cambridge; New York: Cambridge University Press, 2009.

[50] S. Sanei and J. Chambers, *EEG Signal Processing.* Chichester, England; Hoboken, NJ: John Wiley & Sons, 2007.

[51] F. Lotte, L. Bougrain, A. Cichocki, M. Clerc, M. Congedo, A. Rakotomamonjy, and F. Yger, “A review of classification algorithms for EEG-based brain–computer interfaces: A 10 year update,” *Journal of Neural Engineering*, vol. 15, no. 3, p. 031005, Jun. 2018.

[52] L. R. Trambaiolli, N. Spolaor, A. C. Lorena, R. Anghinah, and J. R. Sato, “Feature selection before EEG classification supports the diagnosis of Alzheimer’s disease,” *CLINICAL NEUROPHYSIOLOGY*, vol. 128, no. 10, pp. {2058–2067}, Oct. 2017.

[53] A. Leon-Garcia, *Probability, Statistics, and Random Processes for Electrical Engineering.* Pearson Education, 2017.

[54] D. V. Moretti, D. PaternicoG, G. Binetti, O. Zanetti, and G. B. Frisoni, “Analysis of Grey Matter in Thalamus and Basal Ganglia Based on EEG $a3/a2$ Frequency Ratio Reveals Specific Changes in Subjects with Mild Cognitive Impairment,” *ASN Neuro*, vol. 4, no. 7, p. AN20120058, Nov. 2012.

[55] S. Makeig and J. Onton, “ERP features and EEG dynamics: An ICA perspective,” *S., Luck, E. Kappenman,(Eds.), Oxford handbook of event-related potential components*, pp. 51–88, 2011.

[56] S. J. Luck and E. S. Kappenman, *The Oxford Handbook of Event-Related Potential Components.* Oxford University Press, 2011.

[57] P. Herman, G. Prasad, T. McGinnity, and D. Coyle, “Comparative Analysis of Spectral Approaches to Feature Extraction for EEG-Based Motor Imagery Classification,” *IEEE Transactions on Neural Systems and Rehabilitation Engineering*, vol. 16, no. 4, pp. 317–326, Aug. 2008.

[58] S. Motamedi-Fakhr, M. Moshrefi-Torbati, M. Hill, C. M. Hill, and P. R. White, "Signal processing techniques applied to human sleep EEG signals—A review," *Biomedical Signal Processing and Control*, vol. 10, pp. 21–33, Mar. 2014.

[59] O. Faust, U. R. Acharya, H. Adeli, and A. Adeli, "Wavelet-based EEG processing for computer-aided seizure detection and epilepsy diagnosis," *Seizure*, vol. 26, pp. 56–64, Mar. 2015.

[60] D.-H. Jeong, Y.-D. Kim, I.-U. Song, Y.-A. Chung, and J. Jeong, "Wavelet Energy and Wavelet Coherence as EEG Biomarkers for the Diagnosis of Parkinson's Disease-Related Dementia and Alzheimer's Disease," *Entropy*, vol. 18, no. 1, p. 8, Dec. 2015.

[61] P. Ghorbanian, D. M. Devilbiss, T. Hess, A. Bernstein, A. J. Simon, and H. Ashrafiuon, "Exploration of EEG features of Alzheimer's disease using continuous wavelet transform," *Medical & Biological Engineering & Computing*, vol. 53, no. 9, pp. 843–855, Sep. 2015.

[62] O. Vyšata, M. Vališ, A. Procházka, R. Rusina, and L. Pazdera, "Linear and Nonlinear EEG Synchronization in Alzheimer's Disease," *Neurophysiology*, vol. 47, no. 1, pp. 46–52, Feb. 2015.

[63] Z. Sankari, H. Adeli, and A. Adeli, "Wavelet Coherence Model for Diagnosis of Alzheimer Disease," *Clinical EEG and Neuroscience*, vol. 43, no. 4, pp. 268–278, Oct. 2012.

[64] F.-B. Vialatte, J. Dauwels, M. Maurice, T. Musha, and A. Cichocki, "Improving the Specificity of EEG for Diagnosing Alzheimer's Disease," *International Journal of Alzheimer's Disease*, vol. 2011, pp. 1–7, 2011.

[65] J. Dauwels, F. Vialatte, T. Musha, and A. Cichocki, "A comparative study of synchrony measures for the early diagnosis of Alzheimer's disease based on EEG," *NeuroImage*, vol. 49, no. 1, pp. 668–693, Jan. 2010.

[66] F. Vialatte, A. Cichocki, G. Dreyfus, T. Musha, S. L. Shishkin, and R. Gervais, "Early Detection of Alzheimer's Disease by Blind Source Separation, Time Frequency Representation, and Bump Modeling of EEG Signals," in *Artificial Neural Networks: Biological Inspirations – ICANN 2005*. Berlin, Heidelberg: Springer Berlin Heidelberg, 2005, pp. 683–692.

[67] A. T. Bondar' and A. I. Fedotchev, "Concerning the amplitude modulation of the human EEG," *Human Physiology*, vol. 26, no. 4, pp. 393–399, Jul. 2000.

[68] K. Linkenkaer-Hansen, V. V. Nikouline, J. M. Palva, and R. J. Ilmoniemi, "Long-range temporal correlations and scaling behavior in human brain oscillations," *Journal of Neuroscience*, vol. 21, no. 4, pp. 1370–1377, 2001.

[69] D. Purves, *Neuroscience*. Sinauer Associates, Incorporated, 2012.

[70] E. Başar and A. Düzgün, "How is the brain working?" *International Journal of Psychophysiology*, vol. 103, pp. 3–11, May 2016.

[71] F. J. Fraga, T. H. Falk, P. A. M. Kanda, and R. Anghinah, "Characterizing Alzheimer's Disease Severity via Resting-Awake EEG Amplitude Modulation Analysis," *PLoS ONE*, vol. 8, no. 8, p. e72240, Aug. 2013.

[72] G. McKhann, D. Drachman, M. Folstein, R. Katzman, D. Price, and E. Stadlan, "Clinical diagnosis of alzheimer's disease: Report of the NINCDS-ADRDA work group$\star$ under the auspices of department of health and human services task force on alzheimer's disease," *Neurology*, vol. 34, no. 7, pp. 939–944, 1984.

[73] S. Brucki, R. Nitrini, P. Caramelli, P. H. Bertolucci, and I. H. Okamoto, "Suggestions for utilization of the mini-mental state examination in Brazil," *Arquivos de neuro-psiquiatria*, vol. 61, no. 3B, pp. 777–781, 2003.

[74] C. Lehmann, T. Koenig, V. Jelic, L. Prichep, R. E. John, L.-O. Wahlund, Y. Dodge, and T. Dierks, “Application and comparison of classification algorithms for recognition of Alzheimer’s disease in electrical brain activity (EEG),” *Journal of Neuroscience Methods*, vol. 161, no. 2, pp. 342–350, Apr. 2007.

[75] L. R. Trambaiolli, A. C. Lorena, F. J. Fraga, P. A. M. K. Kanda, R. Nitrini, and R. Anghinah, “Does EEG Montage Influence Alzheimer’s Disease Electroclinic Diagnosis?” *International Journal of Alzheimer’s Disease*, vol. 2011, pp. 1–6, 2011.

[76] F. J. Fraga, T. H. Falk, L. R. Trambaiolli, E. F. Oliveira, W. H. L. Pinaya, P. A. M. Kanda, and R. Anghinah, “Towards an EEG-based biomarker for Alzheimer’s disease: Improving amplitude modulation analysis features,” in *2013 IEEE International Conference on Acoustics, Speech and Signal Processing (ICASSP)*, May 2013, pp. 1207–1211.

[77] G. Gómez-Herrero, W. De Clercq, H. Anwar, O. Kara, K. Egiazarian, S. Van Huffel, and W. Van Paesschen, “Automatic removal of ocular artifacts in the EEG without an EOG reference channel,” in *Signal Processing Symposium, 2006. NORSIG 2006. Proceedings of the 7th Nordic.* IEEE, 2006, pp. 130–133.

[78] M. E. Tipping, “Sparse Bayesian Learning and the Relevance Vector Machine,” *J. Mach. Learn. Res.*, vol. 1, pp. 211–244, Sep. 2001.

[79] B. Byrom, M. McCarthy, P. Schueler, and W. Muehlhausen, “Brain Monitoring Devices in Neuroscience Clinical Research: The Potential of Remote Monitoring Using Sensors, Wearables, and Mobile Devices,” *Clinical Pharmacology & Therapeutics*, vol. 104, no. 1, pp. 59–71, Jul. 2018.

[80] M. Cecchi, D. K. Moore, C. H. Sadowsky, P. R. Solomon, P. M. Doraiswamy, C. D. Smith, G. A. Jicha, A. E. Budson, S. E. Arnold, and K. C. Fadem, “A clinical trial to validate event-related potential markers of Alzheimer’s disease in outpatient settings,” *Alzheimer’s & Dementia: Diagnosis, Assessment & Disease Monitoring*, vol. 1, no. 4, pp. 387–394, Dec. 2015.

[81] J. Zhu, S. Rosset, R. Tibshirani, and T. J. Hastie, “1-norm Support Vector Machines,” *Advances in Neural Information Processing Systems 16*, pp. 49–56, 2004.

[82] F. Pedregosa, G. Varoquaux, A. Gramfort, V. Michel, B. Thirion, O. Grisel, M. Blondel, P. Prettenhofer, R. Weiss, V. Dubourg, J. Vanderplas, A. Passos, D. Cournapeau, M. Brucher, M. Perrot, and E. Duchesnay, “Scikit-learn: Machine Learning in Python,” *J. Mach. Learn. Res.*, vol. 12, pp. 2825–2830, Nov. 2011.

[83] H. Abdi, “The Bonferonni and Šidák corrections for multiple comparisons,” *Encyclopedia of measurement and statistics*, vol. 3, pp. 103–107, 2007.

[84] J. A. Deursen, E. F. P. M. Vuurman, F. R. J. Verhey, V. H. J. M. Kranen-Mastenbroek, and W. J. Riedel, “Increased EEG gamma band activity in Alzheimer’s disease and mild cognitive impairment,” *Journal of Neural Transmission*, vol. 115, no. 9, pp. 1301–1311, Jul. 2008.

[85] D. V. Moretti, C. Fracassi, M. Pievani, C. Geroldi, G. Binetti, O. Zanetti, K. Sosta, P. M. Rossini, and G. B. Frisoni, “Increase of theta/gamma ratio is associated with memory impairment,” *Clinical Neurophysiology*, vol. 120, no. 2, pp. 295–303, Feb. 2009.

[86] C. Stam, C. v. W. Van, Y. Pijnenburg, H. Berendse, M. De, P. Scheltens, and D. Van, “Generalized synchronization of MEG recordings in Alzheimer’s disease: Evidence for involvement of the gamma band,” *Journal of Clinical Neurophysiology*, vol. 19, no. 6, pp. 562–574, 2002.

[87] R. Lizio, F. Vecchio, G. B. Frisoni, R. Ferri, G. Rodriguez, and C. Babiloni, “Electroencephalographic Rhythms in Alzheimer’s Disease,” *International Journal of Alzheimer’s Disease*, vol. 2011, pp. 1–11, 2011.

[88] M. Elgendi, F. Vialatte, A. Cichocki, C. Latchoumane, Jaesung Jeong, and J. Dauwels, "Optimization of EEG frequency bands for improved diagnosis of Alzheimer disease," in *2011 Annual International Conference of the IEEE Engineering in Medicine and Biology Society*. IEEE, Aug. 2011, pp. 6087–6091.

[89] E. Gallego-Jutglà, J. Solé-Casals, F.-B. Vialatte, M. Elgendi, A. Cichocki, and J. Dauwels, "A hybrid feature selection approach for the early diagnosis of Alzheimer's disease," *Journal of Neural Engineering*, vol. 12, no. 1, p. 016018, Feb. 2015.

[90] R. Cassani, T. H. Falk, F. J. Fraga, P. A. Kanda, and R. Anghinah, "Towards automated EEG-Based Alzheimer's disease diagnosis using relevance vector machines," in *5th ISSNIP-IEEE Biosignals and Biorobotics Conference (2014): Biosignals and Robotics for Better and Safer Living (BRC)*, May 2014, pp. 1–6.

[91] V. Bewick, L. Cheek, and J. Ball, "Statistics review 13: Receiver operating characteristic curves," *Critical care*, vol. 8, no. 6, p. 5, 2004.

[92] A. Alberdi, A. Aztiria, and A. Basarab, "On the early diagnosis of Alzheimer's Disease from multimodal signals: A survey," *Artificial Intelligence in Medicine*, vol. 71, pp. 1–29, Jul. 2016.

[93] C. R. Jack, D. S. Knopman, W. J. Jagust, L. M. Shaw, P. S. Aisen, M. W. Weiner, R. C. Petersen, and J. Q. Trojanowski, "Hypothetical model of dynamic biomarkers of the Alzheimer's pathological cascade," *The Lancet Neurology*, vol. 9, no. 1, pp. 119–128, Jan. 2010.

[94] D. Galimberti and E. Scarpini, "Disease-modifying treatments for Alzheimer's disease," *Therapeutic Advances in Neurological Disorders*, vol. 4, no. 4, pp. 203–216, Jul. 2011.

[95] B. Dubois, H. Hampel, H. H. Feldman, P. Scheltens, P. Aisen, S. Andrieu, H. Bakardjian, H. Benali, L. Bertram, K. Blennow, K. Broich, E. Cavedo, S. Crutch, J.-F. Dartigues, C. Duyckaerts, S. Epelbaum, G. B. Frisoni, S. Gauthier, R. Genthon, A. A. Gouw, M.-O. Habert, D. M. Holtzman, M. Kivipelto, S. Lista, J.-L. Molinuevo, S. E. O'Bryant, G. D. Rabinovici, C. Rowe, S. Salloway, L. S. Schneider, R. Sperling, M. Teichmann, M. C. Carrillo, J. Cummings, and C. R. Jack, "Preclinical Alzheimer's disease: Definition, natural history, and diagnostic criteria," *Alzheimer's & Dementia*, vol. 12, no. 3, pp. 292–323, Mar. 2016.

[96] R. Sperling, E. Mormino, and K. Johnson, "The Evolution of Preclinical Alzheimer's Disease: Implications for Prevention Trials," *Neuron*, vol. 84, no. 3, pp. 608–622, Nov. 2014.

[97] B. Dubois, H. H. Feldman, C. Jacova, S. T. DeKosky, P. Barberger-Gateau, J. Cummings, A. Delacourte, D. Galasko, S. Gauthier, G. Jicha, K. Meguro, J. O'Brien, F. Pasquier, P. Robert, M. Rossor, S. Salloway, Y. Stern, P. J. Visser, and P. Scheltens, "Research criteria for the diagnosis of Alzheimer's disease: Revising the NINCDS–ADRDA criteria," *The Lancet Neurology*, vol. 6, no. 8, pp. 734–746, Aug. 2007.

[98] C. R. Jack, D. A. Bennett, K. Blennow, M. C. Carrillo, B. Dunn, S. B. Haeberlein, D. M. Holtzman, W. Jagust, F. Jessen, J. Karlawish, E. Liu, J. L. Molinuevo, T. Montine, C. Phelps, K. P. Rankin, C. C. Rowe, P. Scheltens, E. Siemers, H. M. Snyder, R. Sperling, C. Elliott, E. Masliah, L. Ryan, and N. Silverberg, "NIA-AA Research Framework: Toward a biological definition of Alzheimer's disease," *Alzheimer's & Dementia*, vol. 14, no. 4, pp. 535–562, Apr. 2018.

[99] B. Olsson, R. Lautner, U. Andreasson, A. Öhrfelt, E. Portelius, M. Bjerke, M. Hölttä, C. Rosén, C. Olsson, G. Strobel, E. Wu, K. Dakin, M. Petzold, K. Blennow, and H. Zetterberg, "CSF and blood biomarkers for the diagnosis of Alzheimer's disease: A systematic review and meta-analysis," *The Lancet Neurology*, vol. 15, no. 7, pp. 673–684, Jun. 2016.

[100] B. Barua, "Waiting Your Turn: Wait Times for Health Care in Canada, 2017 Report," Fraser Institute, Tech. Rep., 2017.

[101] C. Piano, E. Mazzucchi, A. R. Bentivoglio, A. Losurdo, G. Calandra Buonaura, C. Imperatori, P. Cortelli, and G. Della Marca, "Wake and sleep EEG in patients with Huntington disease: An eLORETA study and review of the literature," *Clinical EEG and neuroscience*, vol. 48, no. 1, pp. 60–71, 2017.

[102] J. Wang, J. Barstein, L. E. Ethridge, M. W. Mosconi, Y. Takarae, and J. A. Sweeney, "Resting state EEG abnormalities in autism spectrum disorders," *Journal of neurodevelopmental disorders*, vol. 5, no. 1, p. 24, 2013.

[103] C. F. Muniz, A. V. Shenoy, K. L. O'Connor, S. C. Bechek, E. J. Boyle, M. M. Guanci, T. M. Tehan, S. F. Zafar, A. J. Cole, A. B. Patel, M. B. Westover, and E. S. Rosenthal, "Clinical Development and Implementation of an Institutional Guideline for Prospective EEG Monitoring and Reporting of Delayed Cerebral Ischemia:," *Journal of Clinical Neurophysiology*, vol. 33, no. 3, pp. 217–226, Jun. 2016.

[104] B. Graimann, G. Pfurtscheller, and B. Allison, *Brain-Computer Interfaces : Revolutionizing Human-Computer Interaction*, ser. The Frontiers Collection. Berlin, Heidelberg: Springer-Verlag Berlin Heidelberg, 2010.

[105] V. Jurcak, D. Tsuzuki, and I. Dan, "10/20, 10/10, and 10/5 systems revisited: Their validity as relative head-surface-based positioning systems," *NeuroImage*, vol. 34, no. 4, pp. 1600–1611, Feb. 2007.

[106] C. Babiloni, A. I. Triggiani, R. Lizio, S. Cordone, G. Tattoli, V. Bevilacqua, A. Soricelli, R. Ferri, F. Nobili, L. Gesualdo, J. C. Millán-Calenti, A. Buján, R. Tortelli, V. Cardinali, M. R. Barulli, A. Giannini, P. Spagnolo, S. Armenise, G. Buenza, G. Scianatico, G. Logroscino, G. B. Frisoni, and C. del Percio, "Classification of Single Normal and Alzheimer's Disease Individuals from Cortical Sources of Resting State EEG Rhythms," *Frontiers in Neuroscience*, vol. 10, Feb. 2016.

[107] E. Başar, C. Başar-Eroğlu, B. Güntekin, and G. G. Yener, "Brain's alpha, beta, gamma, delta, and theta oscillations in neuropsychiatric diseases," in *Supplements to Clinical Neurophysiology*. Elsevier, 2013, vol. 62, pp. 19–54.

[108] C. Başar-Eroglu, D. Strüber, M. Schürmann, M. Stadler, and E. Başar, "Gamma-band responses in the brain: A short review of psychophysiological correlates and functional significance," *International Journal of Psychophysiology*, vol. 24, no. 1-2, pp. 101–112, Nov. 1996.

[109] C. S. Herrmann, M. H. Munk, and A. K. Engel, "Cognitive functions of gamma-band activity: Memory match and utilization," *Trends in Cognitive Sciences*, vol. 8, no. 8, pp. 347–355, Aug. 2004.

[110] F. J. Fraga, L. A. Ferreira, T. H. Falk, E. Johns, and N. D. Phillips, "Event-related synchronisation responses to N-back memory tasks discriminate between healthy ageing, mild cognitive impairment, and mild Alzheimer's disease," in *2017 IEEE International Conference on Acoustics, Speech and Signal Processing (ICASSP)*. IEEE, Mar. 2017, pp. 964–968.

[111] G. G. Yener and E. Basar, "Biomarkers in Alzheimer's disease with a special emphasis on event-related oscillatory responses," *Suppl. Clin. Neurophysiol*, vol. 62, pp. 237–273, 2013.

[112] D. Hedges, R. Janis, S. Mickelson, C. Keith, D. Bennett, and B. L. Brown, "P300 Amplitude in Alzheimer's Disease: A Meta-Analysis and Meta-Regression," *Clinical EEG and neuroscience*, vol. 47, no. 1, pp. 48–55, 2016.

[113] P. Ghorbanian, D. M. Devilbiss, A. Verma, A. Bernstein, T. Hess, A. J. Simon, and H. Ashrafiuon, "Identification of Resting and Active State EEG Features of Alzheimer's Disease using Discrete Wavelet Transform," *Annals of Biomedical Engineering*, vol. 41, no. 6, pp. 1243–1257, Mar. 2013.

[114] What Are the Signs of Alzheimer's Disease? http://www.nia.nih.gov/health/what-are-signs-alzheimers-disease.

[115] R. Cassani, T. H. Falk, F. J. Fraga, P. A. M. Kanda, and R. Anghinah, "The effects of automated artifact removal algorithms on electroencephalography-based Alzheimer's disease diagnosis," *Frontiers in Aging Neuroscience*, vol. 6, p. 55, 2014.

[116] R. Cassani, T. H. Falk, F. J. Fraga, M. Cecchi, D. K. Moore, and R. Anghinah, "Towards automated electroencephalography-based Alzheimer's disease diagnosis using portable low-density devices," *Biomedical Signal Processing and Control*, vol. 33, pp. 261–271, Mar. 2017.

[117] R. Cassani and T. H. Falk, "Towards new spectrotemporal features for resting-state EEG for Alzheimer's disease diagnosis," 2018, in preparation, to be submitted to IEEE Transactions on Neural Systems and Rehabilitation Engineering.

[118] R. Cassani, H. Banville, and T. H. Falk, "MuLES: An Open Source EEG Acquisition and Streaming Server for Quick and Simple Prototyping and Recording," in *Proceedings of the 20th International Conference on Intelligent User Interfaces Companion*, ser. IUI Companion '15. Atlanta, Georgia, USA: ACM, 2015, pp. 9–12.

[119] R. Cassani and T. H. Falk, "Automated Alzheimer's Disease Diagnosis Using a Portable 7-Channel Electroencephalography Device," in *IUPESM World Congress: Abstracts*, Toronto, 2015.

[120] R. Cassani and T. H. Falk, "Spectrotemporal Modeling of Biomedical Signals: Theoretical Foundation and Applications," in *Reference Module in Biomedical Sciences.* Elsevier, 2018.

[121] T. H. Falk, H. Banville, S. Bishundayal, R. Cassani, A. Clerico, L. Dahmani, R. Gupta, A. Ratnarajah, N. Phillips, and V. D. Bohbot, "EEG-theta modulation is greater in spatial learners than response learners: A scalp-EEG study in young adults tested on a virtual navigation task," in *Neuroscience 2014*, 2014.

[122] R. Cassani and T. H. Falk, "Gaze and BCIs as Gaming Inputs: Opportunities and Open Challenges," in *EyePlay Workshop, CHI-PLAY2014*, 2014, p. 4.

[123] M. Estarellas, R. Cassani, and T. H. Falk, "Assessment of EEG-based biomarkers of Alzheimer's disease progression," in *Mechanisms, Clinical Strategies, and Promising Treatments of Neurodegenerative Diseases. 13th International Conference AD/PDTM Vienna, Austria, March 29 to April 2, 2017: Abstracts.* Vienna, Austria: Neurodegenerative Diseases, 2017.

[124] R. Cassani, S. Narayanan, and T. H. Falk, "Respiration Rate Estimation From Noisy Electrocardiograms Based on Modulation Spectral Analysis," in *CMBES Proceedings*, vol. 41, 2018.

[125] R. Cassani, M.-A. Moinnereau, and T. H. Falk, "A Neurophysiological Sensor-Equipped Head-Mounted Display for Instrumental QoE Assessment of Immersive Multimedia," in *2018 Tenth International Conference on Quality of Multimedia Experience (QoMEX)*, May 2018.

[126] L. R. Trambaiolli, R. Cassani, C. E. Biazoli Jr, A. M. Cravo, J. a. R. Sato, and T. H. Falk, "Resting-Awake EEG Amplitude Modulation Can Predict Performance of an fNIRS-Based Neurofeedback Task," in *2018 IEEE International Conference on Systems, Man, and Cybernetics (SMC)*, Oct. 2018.

[127] K. Bennys, G. Rondouin, C. Vergnes, and J. Touchon, "Diagnostic value of quantitative EEG in Alzheimer's disease," *Neurophysiologie Clinique/Clinical Neurophysiology*, vol. 31, no. 3, pp. 153–160, Jun. 2001.

[128] J. Dauwels, F.-B. Vialatte, and A. Cichocki, "On the Early Diagnosis of Alzheimer's Disease from EEG Signals: A Mini-Review," in *Advances in Cognitive Neurodynamics (II)*, R. Wang and F. Gu, Eds. Dordrecht: Springer Netherlands, 2011, pp. 709–716.

[129] S. J. M. Smith, "EEG in neurological conditions other than epilepsy: When does it help, what does it add?" *Journal of Neurology, Neurosurgery & Psychiatry*, vol. 76, no. suppl_2, pp. ii8–ii12, Jun. 2005.

[130] L. F. M. Scinto and K. R. Daffner, Eds., *Early Diagnosis of Alzheimer's Disease*, ser. Current clinical neurology. Totowa, N.J: Humana Press, 2000.

[131] E. C. Ifeachor and B. W. Jervis, *Digital Signal Processing: A Practical Approach.* Pearson Education, 2002.

[132] T. P. Jung, S. Makeig, C. Humphries, T. W. Lee, M. J. McKeown, V. Iragui, and T. J. Sejnowski, "Removing electroencephalographic artifacts by blind source separation," *Psychophysiology*, vol. 37, no. 2, pp. 163–178, Mar. 2000.

[133] S. Choi, A. Cichocki, H.-M. Park, and S.-Y. Lee, "Blind Source Separation and Independent Component Analysis: A Review," *Neural Information Processing*, p. 57, 2005.

[134] C. J. James and C. W. Hesse, "Independent component analysis for biomedical signals," *Physiological Measurement*, vol. 26, no. 1, pp. R15–R39, Feb. 2005.

[135] S. P. Fitzgibbon, D. M. W. Powers, K. J. Pope, and C. R. Clark, "Removal of EEG Noise and Artifact Using Blind Source Separation:," *Journal of Clinical Neurophysiology*, vol. 24, no. 3, pp. 232–243, Jun. 2007.

[136] T. D. Lagerlund, F. W. Sharbrough, and N. E. Busacker, "Spatial filtering of multichannel electroencephalographic recordings through principal component analysis by singular value decomposition," *Journal of clinical neurophysiology*, vol. 14, no. 1, pp. 73–82, 1997.

[137] A. Belouchrani, K. Abed-Meraim, J.-F. Cardoso, and E. Moulines, "A blind source separation technique using second-order statistics," *IEEE Transactions on Signal Processing*, vol. 45, no. 2, pp. 434–444, Feb./1997.

[138] A. Hyvärinen, P. O. Hoyer, and M. Inki, "Topographic independent component analysis," *Neural computation*, vol. 13, no. 7, pp. 1527–1558, 2001.

[139] W. D. Clercq, A. Vergult, B. Vanrumste, W. Van Paesschen, and S. Van Huffel, "Canonical Correlation Analysis Applied to Remove Muscle Artifacts From the Electroencephalogram," *IEEE Transactions on Biomedical Engineering*, vol. 53, no. 12, pp. 2583–2587, Nov. 2006.

[140] N. P. Castellanos and V. A. Makarov, "Recovering EEG brain signals: Artifact suppression with wavelet enhanced independent component analysis," *Journal of Neuroscience Methods*, vol. 158, no. 2, pp. 300–312, Dec. 2006.

[141] A. Delorme, T. Sejnowski, and S. Makeig, "Enhanced detection of artifacts in EEG data using higher-order statistics and independent component analysis," *NeuroImage*, vol. 34, no. 4, pp. 1443–1449, Feb. 2007.

[142] D. P. He, G. Wilson, and C. Russell, "Removal of ocular artifacts from electro-encephalogram by adaptive filtering," *Medical and Biological Engineering and Computing*, vol. 42, no. 3, pp. 407–412, May 2004.

[143] V. Krishnaveni, S. Jayaraman, L. Anitha, and K. Ramadoss, "Removal of ocular artifacts from EEG using adaptive thresholding of wavelet coefficients," *Journal of Neural Engineering*, vol. 3, no. 4, pp. 338–346, Dec. 2006.

[144] T. Zikov, S. Bibian, G. A. Dumont, M. Huzmezan, and C. Ries, "A wavelet based denoising technique for ocular artifact correction of the electroencephalogram," in *Engineering in Medicine and Biology, 2002. 24th Annual Conference and the Annual Fall Meeting of the Biomedical Engineering Society EMBS/BMES Conference, 2002. Proceedings of the Second Joint*, vol. 1. IEEE, 2002, pp. 98–105.

[145] A. Mognon, J. Jovicich, L. Bruzzone, and M. Buiatti, "ADJUST: An automatic EEG artifact detector based on the joint use of spatial and temporal features," *Psychophysiology*, vol. 48, no. 2, pp. 229–240, Feb. 2011.

[146] H. Nolan, R. Whelan, and R. B. Reilly, “FASTER: Fully Automated Statistical Thresholding for EEG artifact Rejection,” *Journal of Neuroscience Methods*, vol. 192, no. 1, pp. 152–162, Sep. 2010.

[147] R. D. Pascual-Marqui, C. M. Michel, and D. Lehmann, “Low resolution electromagnetic tomography: A new method for localizing electrical activity in the brain,” *International Journal of psychophysiology*, vol. 18, no. 1, pp. 49–65, 1994.

[148] R. D. Pascual-Marqui and others, “Standardized low-resolution brain electromagnetic tomography (sLORETA): Technical details,” *Methods Find Exp Clin Pharmacol*, vol. 24, no. Suppl D, pp. 5–12, 2002.

[149] R. D. Pascual-Marqui, “Discrete, 3D distributed, linear imaging methods of electric neuronal activity. Part 1: Exact, zero error localization,” *arXiv preprint arXiv:0710.3341*, 2007.

[150] M. A. Jatoi, N. Kamel, A. S. Malik, and I. Faye, “EEG based brain source localization comparison of sLORETA and eLORETA,” *Australasian Physical & Engineering Sciences in Medicine*, vol. 37, no. 4, pp. 713–721, Dec. 2014.

[151] A. M. Bastos and J.-M. Schoffelen, “A Tutorial Review of Functional Connectivity Analysis Methods and Their Interpretational Pitfalls,” *Frontiers in Systems Neuroscience*, vol. 9, Jan. 2016.

[152] R. Quian Quiroga, A. Kraskov, T. Kreuz, and P. Grassberger, “Performance of different synchronization measures in real data: A case study on electroencephalographic signals,” *Physical Review E*, vol. 65, no. 4, Mar. 2002.

[153] D. Wen, Y. Zhou, and X. Li, “A Critical Review: Coupling and Synchronization Analysis Methods of EEG Signal with Mild Cognitive Impairment,” *Frontiers in Aging Neuroscience*, vol. 7, Apr. 2015.

[154] G. Nolte, O. Bai, L. Wheaton, Z. Mari, S. Vorbach, and M. Hallett, “Identifying true brain interaction from EEG data using the imaginary part of coherency,” *Clinical Neurophysiology*, vol. 115, no. 10, pp. 2292–2307, Oct. 2004.

[155] C. Coronel, H. Garn, M. Waser, M. Deistler, T. Benke, P. Dal-Bianco, G. Ransmayr, S. Seiler, D. Grossegger, and R. Schmidt, “Quantitative EEG Markers of Entropy and Auto Mutual Information in Relation to MMSE Scores of Probable Alzheimer’s Disease Patients,” *Entropy*, vol. 19, no. 3, p. 130, Mar. 2017.

[156] N. Houmani, G. Dreyfus, and F. B. Vialatte, “Epoch-based Entropy for Early Screening of Alzheimer’s Disease,” *International Journal of Neural Systems*, vol. 25, no. 08, p. 1550032, Dec. 2015.

[157] J. C. McBride, X. Zhao, N. B. Munro, C. D. Smith, G. A. Jicha, L. Hively, L. S. Broster, F. A. Schmitt, R. J. Kryscio, and Y. Jiang, “Spectral and complexity analysis of scalp EEG characteristics for mild cognitive impairment and early Alzheimer’s disease,” *Computer Methods and Programs in Biomedicine*, vol. 114, no. 2, pp. 153–163, Apr. 2014.

[158] S.-S. Poil, W. de Haan, W. M. van der Flier, H. D. Mansvelder, P. Scheltens, and K. Linkenkaer-Hansen, “Integrative EEG biomarkers predict progression to Alzheimer’s disease at the MCI stage,” *Frontiers in Aging Neuroscience*, vol. 5, 2013.

[159] I. H. Witten, E. Frank, M. A. Hall, and C. J. Pal, *Data Mining: Practical Machine Learning Tools and Techniques.* Morgan Kaufmann, 2016.

[160] F. Lotte, M. Congedo, A. Lécuyer, F. Lamarche, and B. Arnaldi, “A review of classification algorithms for EEG-based brain–computer interfaces,” *Journal of Neural Engineering*, vol. 4, no. 2, pp. R1–R13, Jun. 2007.

[161] W. A. Gardner, “Exploitation of spectral redundancy in cyclostationary signals,” *IEEE Signal Processing Magazine*, vol. 8, no. 2, pp. 14–36, Apr. 1991.

[162] L. Atlas and S. A. Shamma, “Joint acoustic and modulation frequency,” *EURASIP Journal on Advances in Signal Processing*, vol. 2003, no. 7, p. 310290, 2003.

[163] B. Picinbono, “On instantaneous amplitude and phase of signals,” *IEEE Transactions on signal processing*, vol. 45, no. 3, pp. 552–560, 1997.

[164] F. G. Stremler, “Introduction to communication systems,” *Introduction to Communication Systems, 3rd edition by Ferrel G. Stremler, 3rd edition, Addison-Wesley, 770 p., ISBN: 0201184982*, 1990.

[165] R. E. Thomson and W. J. Emery, *Data Analysis Methods in Physical Oceanography.* Newnes, 2014.

[166] T. H. Falk, C. Zheng, and W.-Y. Chan, “A Non-Intrusive Quality and Intelligibility Measure of Reverberant and Dereverberated Speech,” *IEEE Transactions on Audio, Speech, and Language Processing*, vol. 18, no. 7, pp. 1766–1774, Sep. 2010.

[167] J. a. F. Santos and T. H. Falk, “Updating the SRMR-CI metric for improved intelligibility prediction for cochlear implant users,” *IEEE/ACM Transactions on Audio, Speech and Language Processing (TASLP)*, vol. 22, no. 12, pp. 2197–2206, 2014.

[168] M. Sarria-Paja and T. H. Falk, “Whispered speech detection in noise using auditory-inspired modulation spectrum features,” *IEEE Signal Processing Letters*, vol. 20, no. 8, pp. 783–786, 2013.

[169] D. P. Tobon V., T. H. Falk, and M. Maier, “MS-QI: A Modulation Spectrum-Based ECG Quality Index for Telehealth Applications,” *IEEE Transactions on Biomedical Engineering*, vol. 63, no. 8, pp. 1613–1622, Aug. 2016.

[170] D. Tobon Vallejo and T. Falk, “Adaptive Spectro-Temporal Filtering for Electrocardiogram Signal Enhancement,” *IEEE Journal of Biomedical and Health Informatics*, pp. 1–1, 2016.

[171] L. M. Nilsson, “Respiration Signals from Photoplethysmography,” *Anesthesia & Analgesia*, vol. 117, no. 4, pp. 859–865, Oct. 2013.

[172] T. H. Falk, W.-Y. Chan, E. Sejdic, and T. Chau, “Spectro-temporal analysis of auscultatory sounds,” in *New Developments in Biomedical Engineering.* InTech, 2010.

[173] S. A. Stamper, E. S. Fortune, and M. J. Chacron, “Perception and coding of envelopes in weakly electric fishes,” *Journal of Experimental Biology*, vol. 216, no. 13, pp. 2393–2402, Jul. 2013.

[174] C. S. Herrmann, M. Grigutsch, and N. A. Busch, “11 EEG oscillations and wavelet analysis,” *Event-related potentials: A methods handbook*, p. 229, 2005.

[175] M. K. van Vugt, P. B. Sederberg, and M. J. Kahana, “Comparison of spectral analysis methods for characterizing brain oscillations,” *Journal of Neuroscience Methods*, vol. 162, no. 1-2, pp. 49–63, May 2007.

[176] A. Bruns, “Fourier-, Hilbert- and wavelet-based signal analysis: Are they really different approaches?” *Journal of Neuroscience Methods*, vol. 137, no. 2, pp. 321–332, Aug. 2004.

[177] F. C. Morabito, D. Labate, A. Bramanti, F. L. Foresta, G. Morabito, I. Palamara, and H. H. Szu, “Enhanced Compressibility of EEG Signal in Alzheimer’s Disease Patients,” *IEEE Sensors Journal*, vol. 13, no. 9, pp. 3255–3262, Sep. 2013.

[178] J. Solé-Casals and F.-B. Vialatte, “Towards Semi-Automatic Artifact Rejection for the Improvement of Alzheimer’s Disease Screening from EEG Signals,” *Sensors*, vol. 15, no. 8, pp. 17 963–17 976, Jul. 2015.

[179] L. R. Trambaiolli, A. C. Lorena, F. J. Fraga, P. A. Kanda, R. Anghinah, and R. Nitrini, "Improving Alzheimer's Disease Diagnosis with Machine Learning Techniques," *Clinical EEG and Neuroscience*, vol. 42, no. 3, pp. 160–165, Jul. 2011.

[180] A. Delorme and S. Makeig, "EEGLAB: An open source toolbox for analysis of single-trial EEG dynamics including independent component analysis," *Journal of neuroscience methods*, vol. 134, no. 1, pp. 9–21, 2004.

[181] S. Romero, M. A. Mañanas, and M. J. Barbanoj, "A comparative study of automatic techniques for ocular artifact reduction in spontaneous EEG signals based on clinical target variables: A simulation case," *Computers in Biology and Medicine*, vol. 38, no. 3, pp. 348–360, Mar. 2008.

[182] I. Guyon, J. Weston, S. Barnhill, and V. Vapnik, "Gene selection for cancer classification using support vector machines," *Machine learning*, vol. 46, no. 1-3, pp. 389–422, 2002.

[183] C. A. Joyce, I. F. Gorodnitsky, and M. Kutas, "Automatic removal of eye movement and blink artifacts from EEG data using blind component separation," *Psychophysiology*, vol. 41, no. 2, pp. 313–325, Mar. 2004.

[184] A. Schlögl, C. Keinrath, D. Zimmermann, R. Scherer, R. Leeb, and G. Pfurtscheller, "A fully automated correction method of EOG artifacts in EEG recordings," *Clinical Neurophysiology*, vol. 118, no. 1, pp. 98–104, Jan. 2007.

[185] S. O'Regan and W. Marnane, "Multimodal detection of head-movement artefacts in EEG," *Journal of Neuroscience Methods*, vol. 218, no. 1, pp. 110–120, Aug. 2013.

[186] S. T. DeKosky and S. W. Scheff, "Synapse loss in frontal cortex biopsies in Alzheimer's disease: Correlation with cognitive severity," *Annals of Neurology: Official Journal of the American Neurological Association and the Child Neurology Society*, vol. 27, no. 5, pp. 457–464, 1990.

[187] L. A. Coben, W. Danziger, and M. Storandt, "A longitudinal EEG study of mild senile dementia of Alzheimer type: Changes at 1 year and at 2.5 years," *Electroencephalography and clinical neurophysiology*, vol. 61, no. 2, pp. 101–112, 1985.

[188] D. Krusienski, E. Sellers, D. McFarland, T. Vaughan, and J. Wolpaw, "Toward enhanced P300 speller performance," *Journal of Neuroscience Methods*, vol. 167, no. 1, pp. 15–21, Jan. 2008.

[189] J.-S. Kim, S.-H. Lee, G. Park, S. Kim, S.-M. Bae, D.-W. Kim, and C.-H. Im, "Clinical Implications of Quantitative Electroencephalography and Current Source Density in Patients with Alzheimer's Disease," *Brain Topography*, vol. 25, no. 4, pp. 461–474, Oct. 2012.

[190] D. A. Casey and Associate Professor, Department of Psychiatry and Behavioral Sciences, University of Louisville School of Medicine, "Event-related Potentials and the Diagnosis of Alzheimer's Disease— The COGNISION™ System," *US Neurology*, vol. 06, no. 02, p. 34, 2010.

[191] Y. Stern, "Cognitive reserve in ageing and Alzheimer's disease," *The Lancet Neurology*, vol. 11, no. 11, pp. 1006–1012, Nov. 2012.

[192] R. Anghinah, P. A. M. Kanda, H. F. Lopes, L. F. H. Basile, S. Machado, P. Ribeiro, B. Velasques, K. Sameshima, D. Y. Takahashi, L. F. Pinto, and others, "Alzheimer's disease qEEG: Spectral analysis versus coherence. which is the best measurement?" *Arquivos de neuro-psiquiatria*, vol. 69, no. 6, pp. 871–874, 2011.

[193] J. Mazziotta, A. Toga, A. Evans, P. Fox, J. Lancaster, K. Zilles, R. Woods, T. Paus, G. Simpson, B. Pike, C. Holmes, L. Collins, P. Thompson, D. MacDonald, M. Iacoboni, T. Schormann, K. Amunts, N. Palomero-Gallagher, S. Geyer, L. Parsons, K. Narr, N. Kabani, G. L. Goualher, D. Boomsma, T. Cannon, R. Kawashima, and B. Mazoyer, "A probabilistic atlas and reference system for the human brain: International Consortium for Brain Mapping (ICBM)," *Philosophical Transactions of the Royal Society B: Biological Sciences*, vol. 356, no. 1412, pp. 1293–1322, Aug. 2001.

[194] M. Brett, I. S. Johnsrude, and A. M. Owen, “The problem of functional localization in the human brain,” *Nature Reviews Neuroscience*, vol. 3, no. 3, pp. 243–249, Mar. 2002.

[195] J. N. Ianof, F. J. Fraga, L. A. Ferreira, R. T. Ramos, J. L. C. Demario, R. Baratho, L. F. H. Basile, R. Nitrini, and R. Anghinah, “Comparative analysis of the electroencephalogram in patients with Alzheimer’s disease, diffuse axonal injury patients and healthy controls using LORETA analysis,” *Dementia & Neuropsychologia*, vol. 11, no. 2, pp. 176–185, Jun. 2017.

[196] R. Lizio, C. Del Percio, N. Marzano, A. Soricelli, G. G. Yener, E. Başar, C. Mundi, S. De Rosa, A. I. Triggiani, R. Ferri, D. Arnaldi, F. M. Nobili, S. Cordone, S. Lopez, F. Carducci, G. Santi, L. Gesualdo, P. M. Rossini, E. Cavedo, M. Mauri, G. B. Frisoni, and C. Babiloni, “Neurophysiological Assessment of Alzheimer’s Disease Individuals by a Single Electroencephalographic Marker,” *Journal of Alzheimer’s Disease*, vol. 49, no. 1, pp. 159–177, Sep. 2015.

[197] F. Vecchio, F. Miraglia, C. Marra, D. Quaranta, M. G. Vita, P. Bramanti, and P. M. Rossini, “Human brain networks in cognitive decline: A graph theoretical analysis of cortical connectivity from EEG data,” *Journal of Alzheimer’s Disease*, vol. 41, no. 1, pp. 113–127, 2014.

[198] L. R. Gianotti, G. Künig, D. Lehmann, P. L. Faber, R. D. Pascual-Marqui, K. Kochi, and U. Schreiter-Gasser, “Correlation between disease severity and brain electric LORETA tomography in Alzheimer’s disease,” *Clinical Neurophysiology*, vol. 118, no. 1, pp. 186–196, Jan. 2007.

[199] O. Tsinalis, P. M. Matthews, Y. Guo, and S. Zafeiriou, “Automatic Sleep Stage Scoring with Single-Channel EEG Using Convolutional Neural Networks,” *arXiv preprint*, p. 12, 2016.

[200] G. Ruffini, D. Ibanez Soria, L. Dubreuil, M. Castellano, J.-F. Gagnon, J. Montplaisir, and A. Soria-Frisch, “Deep learning with EEG spectrograms in rapid eye movement behavior disorder,” *bioRXiv preprint*, May 2018.

[201] S. Lithfous, A. Dufour, and O. Després, “Spatial navigation in normal aging and the prodromal stage of Alzheimer’s disease: Insights from imaging and behavioral studies,” *Ageing Research Reviews*, vol. 12, no. 1, pp. 201–213, Jan. 2013.

[202] K. Vlček, *Spatial Navigation Impairment in Healthy Aging and Alzheimer’s Disease.* INTECH Open Access Publisher, 2011.

[203] V. D. Bohbot, J. Lerch, B. Thorndycraft, G. Iaria, and A. P. Zijdenbos, “Gray matter differences correlate with spontaneous strategies in a human virtual navigation task,” *The Journal of Neuroscience: The Official Journal of the Society for Neuroscience*, vol. 27, no. 38, pp. 10 078–10 083, Sep. 2007.

[204] M. J. Kahana, R. Sekuler, J. B. Caplan, M. Kirschen, and J. R. Madsen, “Human theta oscillations exhibit task dependence during virtual maze navigation,” *Nature*, vol. 399, no. 6738, pp. 781–784, Jun. 1999.

[205] J. Park, H. Lee, T. Kim, G. Y. Park, E. M. Lee, S. Baek, J. Ku, I. Y. Kim, S. I. Kim, D. P. Jang, and J. K. Kang, “Role of low- and high-frequency oscillations in the human hippocampus for encoding environmental novelty during a spatial navigation task: Hippocampal Oscillations in Spatial Navigation,” *Hippocampus*, vol. 24, no. 11, pp. 1341–1352, Nov. 2014.

[206] A. Coutrot, R. Silva, E. Manley, W. de Cothi, S. Sami, V. D. Bohbot, J. M. Wiener, C. Hölscher, R. C. Dalton, M. Hornberger *et al.*, “Global determinants of navigation ability,” *Current Biology*, 2018.

[207] R. I. García-Betances, M. T. Arredondo Waldmeyer, G. Fico, and M. F. Cabrera-Umpiérrez, “A Succinct Overview of Virtual Reality Technology Use in Alzheimer’s Disease,” *Frontiers in Aging Neuroscience*, vol. 7, May 2015.

[208] T. J. Crawford, S. Higham, T. Renvoize, J. Patel, M. Dale, A. Suriya, and S. Tetley, “Inhibitory control of saccadic eye movements and cognitive impairment in Alzheimer’s disease,” *Biological Psychiatry*, vol. 57, no. 9, pp. 1052–1060, May 2005.

[209] M. Vidal, J. Turner, A. Bulling, and H. Gellersen, “Wearable eye tracking for mental health monitoring,” *Computer Communications*, vol. 35, no. 11, pp. 1306–1311, Jun. 2012.

[210] A. Bulling, D. Roggen, and G. Troester, “What’s in the Eyes for Context-Awareness?” *IEEE Pervasive Computing*, vol. 10, no. 2, pp. 48–57, 2011.

Appendix A

Open-source Amplitude Modulation Analysis Toolkit

The amplitude modulation analysis toolkit for MATLAB, Octave and Python, provides functions to compute the transformations from a time real-valued signal to its time-frequency and frequency-frequency domain representations, the methods for these transformations are presented in Chapter 3. The toolkit provides two implementations for the time to time-frequency transformation, one based on the short-time Fourier transform and the other on the continuous wavelet transform using the complex Morlet wavelet. The time-frequency to frequency-frequency transformation is carried out with the Fourier transform. This toolkit includes a graphical user interface (GUI) which facilitates the exploration of the amplitude modulation by allowing changing parameters online, Figure A.1. Besides the functions to compute and visualize the time-frequency and frequency-frequency representations, example data and scripts are provided.

The source code and examples for this toolkit are provided under the MIT licence. The toolkit is available in two GitHub repositories: the MATLAB / Octave version [1] and the Python2 / Python3 version[2].

---

[1] `https://github.com/MuSAELab/amplitude-modulation-analysis-matlab`

[2] `https://github.com/MuSAELab/amplitude-modulation-analysis-module`

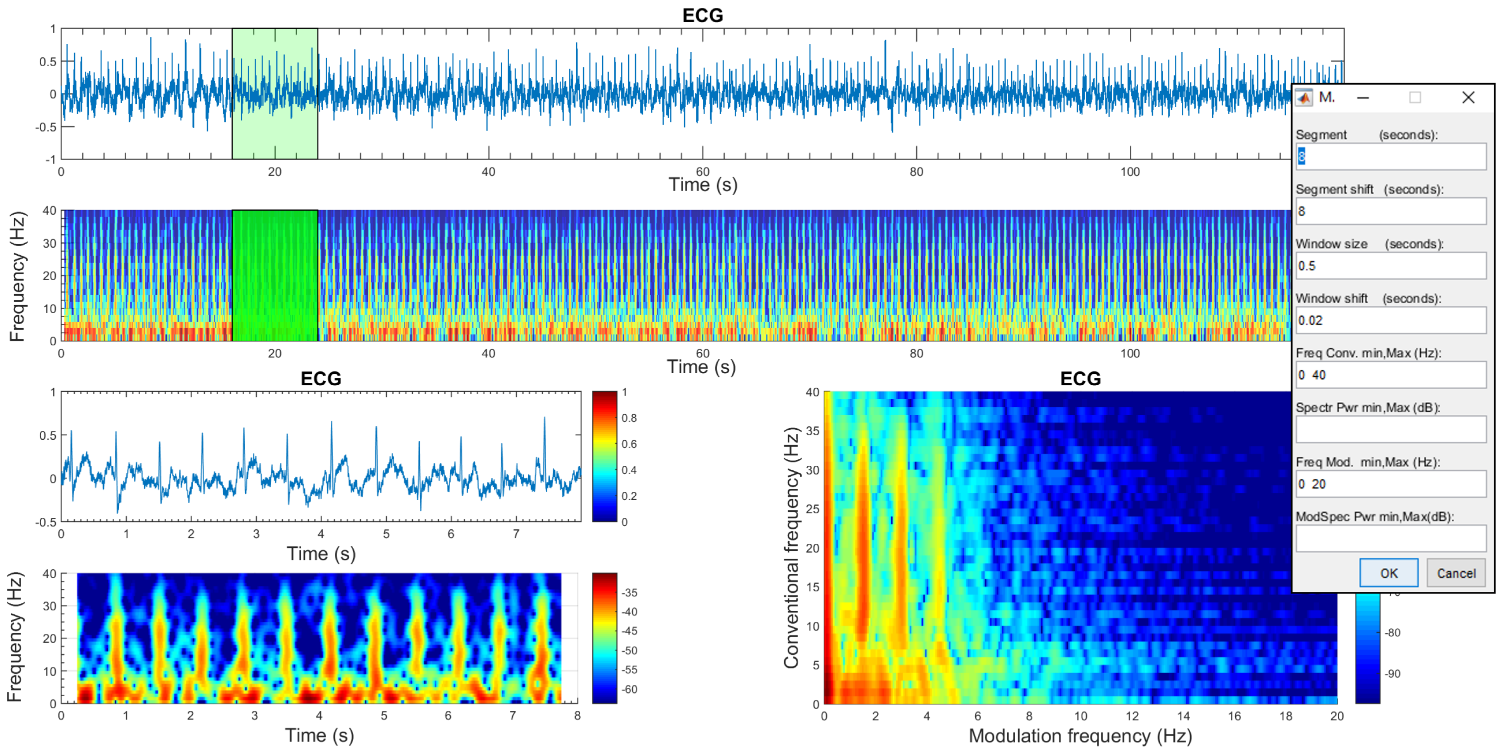

Segment (seconds): 8

Segment shift (seconds): 8

Window size (seconds): 0.5

Window shift (seconds): 0.02

Freq Conv. min,Max (Hz): 0 40

Spectr Pwr min,Max (dB):

Freq Mod. min,Max (Hz): 0 20

ModSpec Pwr min,Max(dB):

Figure A.1 – GUI of the amplitude modulation analysis toolkit.

Appendix B

MuLES: An Open-source EEG Acquisition and Streaming Server

The burgeoning availability of new portable consumer grade EEG devices has reinforced the use of EEG in traditional research and clinical fields and has opened the doors to its utilization in novel domains such as neurogaming, live performance and arts. Although they offer two pivotal advantages (i.e. portability and affordability), consumer grade devices present some drawbacks such as: (*i*) each device possesses its own software developer's kit (SDK), communication protocol or driver, hindering the development of device-independent applications, and (*ii*) extensive programming experience is required to interface such devices with any given application.

The MuSAE Lab EEG Server (MuLES) is an open-source EEG acquisition and streaming server that aims at creating a common interface for portable EEG devices, facilitating the development of device-agnostic applications as shown in Figure B.1. It provides a minimalist GUI that allows quick and simple interfacing with different portable EEG consumer devices.

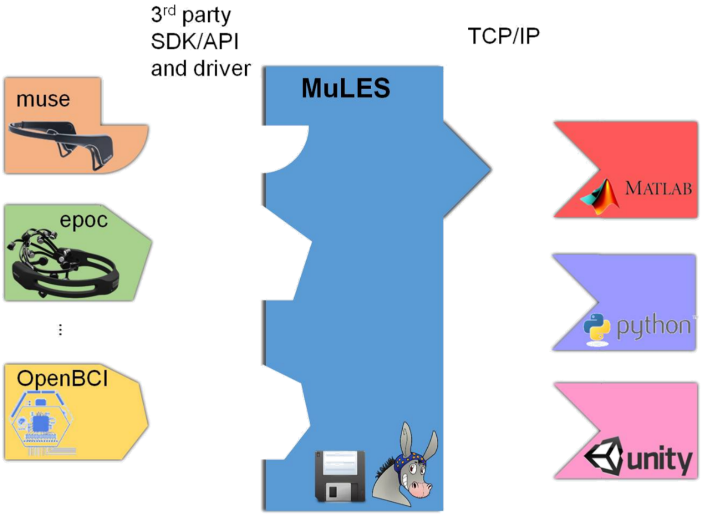

Figure B.1 – Architecture of MuLES: EEG devices are connected through their respective drivers, EEG data is recorded and communication to external client applications is done using the TCP/IP.

The source code, installer and examples are provided under the MIT licence. MuLES is available as a GitHub repository[1].

MuLES features

- Simple GUI allowing recording and streaming of data with a few clicks, Figure B.2.
- Recording of EEG data in standard formats: CSV, EDF.
- Streaming of EEG data (from devices or files) using TCP/IP.
- Simultaneous multiple instances facilitating data synchronization across multiple devices.
- Clients for different programming languages provided MATLAB/Octave, Python, Unity.

---

[1] `https://github.com/MuSAELab/MuLES`

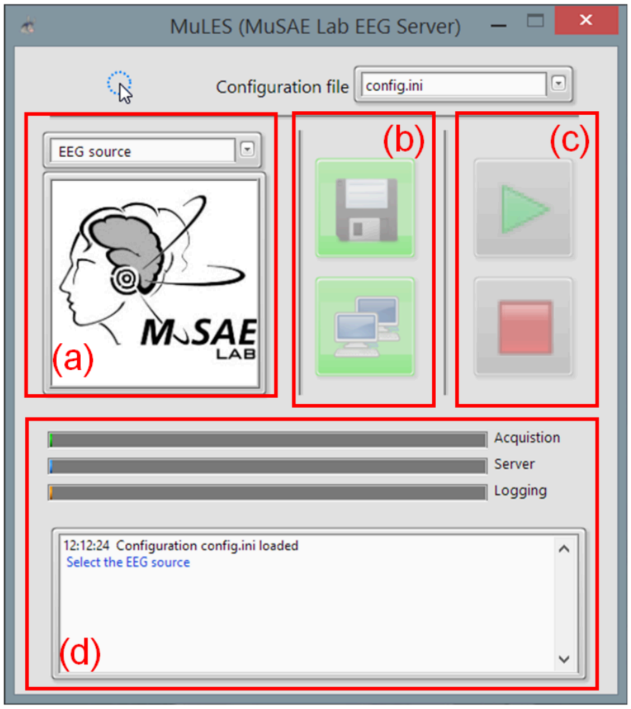

Configuration file: config.ini

```
12:12:24  Configuration config.ini loaded
 Select the EEG source
```

Figure B.2 – MuLES GUI and its sections: (a) input device selection, (b) recording and streaming controls, (c) start/stop acquisition and (d) current server state information.